UNIVERSITY OF CALIFORNIA

SANTA CRUZ

Controlling Ion transport at the Biotic-Abiotic Interface

A dissertation submitted in partial satisfaction of the

requirement for the degree of

DOCTOR OF PHILOSOPHY

in

ELECTRICAL & COMPUTER ENGINEERING

by

Le Luo

December 2023

The Dissertation of Le Luo

is approved:

_____

Professor Marco Rolandi, Chair

_____

Professor Ahmet Ali Yanik

_____

Professor Mircea Teodorescu

_____

Peter F. Biehl
Vice Provost and Dean of Graduate Studies

Copyright © by

Le Luo

2023

Table of Contents

INTRODUCTION *1*

1. Bioelectronics *1*

2. Ion transport mechanism *6*

2.1 Ion conduction **6**

2.2 Proton transport **7**

3. Materials in bioelectronic devices *10*

3.1 Conducting Polymers **10**

3.2 Ion conducting hydrogels **11**

4. Ion channels with bioelectronics *14*

4.1 Cell Membrane and Transmembrane Channels **14**

4.2 Electrodes for Electrochemical Impedance Spectroscopy (EIS) and Proton Conducting PdHx electrodes **16**

4.3 Bioelectronic platforms with supported lipid bilayer and transmembrane channels **19**

RESEARCH CONTRIBUTION *21*

5. Design, improvement and applications of the anion hydrogel *21*

5.1 Correlating protonic Conductivity and Microstructure in Polyelectrolyte Hydrogels **21**

5.1.1 Introduction 22

5.1.2 Results 24

5.1.3 Conclusion 41

5.1.4 Experimental Section/Methods 42

5.2 A Bioelectronic Device for Controlled Delivery of Ions and Biomolecules in Wound Healing 44

5.2.1 Introduction 45

5.2.2 Results 46

5.2.3 Conclusion 59

5.2.4 Methods 60

6. DNA nanopores as artificial membrane channels for bioprotonics 62

6.1 Introduction 63

6.2 Results 65

6.2.1 DNA Nanopore Bioprotonics 65

6.2.2 Control of H^+ flow with DNA Nanopore Bioprotonics 74

6.2.3 Programming the DNA nanopores for biomolecular sensing 80

6.2.4 A model for the rate constant of association and dissociation of DNA nanopores self-insertion 87

6.3 Discussion 91

6.4 Methods 93

6.4.1 Materials 93

6.4.2 Device architecture, fabrication and characterization: 93

6.4.3 Electrical measurements: 94

6.4.4 SLB formation: 94

6.4.5 Fluorescence imaging and fluorescence recovery after photobleaching measurements (FRAP) 95

6.4.6 DNA nanopores folding and characterization: 96

6.4.7 Simulation: 99

7. Outlook 100

8. Reference 101

List of Figures

Figure 1 4

Figure 2 4

Figure 3 5

Figure 4 8

Figure 5 10

Figure 6 12

Figure 7 13

Figure 8 16

Figure 9 18

Figure 10 20

Figure 11 26

Figure 12 27

Figure 13 27

Figure 14 29

Figure 15 30

Figure 16 32

Figure 17 32

Figure 18 36

Figure 19 39

Figure 20 40

Figure 21 48

Figure 22 49

Figure 23 51

Figure 24 53

Figure 25 54

Figure 26 55

Figure 27 59

Figure 28 66

Figure 29 66

Figure 30 72

Figure 31 73

Figure 32 76

Figure 33 77

Figure 34 80

Figure 35 83

Figure 36 84

Figure 37 85

Figure 38 90

Figure 39 91

List of Tables

Table 1 24

Table 2 33

Table 3 34

Table 4 41

Table 5 69

Table 6 78

Table 7 98

Le Luo

Ion Conducting Materials and Ion Channels for Bioelectronics

Abstract

Bioelectronics, an interdisciplinary field at the intersection of biology and electrical engineering, mainly involves the developments and applications of electrical devices, sensors to interact with biological system. A significant progress has been made in the field of electronics but it is still a challenge to integrate biological system with traditional electrical devices. Therefore, it is necessary to investigate ion conducting materials, such as polymers and hydrogels, allowing ions and biomolecules to move in and out of cells, and ion channels, playing a vital role in regulating the flow of ions and biomolecules across the cell membrane.

This work showed typical examples of ion conducting materials, hydrogels and their ion conductivity characterization and applications. Furthermore, a systematic study on a polyelectrolyte hydrogel including amount of polymer, crosslinker and the correlated conductivity with the microstructure. In addition, I designed, fabricated, integrated a bioprotonic device with membrane spanning DNA nanopores to transport proton ions (H^+) and enable electronic recognition of biomolecular signals such as presence of Streptavidin and the cardiac biomarker B-type natriuretic peptide. The results not only broaden the knowledge and comprehension of ion conducting material by the exploration of iontronics field, but also lay the foundations to explore potential future applications of the bioprotonics in the field of proton pump and biosensing.

Acknowledgments

I extend my deepest gratitude and heartfelt thanks to the individuals whose unwavering support and guidance have been instrumental in the completion of my doctoral degree.

First and foremost, I would express my thanks to my supervisor, Marco Rolandi. His wisdom, mentorship, and encouragement throughout this journey have been invaluable. His dedication to excellence has shaped not only my work but also my approach to academia. His attitude to education, academics, research and even life influences me a lot and thus encourage me to chase my goals and enrich my life. I believe that it will ignite my forward way in the future.

I'd like to confer my special thanks to my committees, Dr. Ahmet Ali Yanik and Dr. Mircea Teodorescu, for their precious suggestions and time.

I am indebted to the members of the Rolandi Group for their constructive feedback and scholarly discussions that have enriched the quality of my research: Dr. Harika Dechiraju, Dr. Manping Jia, Dr. John Selberg, Dr. Houpu Li, Dr. Yunjeong Park, PhD Candidate Tiffany Nguyen, and all the other past and present members.

I extend my sincere thanks to Dr. Tom Yuzvinsky in the ECE program for his dedicated management of the cleanroom's daily operations. His selfless advice has significantly enhanced my technical expertise and skills.

I extend my gratitude to my collaborators for their support, which made my research endeavor possible: PhD Candidate Swathi Manda and Dr. Busra Demir.

My sincere appreciation goes to my friends who stood by me, offering both support and understanding during the challenges of PhD study.

Last but not least, to my family, who provided a constant source of love and encouragement, I am profoundly grateful. Your unwavering belief in my abilities has been my driving force. Specially, my parents, Mingqian Luo, and Xiaolan Xiong, unwaveringly believe that I will achieve my eventual goal and support me in various ways. Their love and advice consistently warm my spirit, providing the energy I need to face any challenges that come my way. Despite the challenges of being physically apart, my girlfriend, Yuyao Huang, steadfastly supports me in all my endeavors, no matter what I choose to pursue. Even we are split, closing my eyes allow me to hear and feel her support, advices, encouragement, and love.

Thank you all, from the bottom of my heart.

Publications in this dissertation

[1] L. Luo, S. Manda, Y. Park, B. Demir, J. Vicente, M.P. Anantram, E.E. Oren, A. Gopinath, and M. Rolandi. "DNA nanopores as artificial membrane channels for bioprotonics" Nat. Commun. 14, 5364 (2023)

[2] Y. Park*, L. Luo*, M. Rolandi. "Integrating Ion Channels with Bioelectronics for Biotic-Abiotic Systems" Advanced Intelligent Systems, 5(8), 2200312 (2023) (*contributed equally)

[3] M. Jia, L. Luo, M. Rolandi. "Correlating Ionic Conductivity and Microstructure in Polyelectrolyte Hydrogels for Bioelectronic Devices" Macromolecular Rapid Communications, 43(6), 2100687, (2022)

[4] H. Dechiraju, M. Jia, L. Luo and M. Rolandi. "Ion-conducting hydrogels and their applications" Advanced Sustainable Systems, 6 (2), 2100173 (2022)

[5] N. Asefifeyzabadi, T. Nguyen, H. Li, K. Zhu, H. Yang, P. Baniya, A.M. Lopez, A. Gallegos, H. Hsieh, C. Hernandez, C. Recendez, M. Tebyani, J.Selberg, L. Luo, E. Muzzy, M. A. AlHamo, M. Levin, E. Aslankoohi, M. Gomez, M. Zhao, R. R. Isseroff, M. Teodorescu, and M. Rolandi. "A Bioelectronic Device for Controlled Delivery of Ions and Biomolecules in Wound Healing" Wound Repair and Regeneration, (Submitted) (2023)

Publications not in this dissertation

[6] W. R. Hollingsworth, A. R. Johnston, M. Jia, L. Luo, Y. Park, W. Meier, J. Palmer, M. Rolandi, and A. L. Ayzner. "Influence of Backbone Regioregularity on the

Optoelectronic and Mechanical Response of Conjugated Polyelectrolyte-Based Hydrogels" The Journal of Physical Chemistry, 127, 10, 2277–2285 (2023)

[7] H. Li, H. Yang, N. Asefifeyzabadi, P. Baniya, A. M. Lopez, A. Gallegos, K. Zhu, H. Hsieh, T. Nguyen, C. Hernandez, K. Zlobina, C. Recendez, M. Tebyani, H. Carrión, J. Selberg, L. Luo, M. A. Alhamo, N. Norouzi, M. Gomez, M. Zhao, M. Teodorescu, R. R. Isseroff, and M. Rolandi. "Programmable delivery of fluoxetine via wearable bioelectronics accelerates wound healing in vivo" Advanced Materials Technologies, (Accepted) (2023)

INTRODUCTION

1. Bioelectronics

Bioelectronics integrates biomolecules with electrical elements which uses or transduces electrical signals to interact with biotic systems[1-3]. People regard Luigi Galvani's frog experiment as the foundation of modern electrophysiology, neuroscience, and bioelectronics. He provided evidence for the artificial electricity of animal spirit in essence involved in muscle contraction and nerve conduction by the well-known experiment to gain insights into animal electricity [4]. Afterward, as study of the structure of the giant fibers and experimental investigation of functioning of nerve fibers, exploration of actuator of body current has attracted much attention[5]. For example, Rothenberg, Keynes and Lewis found that the nervous impulse is associated with an inflow of sodium and an outflow of potassium[6]. Moreover, many groups of experiments describe that the changes of permeability of ions especially sodium and potassium lead to nervous conduction. These insane discoveries of bioelectronics have aroused great interest in therapy, and clinical diagnose, such as cardiac pacemakers generating electrical pulses delivered by electrodes to one or more of the chambers of the heart to maintain an adequate heart rate [7], and brain implants electrically stimulating signals from single neurons in the brain to maintain normal neural processing[8-10]. However, in contrast to the rapid advancements in pharmaceuticals, neuromodulation, and electroceuticals, traditional electronics suffers from the disadvantages of rigidity, limited biocompatibility, incompatibility with living tissues and so on[1,2]. Additionally,

in electronics, electrons and holes, serving as the primary charge carriers, are essential for the proper functioning of electronic devices while ions are the main charge carriers in living systems[11,12]. To overcome above difficulties, bioelectronics necessitates materials that are not only well-suited for interfacing with soft organisms and tissues but also capable of facilitating ion conduction and transport.

On one hand, compared to the giant mismatch of Young's moduli between stiffer metals and inorganic semiconductors and tissues, widely used materials such as polymers and hydrogels in bioelectronics are much biocompatible and milder[13,14]. Accordingly, iontronic devices, commonly used to generate, store and transmit electrical signals to biological signals via the concentration, depletion, distribution and flow of ions spatially and temporally, require robust integrations involving well-suited ion conducting materials combining with traditional electrical devices like field effect transistor (FET)[15]. Examples contain organic field effect transistor (OFET)[16], organic electrochemical effect transistor (OECT)[17], ion pump[18,19], organic electronic ion pump (OEIP)[20] and so on. Within these ionic devices, cations and anions as the charge carriers are needed to be independently handled in iontronic devices which are similar to electrons and holes in electrical devices. For this purpose, the most widely employed ionic conducting materials are polyelectrolytes that either selectively permeable to cations or anions[21]. As the key in iontronics, controlled ionic conduction is achieved by applying an electric field over ion exchange membranes (IEMs), generally polymers with charged side groups (Figure 1)[22]. Typically, Poly(3,4-ethylenedioxythiophene) doped with poly(styrenesulfonate) (PEDOT:PSS) (Figure 2) is one of the most famous

polymer-based ion-exchange membrane materials[23,24]. In addition, based on the exploration of ion-conducting polymers, hydrogels have become the material of choice in bioelectronic devices because their high-water content leads to efficient ion transport and a conformal interface with biological tissue. With the biocompatible properties of water swollen porous polymer networks, hydrogels become ideal choices for the bioelectronic interface between electronics and biological systems.

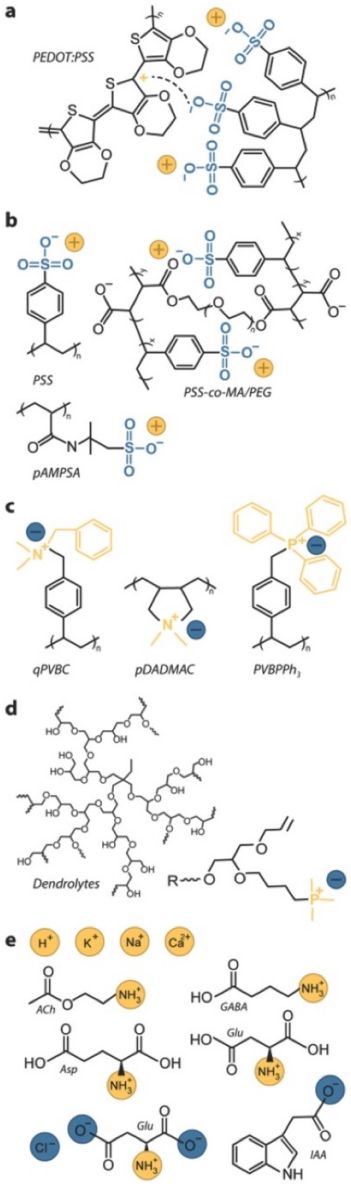


Figure 1: Iontronics materials with ionic conduction. (a) Chemical structure of Poly(3,4-ethylenedioxythiophene) doped with poly(styrenesulfonate) (PEDOT:PSS), a conducting polymer, frequently used as electrode material. (b) Polyanions, the cation-exchange membrane materials. (c) Polycations, anion-exchange membrane materials. (d) Hyperbranched polyglycerol dendrolyte functionalized as an anion exchange membrane. (e) Examples of charged biologically relevant molecules capable of acting as charge carriers in iontronics. Blue circle: Negative charge; Yellow circle: positive charge. Adapted with permission[22]. Copy right 2018, Advanced Materials Technologies.

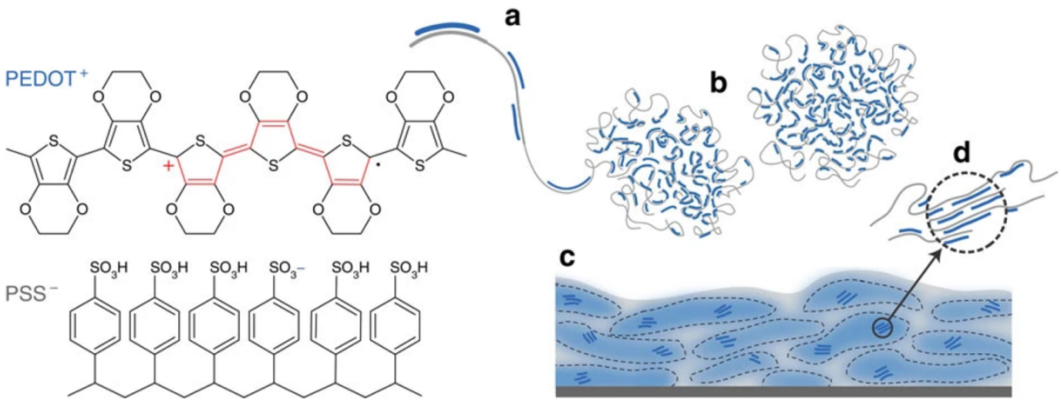


Figure 2: Chemical structure of PEDOT:PSS. (a) PEDOT synthesis onto PSS template, (b) formation of colloidal gel particles when dispersed in water, (c) the resulting films with PSS-dominated regions (gray) and PEDOT:PSS-dominated regions (blue) and (d) Aggregates/crystallites promoting electronic transport. Adapted with permission[23]. Copy right 2016, Nature Communications.

On the other hand, precise and highly regulated flow of biomolecules and ions through complex cellular networks is crucial for communication and information processing in

living systems. In contrast, human-made electronics rely on the flow of electrons and holes through well-defined semiconductor networks for processing. A broad variety of ion channels play a vital role in regulating the flow of ions and biomolecules across the cell membrane with a complexity unmatched in any semiconductor device. Recently, a great deal of progress has been made in transmembrane channels with supported lipid bilayers (SLBs) which create a planar cell membrane for integration with bioelectronics to enable biotic-abiotic communication and leverage this complexity (Figure 3)[25-27].

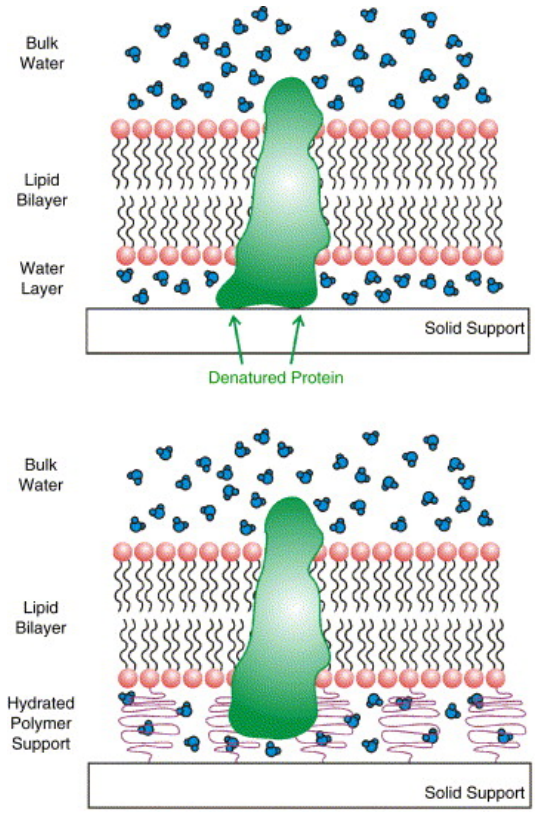


Figure 3: Transmembrane proteins are capable of immobilized and denatured with SLBs on a solid surface (above). And a polymer cushion can also help shield the protein from the substrate (bottom). Adapted with permission[27]. Copy right 2006, Surface Science Reports.

2. Ion transport mechanism

2.1 Ion conduction

The history of ionic conductors can be traced back to the 1830s with the work of Michael Faraday on solid electrolytes[28]. The discovery of silver iodide and sodium alumina in 1967 is considered the beginning of the solid-state ionic field[29,30]. Around the same time, Dupont synthesized a polymer ionomer known as Nafion, which is one of the best proton conductors[31]. Charge carriers in ionic conductors are negatively charged (anions) or positively charged (cations).There can be multiple ionic species with different charges, so the total conductivity of an ionic conductor is given by the sum of the contributions of all of charge carriers (Equation 1)[32]:

$$\sigma = \sum_i Z_i e n_i u_i \quad (1)$$

σ is the sum of the ionic conductivity contributed by each mobile ion (i), where Z_i is the absolute value of the ion charge, e is the fundamental charge, n_i is the charge carrier density, and μ_i is the mobility for each ion.

Although the majority of hydrogels are able to conduct ions because of their aqueous environment, here we mainly discuss the hydrogels that have fixed charges in the polymer network, polyelectrolyte hydrogels. From eq (1), the ionic conductivity of a hydrogel is dependent on both the property of the ionic conductor, such as the charge carrier density, and the property of the charged species, such as their mobility. The assumption is that a hydrogel will be charge neutral so a fixed charge in the polymer backbone will result in the same amount of mobile charge that can contribute to the ionic conductivity. The mobility (μ) of different ions is dependent on the temperature

of the system (T), the diffusion coefficient (D), charge of the ion (q), and the Boltzmann constant (K_B) as shown in Equation 2.

$$\mu = \frac{\boldsymbol{Dq}}{\boldsymbol{k_B T}} \tag{2}$$

In a porous network, the diffusion coefficient of ions is smaller than the diffusion coefficient for the same ion in water and needs to be adjusted for the size and topography of the pores as shown in Equation 3 [33,34]:

$$D_{eff} = D_0 \frac{\epsilon}{\tau} \tag{3}$$

where D_{eff} is effective diffusion coefficient in a porous network, D_0 is the diffusion coefficient in liquid, ϵ is the porosity, and τ is the tortuosity, which describes the non-linear path from one side of the membrane to the other[35]. Tuning charge carrier density, porosity, and tortuosity during hydrogel synthesis can optimize the ionic conductivity of the hydrogel.

2.2 Proton transport

Compared with other ions, proton can follow a version of migration through the medium along with a "vehicle" or proton solvent such as H_3O^+, $H_5O_2^+$, and $H_9O_4^+$, called vehicle mechanism, which is one of two proton-transfer mechanisms[36]. Besides, the other type of proton transfer called Grotthuss-type mechanism determines protons being transferred from one site to another through the formation and breaking of hydrogen bonds (proton hopping), and hence a vehicle or proton solvent is not needed[37]. In the Grotthuss mechanism, a proton hops from one molecule to the next one by

exchanging a hydrogen bond with a covalent bond (Figure 4)[38,39]. However, the net movement of a proton along a single file water chain does lead to the transfer of a unit charge due to the water chain remaining in a polarized state. In order to accept another proton, the water chain

Requires reordering itself by the transport of a Bjerrum D orientation defect containing the rotation of the water molecules in the chain (Figure 4a). Thus, the combined motion of H^+ and a Bjerrum D defect will translate a unit charge. Similarly, this two-step process also supports the transfer of a negatively charged OH^- as "proton hole" (Figure 6b).

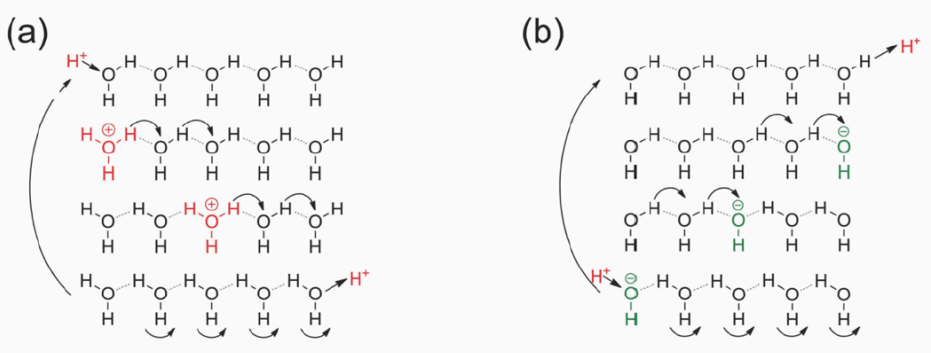


Figure 4: (a) H^+ as hydronium ion along proton wires in Grotthuss mechanism. (b) An equivalent mechanism for OH^- conductivity as proton hole along proton wire). Adapted with permission[38]. Copy right 2016, Journal of Physics.

Actually, because most metals are excellent contacts for e^- but poor for H^+ transport, most investigations on proton conduction utilize alternating current in order to avoid ion accumulation at the interface[40,41]. The couple Pd/PdH_x is capable of acting as a H^+ to electron transducer, eliciting a proton-transparent contact for DC measurements of

proton conducting materials. Pd has a strong affinity to hydrogen and forms palladium hydride (PdH_x) either by absorbing hydrogen from H_2 gas or from H^+ in solution as a reversible hydrogen electrode in electrochemistry[42]. Thus, the incorporation of H^+ from the solution into Pd is potential dependent and follows the reversible reduction: $H^+ + e^- \leftrightarrow H$, at the Pd/PdH_x–solution interface. Subsequently, H physisorbs onto Pd to form PdH_x following another reversible reaction: $H + Pd \leftrightarrow PdH_x$. An electrical potential applied (V) on the Pd/PdHx contact shifts the reaction equilibrium and induces the transfer of H^+ to or from the solution (Figure 5)[42,43]. In brief, when $V < 0$ and the contact is at a lower potential than the solution, an H^+ in solution is delivered to the Pd/solution interface where it is reduced to PdH_{ads} with absorption of H^+. PdH_{ads} subsequently absorbs onto the Pd subsurface to form PdH_{subs} and finally diffuses into the bulk Pd to form PdH_{bulk} because of the concentration gradient. In contrast, when $V > 0$, some of the H that is part of PdH_{ads} oxidizes at the Pd surface to form H^+ and dissolves into solution. Equation 4 describes the reversible process:

$$Pd + H^+ + e^- \leftrightarrow PdH_x \tag{4}$$

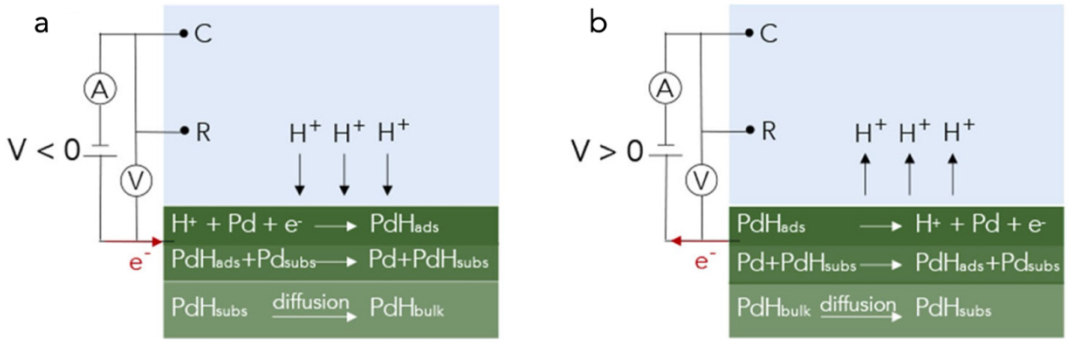


Figure 5: (a) Once a negative voltage applied, H^+ is first adsorbed onto the surface of Pd (Pd_{ads}), then absorbed onto the subsurface layer, Pd_{subs}, and further diffuses into bulk Pd to form PdH_{bulk} following the concentration gradient. (b) Once a positive voltage applied, H^+ is first released from the surface, PdH_{ads}, then from the subsurface layer (Pd_{subs}) to the surface (Pd_{ads}), and further diffuses from PdH_{bulk}. (b). Adapted with permission[43]. Copy right 2020, APL Materials.

3. Materials in bioelectronic devices

3.1 Conducting Polymers

Conducting polymers have been used in various fields such as energy storage, environmental and eco-friendly bioelectronic applications since their discovery in 1977[44-46]. Owing to their outstanding physical and chemical properties, the suitable combinations with different-size inorganic nanoparticles lead to the high performance of applications in microsystems[47]. Generally, there are four promising polymers with excellent electronic and ionic conductivities, PEDOT:PSS, polypyrrole (PPy), polythiophenes (PT), and polyaniline (PANI)[44,48]. Their porous structures for good biocompatibility with cells and good conductivities, exploit wide bioelectronic applications involving drug delivery, bioactuator, and neural probe applications[48]. Especially, ions and biomolecules are the languages between intracellular communication and organism metabolisms. Therefore, the coupled realms of ion conducting polymers and nanoscale devices provide additional insights into

bioelectronics. Subsequently, a new polymetric-network based material, hydrogel, makes a contribution to interfacing microelectrodes.

3.2 Ion conducting hydrogels

Hydrogels are crosslinked 3D polymeric networks capable of retaining water within the polymer chains.[49] The high water content makes hydrogels soft with a low Young's modulus, which results in a conformal interface with soft biological tissue[14]. In the 1960s, polyhydroxyethylmethacrylate (pHEMA) hydrogel was developed as a material for permanent contact with human tissue and it was first used in contact lenses[50,51]. Thereafter, researchers started using hydrogels in drug delivery[52], wound dressings[51,53], and tissue engineering[54,55]. Recently, hydrogels have been gradually integrated in bioelectronic devices such as for neuronal recording and simulation.[56] Water rich hydrogels are ion conductors and make for an ideal bioelectronic interface because in biological systems signals are carried on by ions and molecules[3,11,57-60]. This ionic conductivity has led to the development of iontronics - ion conducting bioelectronic devices- with an increasing amount of research focused on using hydrogels as ionic conductors at the interface[56,59,61,62]. The unique combination of ionic conductivity, soft, elastic nature and optical transparency allows ion conducting hydrogels to be widely used in developing bioelectronics. The ion conducting hydrogels' structures, ionic conduction, and applications in bioelectronic devices have been explored to ascertain the remarkable interface with biological systems (Figure 6).

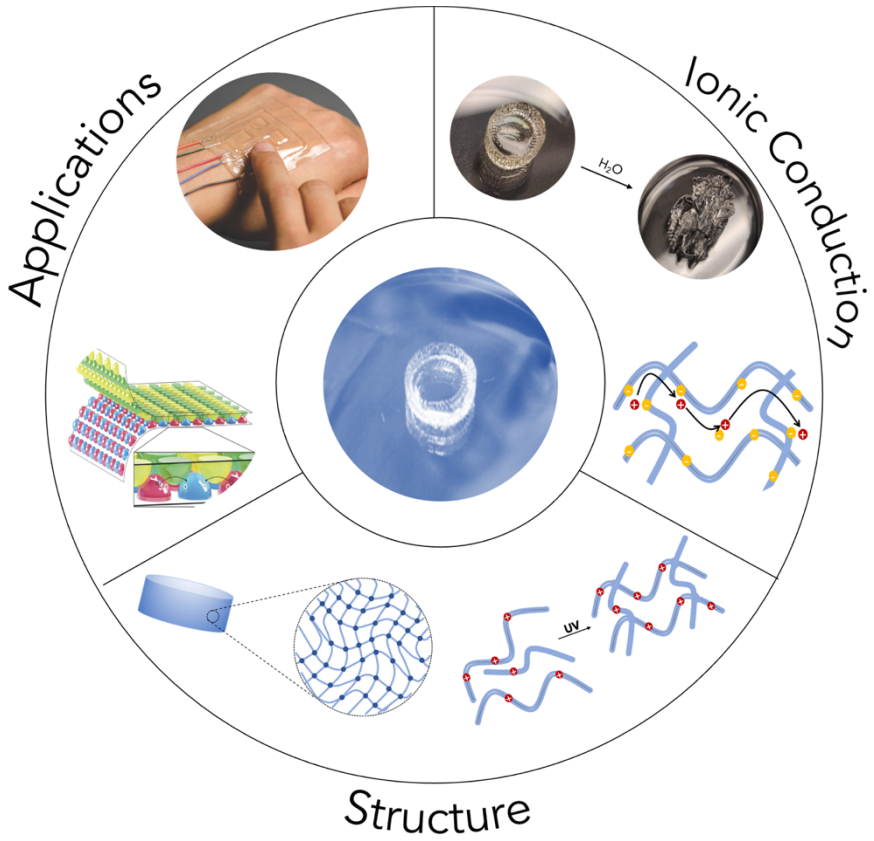


Figure 6: Hydrogels consists of various monomers cross-linked together to form a polymeric, porous mesh-like structure. This cross-linked structure allows for water absorption and ionic conductivity. This conductivity makes hydrogel ideal for bioelectronic applications.

The physical, chemical and mechanical properties of hydrogels dependent on the inter and intra-molecular interactions between the polymer functional groups and solvents present inside the 3D structure[63]. Based on their crosslinking mechanism, hydrogels can be classified as physical hydrogels and chemical hydrogels. Physical hydrogels are crosslinked by ionic and electrostatic interactions between the monomers, hydrogen

bonding, or by dipolar and hydrophobic interactions[49,64]. Chemical hydrogels have cross links formed by covalent bonds, photo-polymerization (UV induced crosslinking), and enzyme- induced crosslinks[64]. A typical chemical hydrogel structure consists of cross-linked polymer chains, fixed ions and mobile ions (Figure 7)[49,65]. Depending on the type of charges, hydrogels can be classified into neutral hydrogels and polyelectrolyte hydrogels. Polyelectrolytes have repeating electrolyte units of charged groups, such as polyanion (Figure 7a,d), polycation (Figure 7b,e), and zwitterionic (Figure 7c,f) gels[66-69].

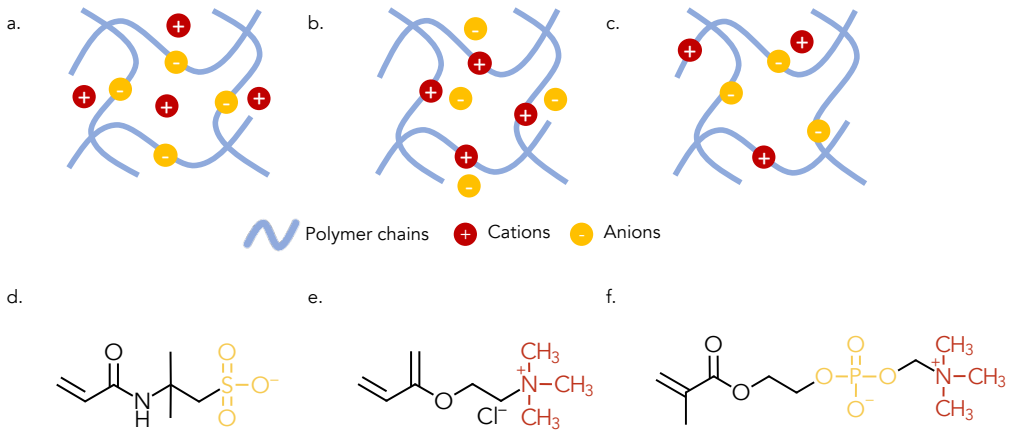


Figure 7: Schematic of the structure of (a) Polyanion hydrogel (b) Polycation hydrogel and (c) Zwitterionic hydrogel. Polyanion hydrogel has a large number of fixed anions (negatively charged ions) and can conduct cations (positively charged ions) through the gel. Polycation hydrogel has a large number of fixed cations and can conduct anions. Zwitterionic gels are composed of monomers both positively and negatively charged. (d) Polyanionic monomer - 2-acrylamido-2-methylpropane sulfonic acid (e)

Polycationic monomer - 2-(acryloyloxy) ethyltrimethyl ammonium chloride (f) Zwitterionic monomer - 2-methacryloyloxyethyl phosphorylcholine.

Over the past decade, hydrogels made from natural materials have come to the limelight because of their biocompatibility, hydrophilicity, and biodegradable nature[70]. Several natural hydrophilic polymers such as polysaccharides (hyaluronic acid, alginate, chitosan, and cellulose), proteins (collagen, gelatin), and DNA can form a three-dimensional network that can retain a large amount of interstitial water, hence forming a naturally derived hydrogel[63,71,72]. They can also mimic the chemical and physical environments of an extracellular matrix thereby making them popular candidates for creating scaffolds for drug delivery and tissue engineering applications[71,72].

4. Ion channels with bioelectronics

4.1 Cell Membrane and Transmembrane Channels

Cell membranes serve as a vital barrier between cells and their environment, and are primarily composed of amphiphilic phospholipids that spontaneously self-assemble into a continuous lipid bilayer when in water[73,74]. Since their first demonstration in 1985 by Tamm and McConnell as simple two-dimensional plasma biomimetic models, SLBs have become a versatile tool for studying transmembrane proteins and biomolecule interactions[75-77]. The mechanical and electrical properties of SLBs have been

characterized using various techniques, including fluorescence and surface plasmon resonance (SPR)[78,79], atomic force microscopy (AFM) and quartz crystal microbalance (QCM)[80-82]. Electrochemical impedance spectroscopy (EIS) and field effect were mainly used for SLBs characterizations[83].

Transmembrane channels span the lipid bilayer and enable the regulated flow of ions and small molecules across the cell membrane. Transmembrane channels can be divided into (a) passive ion channels and (b) active ion channels (Figure 8). Passive ion channels, also known as leakage channels, allow the continuous passive transport of intracellular and extracellular ions by means of hydrophilic pores that are always open (Figure 8a). These channels can be selective for specific ions, allowing certain ions to pass through more easily than others[84]. Examples of passive ion channels include gramicidin A (gA), which forms a channel permeable to small monovalent cations, protons, and water molecules but not divalent cations and anions[85]. Active ion channels, on the other hand, can open, close, or act as pumps depending on external factors such as chemistry, voltage, and light (Figure 8b)[86-88]. For example, bacteriorhodopsins are light-gated ion channels that change conformation upon absorbing a specific wavelength of light, transporting ions across the membrane[89]. Recently, many strategies have emerged to create artificial membrane channels (Figure 8c). These strategies include carbon nanotube porins[90], DNA nanopores[91], and random heteropolymers (RHPs)[92]. Carbon nanotube porins consist of carbon nanotubes (~10 nm in length) that are coated with a lipid layer so that they position themselves across the cell membranes. Carbon nanotube porins transport protons, small ions, and single strand DNAs[90]. DNA

nanopores are designed with programmable triggers and transport small ions and dye for real-time detecting systems[91]. RHPs can position themselves across the cell membrane and efficiently transport protons[92].

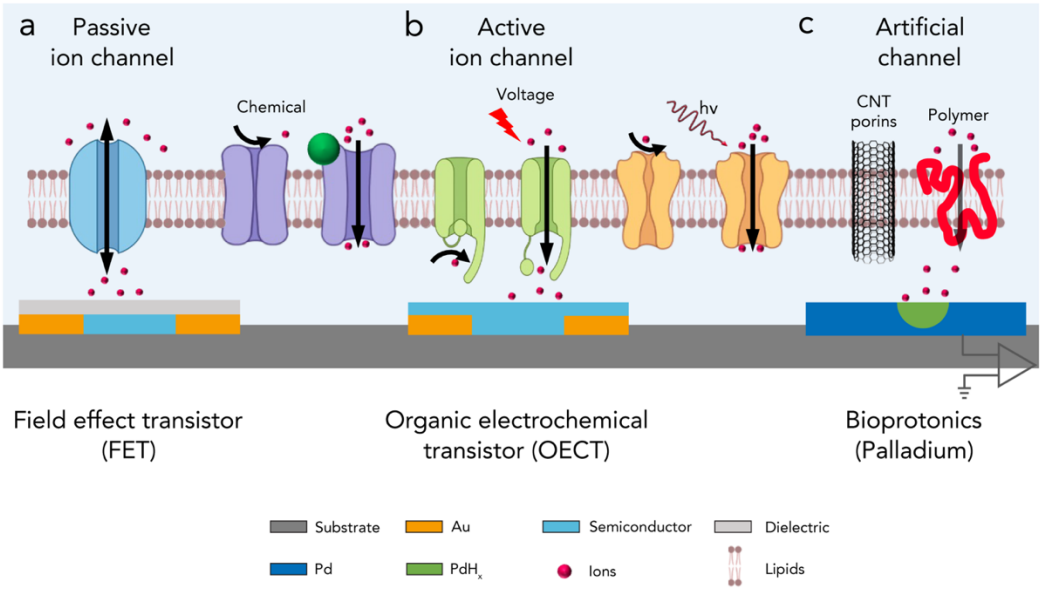


Figure 8: Schematic representation of transmembrane channels and bioelectronics. Top: (a) Passive transmembrane protein, (b) active transmembrane protein (Chemical, voltage, light-activated channel), and (c) artificial channel (Carbon nanotube porin and polymer-based channel). Bottom: Field effect transistor (FET), organic electrochemical transistor (OECT), and bioprotonics.

4.2 Electrodes for Electrochemical Impedance Spectroscopy (EIS) and Proton Conducting PdHx electrodes

In addition to active field effect devices, electrodes made of metal or polymer can be used to record signals from transmembrane channels using EIS or PdH_x electrodes that

are able to transduce H^+ signals into electronic signals[93]. EIS involves a working electrode, a counter electrode, and a reference electrode in its setup (Figure 9a). EIS measures the impedance between the working electrode and the solution electrolyte and uses the resulting data to fit an equivalent circuit, which includes both resistance and capacitance components. EIS can also be used for biosensing when the working electrode surface is functionalized with redox species, allowing for the detection and quantification of specific biological targets through changes in impedance and resistance. This method is able to analyze the concentration of ions/biomolecules, charge transfer, and resistance of electrolytes, making it a powerful tool for studying and understanding interfacial properties such as lipid bilayers/transmembrane channels, antigen-antibodies, aptamers, receptors, and enzymes[94].

Many transmembrane channels, including ATPase and bacteriorhodopsin, are proton conductors[95-98]. Pd/PdH_x contacts are useful for measuring the conductivity of these channels, taking advantage of the reversible redox reaction of H^+ at the Pd/solution interface and subsequent physisorption to create PdH (Figure 9b). For $V < 0$ applied to the Pd contact, an H^+ takes an electron from the contact to reduce to H and H subsequently absorbs onto the Pd surface to create PdH_x. This transfer results in an increase in solution pH. For every H^+ transferred from the solution to PdH_x an electron flows from the circuit into the Pd electrode. Therefore, measuring electronic current provides a one-to-one correlation with the H^+ current flowing through the transmembrane channel[99]. For $V > 0$, oxidization takes place at the Pd surface, releasing H^+ from PdH_{ads}, and increasing the concentration of H^+ in the solution while decreasing

the pH (Figure 9c). These reactions depend on the difference in protochemical potential between the Pd/PdH_x contact and the solution and are pH dependent.[93] For example, at low pH, with high H^+ in solution and high activity, H^+ may transfer directly from the solution into the Pd even for V = 0. The ability to measure H^+ current with PdH_x contacts makes them a suitable alternative to EIS measurements when using proton-conducting membrane channels[95-98].

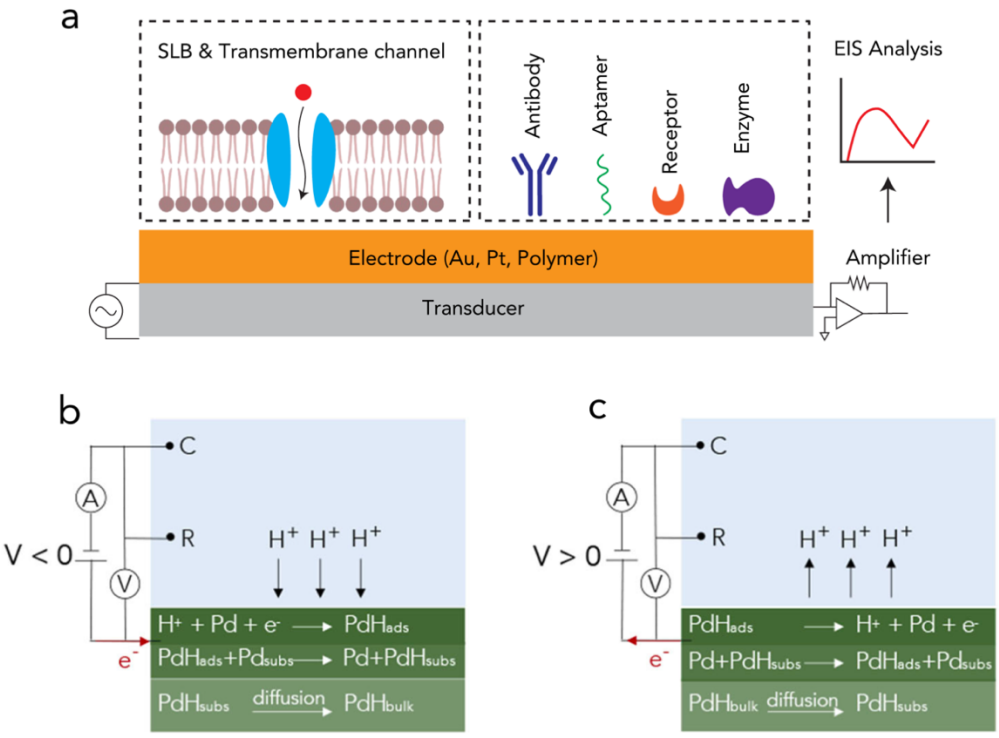


Figure 9: Schematics of bioelectronic platforms with conducting contacts. (a) SLBs on single electrodes for electrochemical measurement. (b) With an applied negative bias, H^+ transports to the Pd/solution surface and is absorbed onto the surface, then onto the Pd subsurface layer, and finally diffuses into the bulk layer to acquire PdH_{bulk}. (c)

With an applied positive bias, H^+ is initially released from the surface PdH_{ads}, then from the subsurface layer Pd_{subs} to the surface PdH_{ads} and further diffuses from PdH_{bulk}.

4.3 Bioelectronic platforms with supported lipid bilayer and transmembrane channels

1D nanostructures are well-suited for biosensing and diagnostics as they have comparable dimensions to biological molecules[100,101]. Researchers have combined silicon nanowire (SiNW) based FETs with SLBs and incorporated two transmembrane channels, gramicidin A (gA) and alamethicin (ALM)[102]. With gA, the SiNW conductivity becomes pH-dependent because gA allows H^+ ions to cross the lipid bilayer onto the SiNW surface. These H^+ ions change the surface pH, affecting the charged state of the surface -OH groups, effectively gating the SiNW. 2D nanomaterials possess several advantages for biosensing, including low noise, scalability, high surface-to-volume ratio, and compatibility with biomaterials, making them effective transducers of biosensors[103-105]. Among 2D materials, molybdenum disulfide (MoS_2) is particularly advantageous for biosensing due to its bandgap, which allows for integration with standard FET architectures, unlike graphene. MoS_2-based biosensors are capable of sensing pH, DNA hybridization, and proteins[103-105]. Bioprotonic devices use Pd/PdH_x contacts to translate H^+ currents into electronic currents and vice versa, forming a versatile interface with SLBs given that many transmembrane channels are proton conductors (Figure 10)[106]. The Pd/PdH_x working electrode, Ag/AgCl counter and reference electrode are used in this setup. A voltage

(V_{H+}) applied between the Pd/PdH_x working electrode and reference causes a current(i_{H+}) to flow. With V_{H+} is negative, protons transfer from the solution into the Pd/PdH_x contact. When V_{H+} is positive, protons transfer from the Pd/PdH_x contact into the solution.

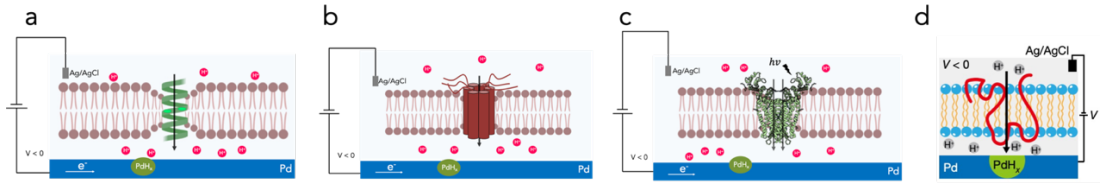


Figure 10: (a) Schematic of the bioprotonic devices integrated with passive ion channel gA and (b) active ion channel ALM, supporting the flow of H^+ across the SLB upon application of a voltage to the PdH_x contact. Reproduced with permission[106]. Copyright 2016, Springer Nature. (c) the bioprotonic device integrated with a light-activated ion channel consisting of deltarhodopsin with SLB and Pd/PdH_x contacts enables control of H^+ flow. Reproduced with permission[107]. Copyright 2016, Wiley-VCH. (d) Pd/PdH_x is used to measure the H^+ conductivity of a synthetic transmembrane protein, RHPs. Adapted with permission[92]. Copyright 2020, Springer Nature.

RESEARCH CONTRIBUTION

5. Design, improvement and applications of the anion hydrogel

5.1 Correlating protonic Conductivity and Microstructure in Polyelectrolyte Hydrogels

Hydrogels have become the material of choice in bioelectronic devices because their high-water content leads to efficient ion transport and a conformal interface with biological tissue. While the morphology of hydrogels has been thoroughly studied, systematical studies on their ionic conductivity is less common. Here, we present an easy-to-implement strategy to characterize the ionic conductivity of a series of polyelectrolyte hydrogels with different amounts of monomer and crosslinker and correlate their ionic conductivity with microstructure. Higher monomer increases the ionic conductivity of the polyelectrolyte hydrogel due to the increased charge carrier density, but also leads to excessive swelling that may cause device failure upon integration with bioelectronic devices. Increasing the amount of crosslinker can reduce the swelling ratio by increasing the crosslinking density and reducing the mesh size of the hydrogel, which cuts down the ionic conductivity. Further investigation on the porosity and tortuosity of the swollen hydrogels correlates the microstructure with the ionic conductivity. These results are generalizable for various polyelectrolyte hydrogel systems with other ions as the charge carrier and provide a facile guidance to design

polyelectrolyte hydrogel with desired ionic conductivity and microstructure for applications in bioelectronic devices.

5.1.1 Introduction

Hydrogels are crosslinked three-dimensional polymeric networks capable of retaining a significant fraction of water within the polymer chains without dissolving[49]. Hydrogels were first used for contact lenses in the 1960's[50,51], and have found many bioengineering applications since. Their high-water affinity and porous nature make them good scaffolds to load substances (functional nanomaterials and cells) for applications in drug delivery[52], wound dressing[51,53], and tissue engineering[54,55]. Specifically, the composite of hydrogels and conducting polymers play a critical role at the interface between electronic devices and biological systems for neuronal recording and stimulation[56,108-110], which not only reduces the impedance but also reduces mechanical mismatch and possible damage to biological tissue[111]. Additionally, hydrogels are wet allowing diffusion of ions and molecules mimicking the physiological environment of cells and tissue and so they are intrinsic ionic conductors[112]. Ionic conductors are particularly important because biological systems use ions and small molecules for information processing and not electrons and holes like semiconductor devices[59,113]. Hydrogels are good candidate to transfer information between biological system and electronic devices in ion-based bioelectronic device, including ionic diodes[114], ionic transistors[115], basic logic circuits[116], and ion pumps[22,117-120]. Although small molecule diffusion in polyelectrolyte hydrogels is well studied for applications such as drug delivery[121], water desalination[122], and pressure sensors[123],

relatively less work exists on the study of ionic conduction of hydrogels and their integration with bioelectronic devices[124].

Polyelectrolyte hydrogels are charged polymer network with macro-ions fixed on the polymer chains, which can be obtained by crosslinking charged monomer into network structure[125]. Thus, the charged monomer and crosslinker affect the ionic conduction properties and microstructure of polyelectrolyte hydrogels by designing a series hydrogel with (1) varying amounts of monomer and a fixed amount of crosslinker, (2) varying amounts of crosslinker and fixed amount of monomer. For instance, 2-acrylamido-2-methylpropane sulfonic acid (AMPSA) as the monomer and poly (ethylene glycol) diacrylate (PEGDA) as the crosslinker. AMPSA is an ionic monomer widely used for the synthesis of polyelectrolyte hydrogels because of its strongly ionizable sulfonate group that dissociates entirely in most of the pH range, and therefore hydrogels derived from AMPSA contain a high number of mobile counter ions[126]. PEGDA is commonly used as the crosslinker in the free-radical polymerization of AMPSA hydrogel, and it is water-soluble, non-toxic, and suitable for biomedical applications[127]. Many studies have been reported on the morphological and mechanical properties of AMPSA/PEGDA polyelectrolyte hydrogel as a function of their ionic group content. For example, Freeman et al. showed that the water uptake and ion sorption of AMPSA/PEGDA hydrogel increases with fixed charge density[128]. Durmaz and co-workers have reported that the elastic modulus of hydrogels first increases with higher charge density but then decreases continuously. Recently, Berggren and co-workers used AMPSA/PEGDA polyelectrolyte hydrogel as the ion exchange

membrane for the electrophoretic delivery of different ionic species[129]. In this paper, we present a comprehensive study on both the ionic conduction properties and the microstructure of a series of AMPSA/PEGDA hydrogels (Figure 11). We found that hydrogels with higher AMPSA show higher ionic conductivity due to the increased ionized groups and charge carrier density, but also results in excessive water absorption and hydrogel swelling that is detrimental to the integration of hydrogels with bioelectronic devices. By increasing the amount of PEGDA, we reduced the swelling behavior but the ionic conductivity is also decreased. The hinderance of hydrogel microstructure is similar to different ionic species and we further investigated the porosity and tortuosity and correlated the microstructure with the ionic conductivity quantitatively. These results provide simple design rules for tuning hydrogel microstructure and ionic conductivity for applications in bioelectronic devices.

5.1.2 Results

We prepared AMPSA/PEGDA hydrogels (Table 1) by free radical solution polymerization in the presence of photo-initiator (1-[4-(2-hydroxyethoxy)-phenyl]-2-hydroxy-2-methyl-1-propanone, Irgacure 2959) following a previously published procedure (Figure 11)[130].

Table 1:

	AMPSA (M)	PEGDA (M)	Photo-Initiator (M)
AP/1/0.5	1	0.5	0.05
AP/2/0.5	2	0.5	0.05

AP/3/0.5	3	0.5	0.05
AP/4/0.5	4	0.5	0.05
AP/2/0.1	2	0.1	0.05
AP/2/0.3	2	0.3	0.05
AP/2/0.5	2	0.5	0.05
AP/2/0.7	2	0.7	0.05

The crosslinked hydrogel has counterions and water molecules in the polymeric network, and fixed charges on the chains (Figure 11a and b). The hydrogel is transparent and absorbs water when exposed (Figure 11c). To measure the ionic conductivity of the hydrogel, we made the hydrogel into an ionic resistor by filling the hydrogel precursor solution into the glass capillary fiber with a modified surface and crosslinked the solution in situ using UV exposure (Figure 12 and 13). Figure 11d and 11e show a two-terminal experiment setup for the ionic conductivity measurement: the hydrogel fiber is an ionic conductor connecting two 100 mM HCl electrolytes, which ensured that H^+ are the dominant charge carriers in the hydrogel. AgCl wires immersed in the electrolytes serve as the ion-to-electron transducer following the electrochemical reaction, $Ag + Cl^- \leftrightarrow AgCl + e^-$, and close the circuit. For initial measurements, we used 100 mM HCl in both of the electrolytes, and assumed that H^+ are the dominant charge carriers in the hydrogel.

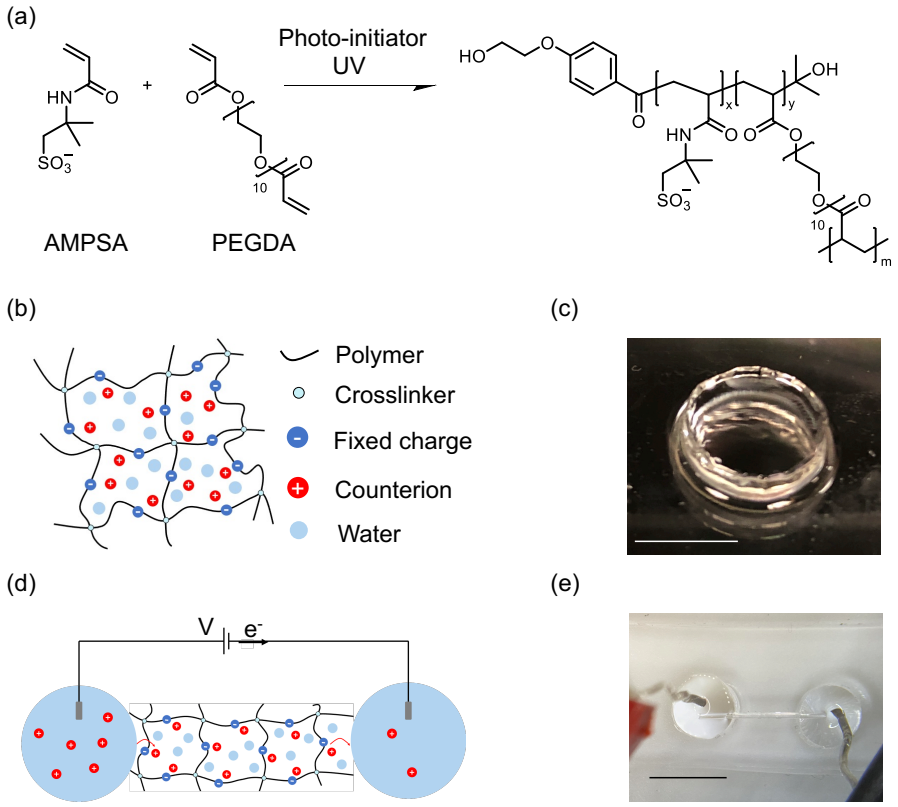


Figure 11: (a) Hydrogel polymerization reaction with AMPSA as the monomer, PEGDA as the crosslinker in the presence of the photo-initiator. (b) Schematic of the crosslinked polyelectrolyte hydrogel with fixed charges on the chain, counterions and water molecules in the polymetric network. (c) Optical image of the bulk hydrogel. Scale bar: 5 mm. (d) Schematic of the hydrogel ionic conductivity measurement experiment setup. A voltage (V) across the AgCl electrodes drives H^+ to move through the hydrogel in the capillary fiber, and the ionic flux is translated into an electronic current by the electrochemical reactions at the Ag/AgCl contacts. (e) Optical image of the hydrogel ionic conductivity measurement experiment setup. Scale bar: 5 mm. The

hydrogel capillary fiber is between two electrolyte chambers made from PDMS, and AgCl wires are used as the electrode contacts in each chamber.

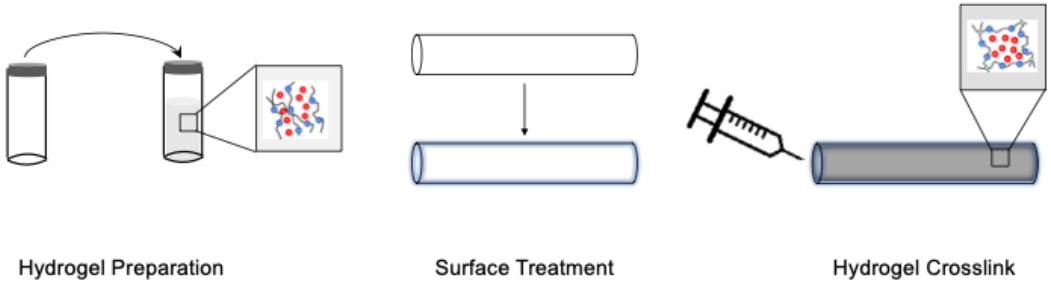


Figure 12: Hydrogel resistor fabrication process.

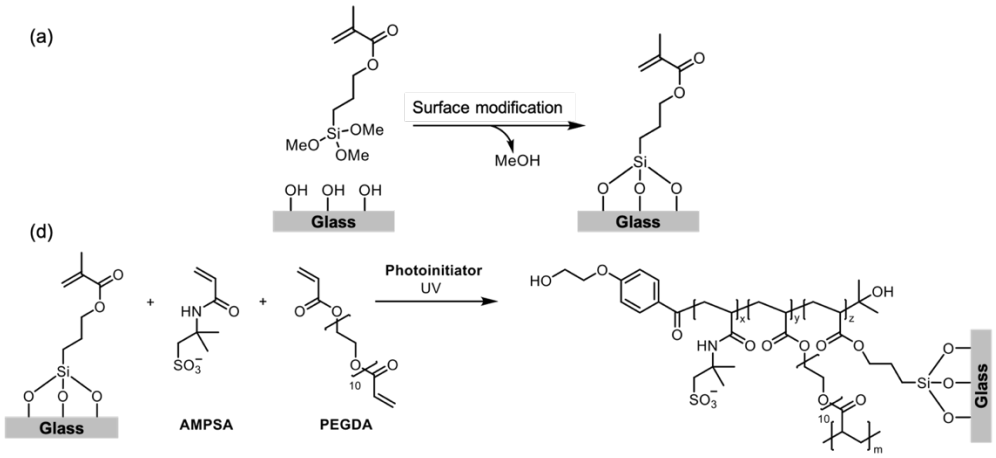


Figure 13: (a) The reaction between the glass and A174. (b) The reaction of hydrogel polymerization and covalent bonding in the glass capillary fiber.

We calculated the resistance (R) and ionic conductivity (δ) of the hydrogel using Equation 5 and Equation 6, respectively. This approach is simple compared to electrochemical impedance spectroscopy and does not require complicated device fabrication in the cleanroom or expensive equipment such as potentiostat[131-133].

$$R = \frac{V}{I} = \frac{L}{A\delta} \tag{5}$$

$$\delta = \frac{LI}{AV} \tag{6}$$

where R is the resistance, V is the applied voltage, I is the measured electrical current, A is the cross-section area of the capillary fiber, and δ is the ionic conductivity.

Equation 7 is a general expression of conductivity, and ionic conductivity is usually a summary of all mobile species in the system, where q is value of charge, z_i is the charge of each ion, n_i is charge carrier density per unit volume, μ_i is the mobility of each species.

$$\delta = \sum_i n_i |z_i| q \mu_i \tag{7}$$

In the case of a single ion type contributing to the conductivity, the summation is reduced to one term. The mobility of the ion can be expressed with the Einstein relationship (Equation 8) in term of the diffusion coefficient (D) of the ion in water, where K_B is the Boltzmann constant and T is the absolute temperature.

$$\mu = \frac{D}{k_B T} \tag{8}$$

However, ion transport in polyelectrolyte hydrogels is slower than that in the bulk electrolyte because of the interaction of the ions with the hydrogel microstructure. To take this effect into account, we can replace D with the effective diffusion coefficient (D_{eff}) in Eq (8) to get the ion mobility in a specific hydrogel[119]. The overall conductivity can then be expressed using Equation 9:

$$\sigma = n \frac{q D_{eff}}{k_B T} \tag{9}$$

First, we measured the ionic conductivity of all the hydrogels and found that the ionic conductivity increases with more AMPSA and less PEGDA (Figure 14a). When we increase AMPSA from 1 M to 4 M, the ionic conductivity increases from 8.7 ± 0.8 S/m to 11.6 ± 0.2 S/m. When we increased the PEGDA from 0.1 M to 0.7 M, the ionic conductivity decreases from 14.7 ± 0.3 S/m to 9.7 ± 0.8 S/m (Figure 15). AP/2/0.1 hydrogel shows the highest ionic conductivity to be 14.7 ± 0.3 S/m, which is similar to what has been reported[66,129]. AP/1/0.5 shows the lowest conductivity, 8.7 ± 1.8 S/m. To understand how AMPSA and PEGDA affect ionic conductivity, respectively, we further studied their influence on the change of charge carrier density and effective diffusion coefficient.

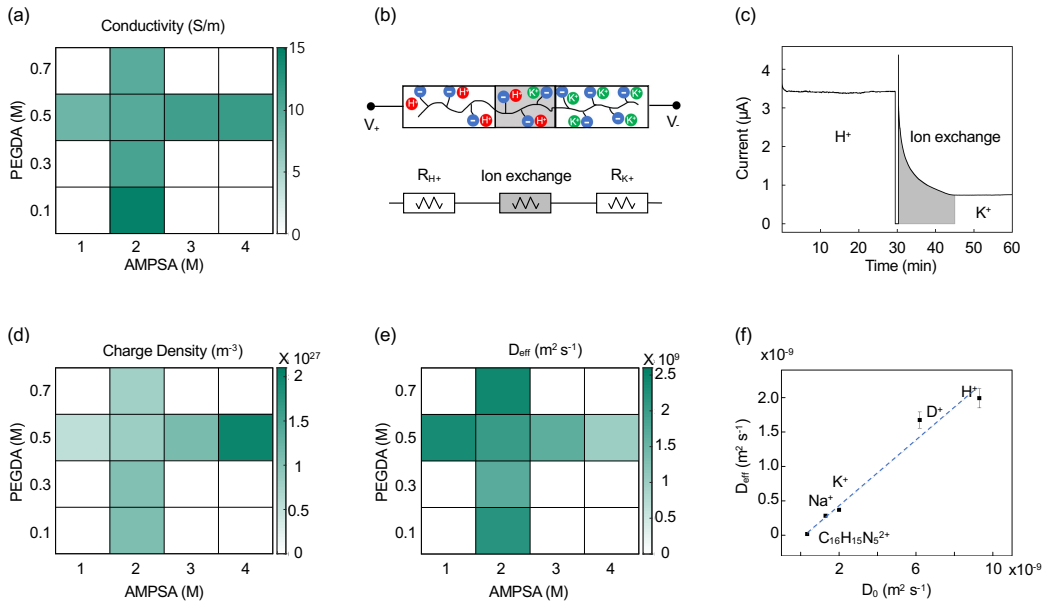


Figure 14: (a) Ionic conductivity of hydrogels as a function of AMPSA and PEGDA content. With more AMPSA and less PEGDA, hydrogels exhibit higher conductivity.

(b) Schematic of charge carrier density measurement using the ion exchange process. (c) Current response when we change the charge carrier from H^+ to K^+. During the ion exchange process, the current under the gray area is integrated and leads to the charge carrier density. (d) Charge carrier density of the hydrogels as a function of AMPSA and PEGDA. The charge carrier density increases with AMPSA content because AMPSA directly provides charged sites, and slightly decreases with more PEGDA. (e) Effective diffusion coefficient (D_{eff}) of the hydrogels as a function of AMPSA and PEGDA. The D_{eff} decreases with more AMPSA and shows no obvious trend while changing PEGDA. (f) Relationship between effective diffusion coefficient (D_{eff}) and bulk diffusion coefficient (D_0) of Na^+, K^+, H^+, D^+, DAPI in AP/2/0.5 hydrogel.

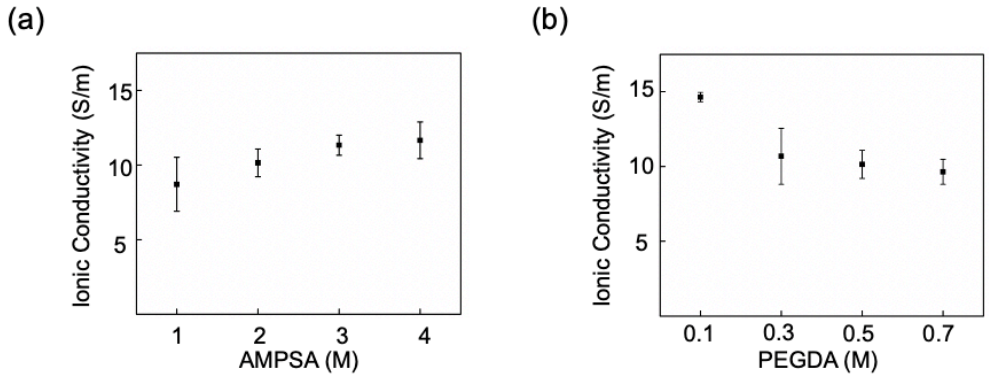


Figure 15: Dependence of ionic conductivity on AMPSA and PEGDA.

Assuming that the hydrogel is electroneutral, the mobile charge carrier density (n) in the hydrogel equals to the fixed charge density of the polymetric network.[119] Here, we measure the fixed charge density of the polyelectrolyte hydrogel using an ion exchange

process with the same experiment setup in the ionic conductivity measurement (Figure 14b). First, we use 100 mM HCl as the electrolyte, apply 0.8 V and measure the currents. When all the charged groups in the polyelectrolyte hydrogels are compensated with H^+, the resistance of the ionic conductor is stable and the current reaches an equilibrium. Second, we change the electrolyte to 100 mM KCl. The counter ions H^+, at the fixed charge sites, are gradually exchanged by K^+, which has lower mobility and therefore the current decreased. When all the H^+ are replaced by K^+, the resistance of the ionic conductor is only dependent on K^+, and the current became steady again. Here we assume the total number of fixed charges equals to the transferred ionic charges between the two steady states, which can be estimated by integrating the electronic current with time (Figure 14c).

The hydrogel glass fiber has a precisely defined geometry, so we can easily have an estimate of the mobile charge density in each hydrogel by dividing the number of charges by the hydrogel volume. Figure 14d shows that the charge density increases with higher AMPSA and less PEGDA. In Figure 16, the charge carrier density increases from $5.6 \pm 0.2 \times 10^{26}$ m^{-3} to $1.6 \pm 0.5 \times 10^{27}$ m^{-3} when we increase AMPSA from 1 M to 4 M, which is more significant than that of hydrogels with different PEGDA, from $1.1 \pm 0.1 \times 10^{27}$ m^{-3} to $7.7 \pm 0.1 \times 10^{26}$ m^{-3}. This is because AMPSA provides ionized sulfonate groups directly. Even PEGDA doesn't directly supply fixed charges, its influence on the crosslinking density changes the charge carrier density in a moderate manner.

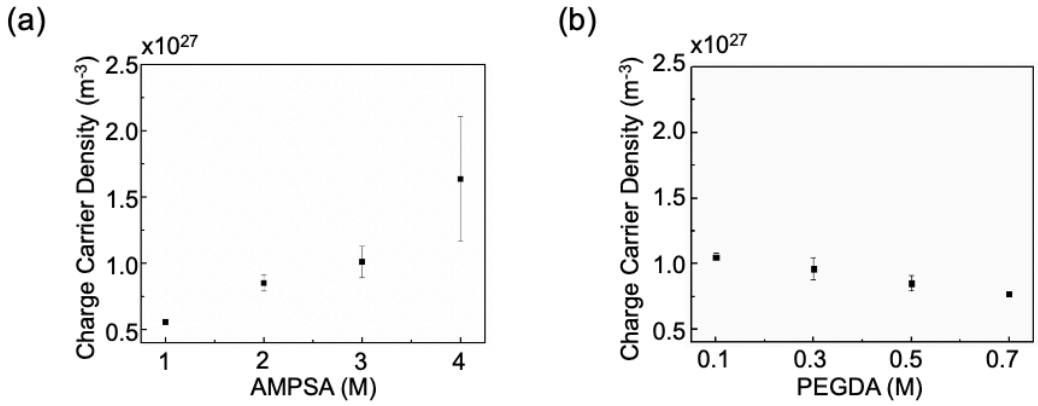


Figure 16: Dependence of charge carrier density on AMPSA and PEGDA.

Then, we calculated the effective diffusion coefficient of H^+ in each hydrogel with the ionic conductivity and charge carrier density following Eq (9) (Figure 17 and Table 2). Figure 14e shows that the D_{eff} decreases with higher AMPSA, from $2.5 \pm 0.5 \times 10^{-9}$ m^2s^{-1} to $1.1 \pm 0.4 \times 10^{-9}$ m^2s^{-1}, which are in the same magnitude of what reported so far[134]. However, D_{eff} does not show monotonical change when we change PEGDA. The reason could be that effective diffusion coefficient is affected by more complicated factors.

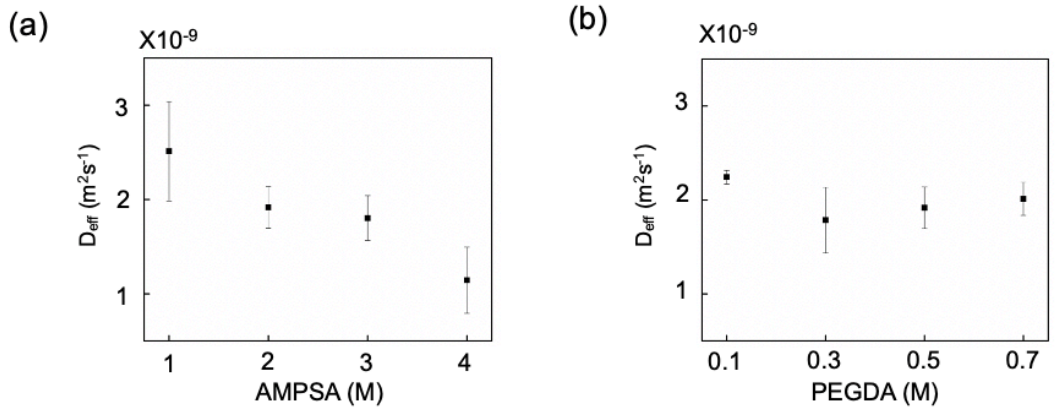


Figure 17: Dependence of effective diffusion coefficient (D_{eff}) on AMPSA and PEGDA.

Table 2: Electrical Properties of hydrogel.

	Conductivity (S/m)	Charge Density ($/m^3$)	Mobility ($m^2/V \cdot s$)	Effective Diffusion coefficient (D_{eff}) (m^2/s)
AP/1/0.5	8.7 ± 1.8	$5.6 \pm 0.2 \times 10^{23}$	$9.8 \pm 2.0 \times 10^{-8}$	$2.5 \pm 0.5 \times 10^{-9}$
AP/2/0.5	10.1 ± 0.9	$8.5 \pm 0.6 \times 10^{23}$	$7.5 \pm 0.9 \times 10^{-8}$	$1.9 \pm 0.2 \times 10^{-9}$
AP/3/0.5	11.3 ± 0.7	$1.0 \pm 0.1 \times 10^{24}$	$7.0 \pm 0.9 \times 10^{-8}$	$1.8 \pm 0.2 \times 10^{-9}$
AP/4/0.5	11.6 ± 1.2	$1.6 \pm 0.5 \times 10^{24}$	$4.4 \pm 1.4 \times 10^{-8}$	$1.1 \pm 0.4 \times 10^{-9}$
AP/2/0.1	14.7 ± 0.3	$1.1 \pm 0.1 \times 10^{24}$	$8.7 \pm 0.3 \times 10^{-8}$	$2.2 \pm 0.1 \times 10^{-9}$
AP/2/0.3	10.7 ± 1.9	$9.6 \pm 0.8 \times 10^{23}$	$6.9 \pm 1.4 \times 10^{-8}$	$1.8 \pm 0.3 \times 10^{-9}$
AP/2/0.5	10.1 ± 0.9	$8.5 \pm 0.6 \times 10^{23}$	$7.5 \pm 0.9 \times 10^{-8}$	$1.9 \pm 0.2 \times 10^{-9}$
AP/2/0.7	9.7 ± 0.8	$7.7 \pm 0.1 \times 10^{23}$	$7.8 \pm 0.7 \times 10^{-8}$	$2.0 \pm 0.2 \times 10^{-9}$

Here we consider D_{eff} as a description of the hinderance of hydrogel microstructure on the ion transport, and measured the ionic conductivity and D_{eff} of different ions and small molecules using AP/2/0.5 hydrogel. By changing the electrolyte that supplies ions to the hydrogel, we changed the charge carriers in the hydrogel among H^+, D^+, Na^+, K^+, and $C_{16}H_{12}N_5^{2+}$. While we applied 0.8 V across the same hydrogel fiber (AP/2/0.5 hydrogel). We measured the ionic conductivity of hydrogel corresponding to different ionic species, and calculated the D_{eff} of different ionic species (H^+, D^+, Na^+, K^+, and $C_{16}H_{12}N_5^{2+}$) (Table 3). The results of H^+ and K^+ are almost the same as what reported

by Simon and co-workers.[129] In Figure 14f, we plotted the relationship of D_{eff} and the diffusion coefficient in bulk solution, D_0. The linear relationship ($R^2 = 0.98$) indicates that the effect of the hydrogel microstructure on the ion and ionic species transport is a property of the hydrogel itself and it is generalizable in this transport regime in which we assume that the size of the ionic species is much smaller than the pore size of the hydrogel.

Table 3: The electrical properties of AP/2/0.5 with different ions as the charge carriers.

Charge Carrier	D_0 (m^2/s)	D_{eff} (m^2/s)
H^+	9.30×10^{-9}	$1.99 \pm 0.14 \times 10^{-9}$
D^+	6.20×10^{-9}	$1.67 \pm 0.12 \times 10^{-9}$
K^+	2.00×10^{-9}	$3.69 \pm 0.26 \times 10^{-10}$
Na^+	1.30×10^{-9}	$2.83 \pm 0.21 \times 10^{-10}$
$C_{16}H_{15}N_5^{2+}$	3.40×10^{-10}	$1.79 \pm 0.64 \times 10^{-11}$

To gain further insights, we characterize the hydrogel microstructure as a function of composition and relate the microstructure to D_{eff}. When a hydrogel is brought into contact with water, water diffuses into the pre-existing or dynamically formed spaces

between hydrogel chains due to the osmotic pressure.[126] The polymetric network expands and results in swelling of the hydrogel, which involves larger segmental motion and ultimately increased separation between hydrogel chains (Figure 18a)[135]. The swelling capability is important for applications such as drug delivery and ion-based bioelectronics. However, when we integrate hydrogels with bioelectronic devices, excessive swelling behavior damages the device (Figure 18b). Thus, understanding the mechanism of hydrogel swelling and methods to regulate this property is of great significance for their integration with the bioelectronic devices. We soaked all the hydrogels in excessive DI water for 48 hrs to reach equilibrium before taking the pictures in Figure 18c-j. When we increase AMPSA from 1 M to 4 M, hydrogel swelling ratio increases from 268 ± 16 % to 331 ± 20 %. This is mainly because the increase of the counterions inside the hydrogel, which increases the osmotic pressure that swells the hydrogel[136]. On the other hand, when we increase the crosslinker from 0.1 M to 0.7 M, the swelling ratio is dramatically reduced from 1418 ± 153 % to 242 ± 1 %. The crosslinker has a major effect on the polymer chains branching and network. Thus, the network space is decreased with higher crosslinker and less water enters the hydrogel. This result is similar with the study from Patel and co-workers on superporous hydrogels[137].

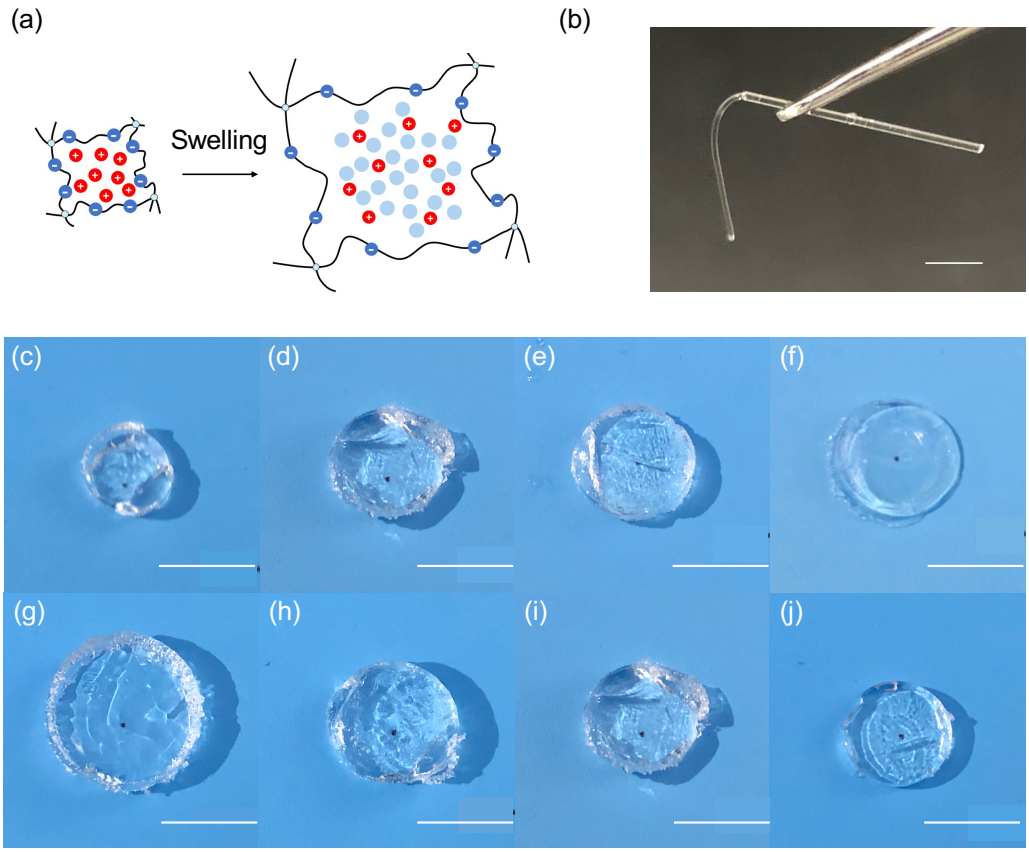


Figure 18: (a) Schematic of water diffusing into the hydrogel due to osmotic pressure, which results in swelling of the hydrogel and enlarged pores. (b) Hydrogel swells in the glass capillary fiber. Scale bar: 2 mm. Optical images of swollen (c) AP/1/0.5, (d) AP/2/0.5, (e) AP/3/0.5, (f) AP/4/0.5, (g) AP/2/0.1, (h) AP/2/0.3, (i) AP/2/0.5, (j) AP/2/0.7 hydrogels.

To gather further understanding, we conducted SEM characterization to determine the morphology of the polymetric network and understand the average pore size of all the hydrogels. In Figure 19(a-d), all hydrogels except AP/1/0.5 present well-defined pores

with average size ranging from 12 ± 7 um^2 to 802 ± 94 um^2. AP/1/0.5 seems to have a structure with few pores, which aligns well with its relatively lower swelling ratio. The nonporous structure reduces water absorption and therefore ion transport, but nonporous hydrogels are good candidates for applications that require low swelling ratio or good mechanical properties[138]. AP/2/0.5, AP/3/0.5, and AP/4/0.5 hydrogels are similar in the average pore sizes, 39 ± 82 um^2, 54 ± 33 um^2, and 33 ± 27 um^2, respectively. In comparison, when PEGDA is increased from 0.1 M to 0.7 M, the average pore sizes of hydrogels show significant decrease: 802 ± 93 um^2, 275 ± 121 um^2, 39 ± 18 um^2, 13 ± 7 um^2, as shown in Figure 19e-h. PEGDA has a higher impact on the hydrogel pore size, which is in consistent with their swelling performance in Figure 18.

Diffusion coefficient (D_{eff}) is dependent on the porosity (ε) and tortuosity (τ) of the porous media (Equation 10)[139]. Here we use Eq 10 to correlate the microstructure and the ionic conductivity.

$$D_{eff} = \frac{\varepsilon}{\tau} D_0 \tag{10}$$

where D_0 is the diffusion coefficient of H^+ in bulk solution (9.31 x 10^{-9} m^2/s). ε is the porosity and τ is the tortuosity.

First, we characterize the porosity of hydrogels (Figure 19i), which is defined as the ratio of the pores' volume and the total volume of the hydrogel (Equation 11).

$$\varepsilon = \frac{V_{pore}}{V_{total}} \tag{11}$$

In Figure 19j, when we increase the AMPSA from 1 M to 3 M, the porosity increases from 0.39 ± 0.04 to 0.56 ± 0.02 because the higher osmotic pressure[126]. The porosity doesn't further increase and even decrease to 0.52 ± 0.02 when we increase the AMPSA to 4 M, which might be due to the ion pair formation from the high ionic group contents[126]. In comparison, the porosity decreases from 0.74 ± 0.02 to 0.48 ± 0.01 when we increased the PEGDA from 0.1 M to 0.5 M because of the higher polymetric network density (Figure 19k). However, the porosity doesn't further decrease when we increase the AMPSA to 0.7 M because of the finite shrinkage of the network chains. Apparently, the influence of PEGDA on the porosity is more significant than APMSA, and these results match well with the SEM images and swelling behaviors.

Various definition and measurements of tortuosity have been reported from the perspective of engineers geologists and chemists[139,140], but rarely studied for hydrogels. In fact, hydrogels with low tortuosity is desired for supercapacitors[141] and ion-based bioelectronic devices, so the investigation on the hydrogel tortuosity is in demand. Figure 18l shows the definition of tortuosity: the ratio of the actual distance that ions travel between two points by following the microchannel of the hydrogel to the straight-line distance between the two points (Equation 12).

$$\tau = \frac{L}{X} \tag{12}$$

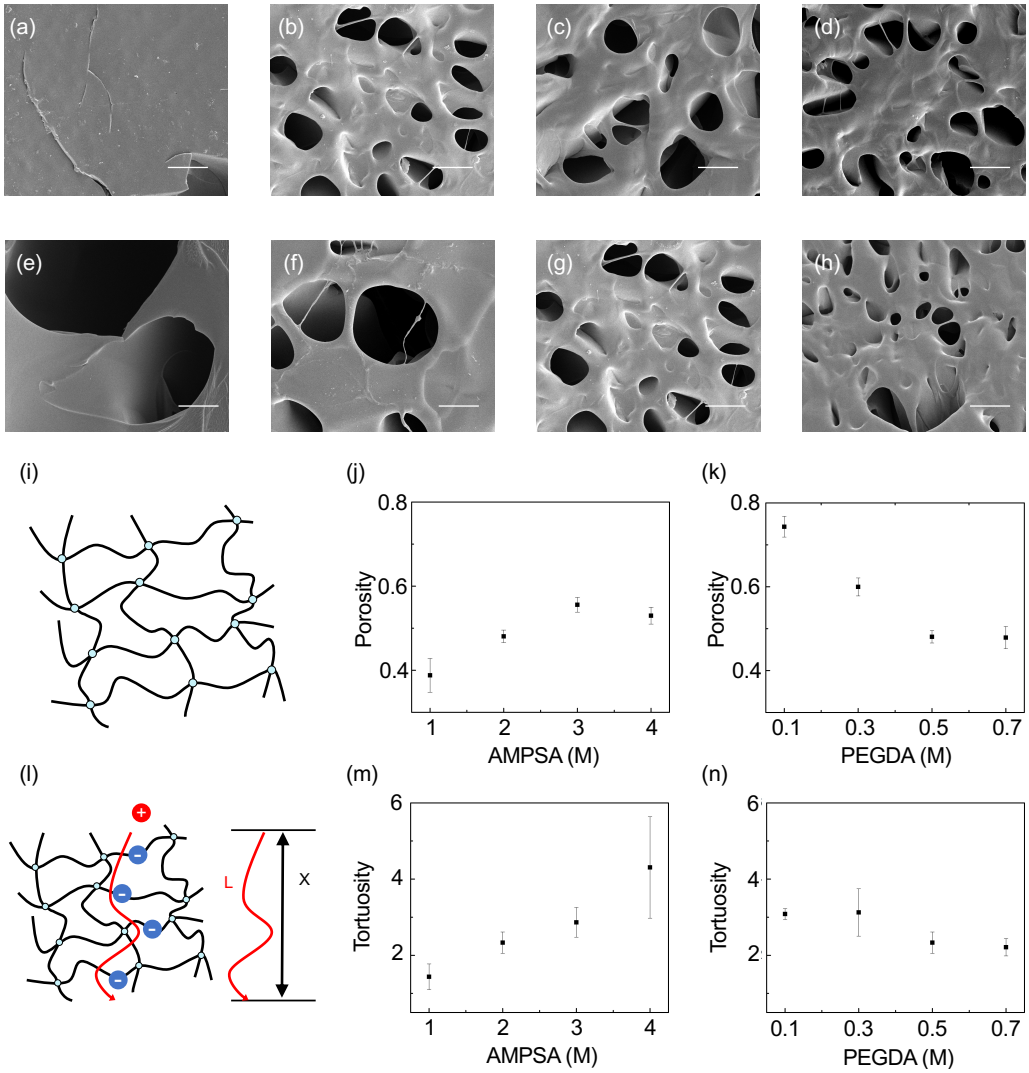


Figure 19: SEM of hydrogels: (a) AP/1/0.5, (b) AP/2/0.5, (c) AP/3/0.5, (d) AP/4/0.5, (e) AP/2/0.1, (f) AP/2/0.3, (j) AP/2/0.5, (h) AP/2/0.7 hydrogels. Scale bar: 10 µm. (i) Schematic of porosity. (j) Porosity change while changing AMPSA. (k) Porosity change while changing PEGDA. (l) Schematic of tortuosity. (m) Tortuosity change while changing AMPSA. (n) Tortuosity change while changing PEGDA.

A material with perfectly straight pores will have a tortuosity of 1[142]. Here we extracted the tortuosity from D_{eff} and ε, according to Eq 11. Figure 19m show the tortuosity increases with higher AMPSA, from 1.44 ± 0.34 to 4.31 ± 1.33, which could be attributed to the increased fixed charge sites that dictate the path ion movement[143]. Figure 19n shows that the tortuosity decreases with more PEGDA, from 3.08 ± 0.14 to 2.21 ± 0.23, because of the higher network density. Thus, the charged monomer influences the tortuosity more than the crosslinker in polyelectrolyte hydrogels (Figure 20 and Table 4).

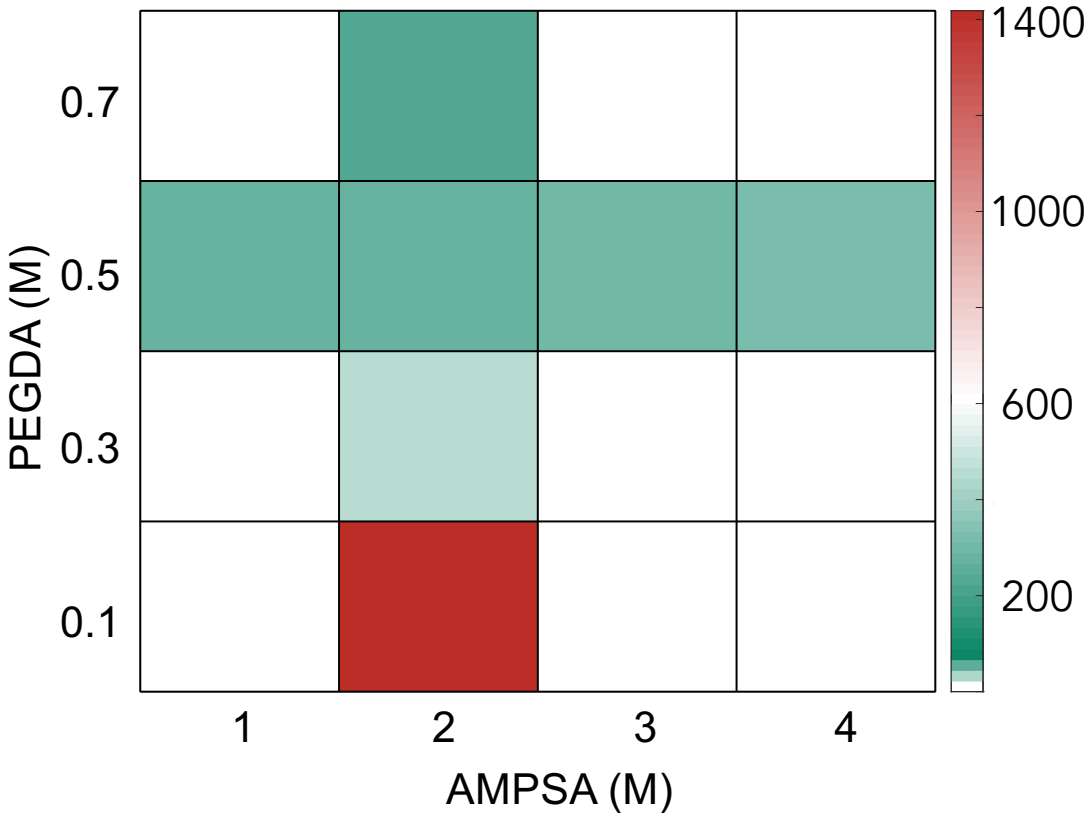


Figure 20: Swelling ratio of hydrogels as a function of AMPSA and PEGDA.

Table 4: Microstructure properties of the hydrogels.

	Swelling Ratio (%)	Porosity	Tortuosity
AP/1/0.5	268 ± 16	0.39 ± 0.04	1.44 ± 0.34
AP/2/0.5	285 ± 5	0.48 ± 0.01	2.33 ± 0.28
AP/3/0.5	298 ± 2	0.56 ± 0.02	2.87 ± 0.39
AP/4/0.5	331 ± 20	0.53 ± 0.02	4.31 ± 1.33
AP/2/0.1	1418 ± 153	0.74 ± 0.02	3.08 ± 0.14
AP/2/0.3	454 ± 12	0.60 ± 0.02	3.12 ± 0.62
AP/2/0.5	285 ± 5	0.48 ± 0.01	2.33 ± 0.28
AP/2/0.7	242 ± 1	0.48 ± 0.03	2.21 ± 0.23

5.1.3 Conclusion

In summary, we presented a comprehensive study on the electrical properties (the ionic conductivity, charge carrier density, and effective diffusion coefficient) and microstructure (swelling ratio, porosity, and tortuosity) of a series of polyelectrolyte hydrogel. We found that more AMPSA monomer results in higher ionic conductivity due to higher charge carriers directly compensated by sulfonate groups. The charge carriers also influence the hydrogel microstructure by altering the osmotic pressure between the polymetric network and the environment, and therefore the swelling ratios.

By further analyzing the hydrogel microstructure by SEM, porosity, and tortuosity, we found that the AMPSA can increase porosity and tortuosity of the hydrogels, but shows negligible influence on the pore size. However, the excessive hydrogel swelling from high AMPSA has the risk of device failure when the hydrogel is integrated in bioelectronic devices. On the other hand, we found that increasing PEGDA content crosslinker can reduce the amount of swelling by increasing the crosslinking density. The relationship between effective diffusion coefficient and porosity and tortuosity correlates the ionic conductivity and microstructure of hydrogels, which can be applied to other ions and even small charged molecules. By tuning the monomer and crosslinker, we provide a strategy to regulate the ionic conductivity and microstructure of the AMPSA/PEGDA hydrogels that could also be extended to other polyelectrolyte hydrogels and will enable applications of such materials in bioelectronic devices to control ionic signals directly.

5.1.4 Experimental Section/Methods

Hydrogel capillary fibers fabrication: AMPSA, PEGDA, and photo-initiator are mixed in water at room temperature following the protocols in Table 1. The hydrogel precursor solution was injected into the glass capillary fiber (50 um diameter, 10 cm long) and crosslinked under UV light (power: 8 mW / cm^2, wavelength 306 nm) for 5 min to finalize the ionic resistor fabrication. The fiber was cut into 5 mm length for the measurement of ionic conductivity and charge carrier density.

Ionic conductivity measurement: PDMS wells were used to isolate electrolytes and the hydrogel glass fiber was used to connect them (Figure 11e). All electrical measurements were performed using a computer controlled Autolab potentiostat PGSTAT128N with analytic software Nova 2.0, which simply supplies voltage and measures the current.

Swelling ratio measurement: First, we crosslinked 100 ul hydrogel solution in PDMS well (8 mm diameter) with UV exposure. Then, we placed each hydrogel sample in excessive distilled water at room temperature for 48 hours to reach the equilibrium. The weight of the swollen hydrogel was recorded as W_{wet}. Then we dried the hydrogel samples immediately using lyophilizer and recorded the weight of the dried hydrogel as W_{dry}. The swelling ratio is calculated by the following equation 13:

$$swelling\ ratio = \frac{W_{wet} - W_{dry}}{W_{wet}} \tag{13}$$

Porosity measurement: By substituting W_{wet} by W_{dry}, we got the weight of the water in all the hydrogel pores and therefore the volumes of the pores, V_{pore}. By dividing V_{pore} by the total volume of the hydrogel, 100 ul + V_{pore}, we calculated the porosity of each hydrogel. To achieve good precision, we measured 3 samples for each hydrogel in each measurement and took the average of the results.

SEM: First, we crosslinked 100 ul hydrogel solution in PDMS well under UV exposure. Then, we placed each hydrogel sample in an excess of water at room temperature for 48 hours in order to reach the equilibrium. Right after this, we froze the sample by

liquid nitrogen and left them in the lyophilizer for another 48 hours. The samples were sputtered with ~20nm of Au-Pd prior to imaging to prevent charging. We used a FEI Quanta 3D Dualbeam microscope operated with the electron beam at 5kV.

5.2 A Bioelectronic Device for Controlled Delivery of Ions and Biomolecules in Wound Healing

Wound healing is a complex physiological process that requires precise control and modulation of many parameters. Therapeutic ion and biomolecule delivery has the potential to beneficially regulate the wound healing process. However, achieving controlled delivery with a compact device with the ability to deliver multiple therapeutic species can be a challenge. Bioelectronic devices have emerged as a promising approach for therapeutic delivery. Here, we present a bioelectronic device designed to deliver ions and biomolecules for wound healing applications. The device incorporates ion pumps for targeted delivery of H+ and zolmitriptan to the wound site. In vivo studies using a mouse model further validated the device's potential for modulating the wound environment via H^+ delivery that decreased M1/M2 macrophage ratios. Overall, this bioelectronic ion pump holds promise for accelerating wound healing via targeted and controlled delivery of therapeutic agents to wounds. Continued optimization and development of this device could not only lead to significant advancements in wound healing strategies but also reveal new physiological information about the dynamic wound environment.

5.2.1 Introduction

Millions of people across the globe experience harmful impacts from both acute and chronic wounds[144]. In the United States alone, around 300,000 hospitalizations annually are linked to wounds[144]. Improved and innovative wound healing strategies are necessary to reduce the associated hospitalizations and healthcare costs[145]. Bioelectronic devices are one possible healing approach that bridges the gap between electronic control and complex biological processes like those of wounds[56,146]. For example, recent bioelectronic developments use flexible or microfluidic platforms to deliver electric field stimulation to rodent skin wounds or in vitro scratch wound assays for accelerated healing[145,147]. Other bioelectronic platforms incorporate the use of metal dots on polyester or cotton fibers to generate small potentials that are reported to aid in wound healing[148]. Another bioelectronic approach involves utilizing ion-selective membranes (IEMs) in devices to deliver specific ions and biomolecules to the wound site. An example of this kind of device is the electrophoretic ion pump[43,56]. Ion pumps can deliver ions and biomolecules directly to a specific target, like the surface of a wound, in order advantageously alter the biological environment[149,150]. This can result in promoting crucial cellular processes such as inflammation regulation, tissue regeneration, and pain alleviation[151,152].

Recent studies have demonstrated how bioelectronic ion pumps can deliver a range of ions such as K^+ [153], Ca^{2+} [154], H^+ [155], as well as neurotransmitters like acetylcholine (ACh)[156], gamma-aminobutyric acid (GABA)[157] and glutamate[158]. These ion pumps

typically deliver one therapeutic agent at a time. However, due to the complexity of the wound environment, simultaneous on-demand delivery of multiple agents could potentially enhance wound healing. To this end, our team has previously reported a bioelectronic electrophoretic ion pump capable of simultaneously delivering H^+, Na^+, and Cl^-ions[159]. The anti-inflammatory properties of zolmitriptan[160,161] and its ability to modulate neurogenic reactions[160] make it a promising candidate for wound healing. Research on migraines and meningitis shows that zolmitriptan reduces inflammation and vasodilation by inhibiting the release of proinflammatory neuropeptides from nerve fibers[160]. Because zolmitriptan is a selective 5-hydroxytryptamine 1B/1D receptor agonist it can activate serotonin receptors in the skin, with downstream pro-reparative outcomes[162,163]. This mechanism shows potential for zolmitriptan use in wound healing, particularly considering inflammation's vital role in the healing process. Building on these investigations, here we introduce an advanced bioelectronic device with the capacity to deliver ion such as H^+ alongside biomolecules such as zolmitriptan. To validate the device's practical application, we further conduct an in vivo study using a mouse wound model (Figure 21).

5.2.2 Results

The design of the bioelectronic device enables electronically programmable ionic and biochemical delivery to biological targets. In our study, we used wounds in a mouse model as the target (Figure 21A). The fabrication process of the device involves several steps, starting with the creation of 3D printed molds to form a two-layered

polydimethylsiloxane (PDMS) body. PDMS is a flexible and biocompatible polymer commonly used in the fabrication of medical devices[164,165]. The top layer of the PDMS body contains reservoirs (Figure 21B, left and middle) that hold cationic therapeutics in aqueous form, such as hydrogen ions (H^+) or protonated biomolecules such as zolmitriptan$^+$ (Z^+). To achieve controlled delivery of ions and biomolecules, the PDMS body integrates with a custom printed circuit board (PCB) (Figure 21B, right). The PCB serves as the control system for the device, allowing for programmable delivery of the therapeutic.

The device achieves ion and biochemical delivery via ion pump technology. The working mechanism of ion pumps is to deliver charged species from the reservoir, through the IEM, and to the target (Figure 21C). This transport occurs by applying a low voltage (V_{pump}) between the working electrode (WE) and the reference/counter electrode (RE/CE). Each reservoir of the device houses a metal wire that acts as a WE or RE/CE. Further, the aqueous solution in each reservoir interfaces with hydrogel that acts as the IEM in our system. The hydrogel contains 2-acrylamido-2-methylpropane sulfonic acid (AMPSA) and poly (ethylene glycol) diacrylate (PEGDA) and is selective to cationic species[166]. Thus, the ion pump selectively permits the passage of protonated ions and biomolecules while preventing the passage of anionic species.

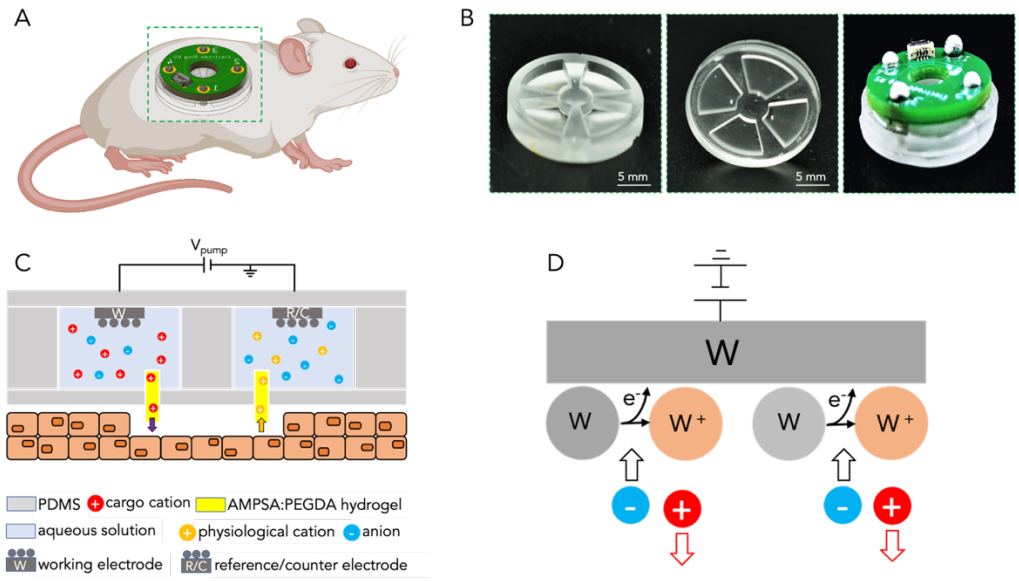


Figure 21: (A) The schematic of the bioelectronic device demonstrates its application in a mouse model. (B) The bioelectronic device consists of a 3D printed PDMS body featuring four reservoirs for solution storage. The body is securely bonded with a PDMS lid and integrated with a printed circuit board (PCB). (C) Schematics of the ion pumping process illustrate how the electric field drives protons towards the target through the ion-selective hydrogel (yellow). (D) The generalized electrochemical reaction for the ion-pump WE. The schematic illustrates the voltage-induced oxidation mechanisms which facilitate proton conduction.

The substance in the reservoir thus must be naturally positively charged or protonated through use of acidic solution. When V_{pump} is positive, cationic species from the reservoir at the WE electrophoretically transfer into the target through the IEM. This is due to oxidation reactions that occur at the WE (Figure 21D). To maintain charge neutrality, physiological cations exit the wound and enter the opposite reservoir at the

RE/CE. These physiological cations also serve as the charge carriers at the wound surface, thereby completing the circuit.

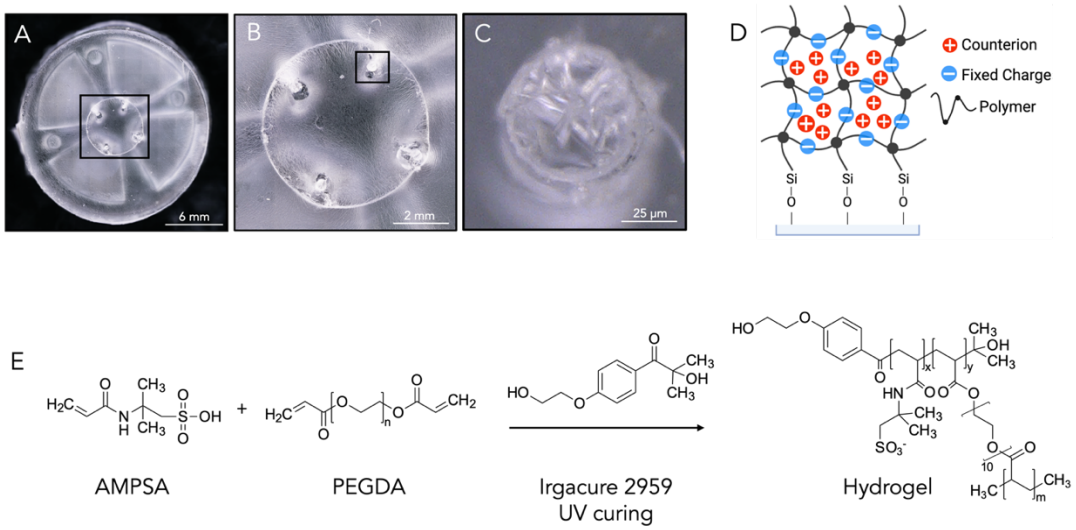


Figure 22: (A) An optical microscopy image of the wound-interfacing side of the device, (B) Zoomed-in image revealing the wound-interfacing PDMS and the openings of the capillary tubing filled with hydrogel. (C) A microscopy image of the bulk hydrogel within the glass capillary fiber. (D) A schematic representation of the crosslinked polyelectrolyte hydrogel, depicting fixed charges along the chain and counterions within the polymeric network. (E) Illustration of the hydrogel polymerization reaction, utilizing AMPSA as the monomer, PEGDA as the crosslinker, and the presence of a photo-initiator.

In order to deliver specific ion and biomolecules (H^+, and protonated zolmitriptan$^+$), we use four glass capillary fibers to house the cation-selective IEM. We insert the IEM-filled capillaries into the PDMS device where they can interface with the wound (Figure

22A, B). A zoomed-in optical microscope image reveals the openings of the capillary tubing and provides a visual of the bulk hydrogel (Figure 22C). The IEM is a crosslinked polyelectrolyte hydrogel made selective to cations through the presence of fixed negative charges within the polymeric network (Figure 22D). We achieve this through a hydrogel polymerization reaction, where AMPSA acts as the monomer and PEGDA acts as the crosslinker in the presence of a UV photoinitiator (Figure 22E). The hydrogel-filled capillaries require a preparation procedure that we have previously optimized[166].

To evaluate the devices' performance, we utilized a fluorescence microscope (Keyence BZ-X710) setup and an indicator dye for H^+ detection (Figure 23A). We first placed the devices on a target solution containing buffer along with the indicator dye. Next, we used a V_{pump} pulse (usually within a magnitude of 2 V, in this case referred to as V_{H+}) across the WE and RE/CE of each device for several minutes. V_{H+} enables the electrophoretic transfer of cations from the device reservoir (at the WE), through the IEM, and into the target solution. Concurrently, pre-existing cations in the target solution migrated through the IEM to the other reservoir (at the RE/CE). The observed changes in fluorescence intensity within the target solution corresponded to variations in ion concentration. On the other hand, the delivery of cationic biomolecules such as zolmitriptan required the use of high-performance liquid chromatography (HPLC) rather than fluorescence microscopy. The underlying principle of the device remained unchanged, as a positive V_{Z+} transfers protonated zolmitriptan$^+$ from the reservoir to

the target solution containing 0.01 M KCl. We maintained the same device setup, excluding the microscope (Figure 23B).

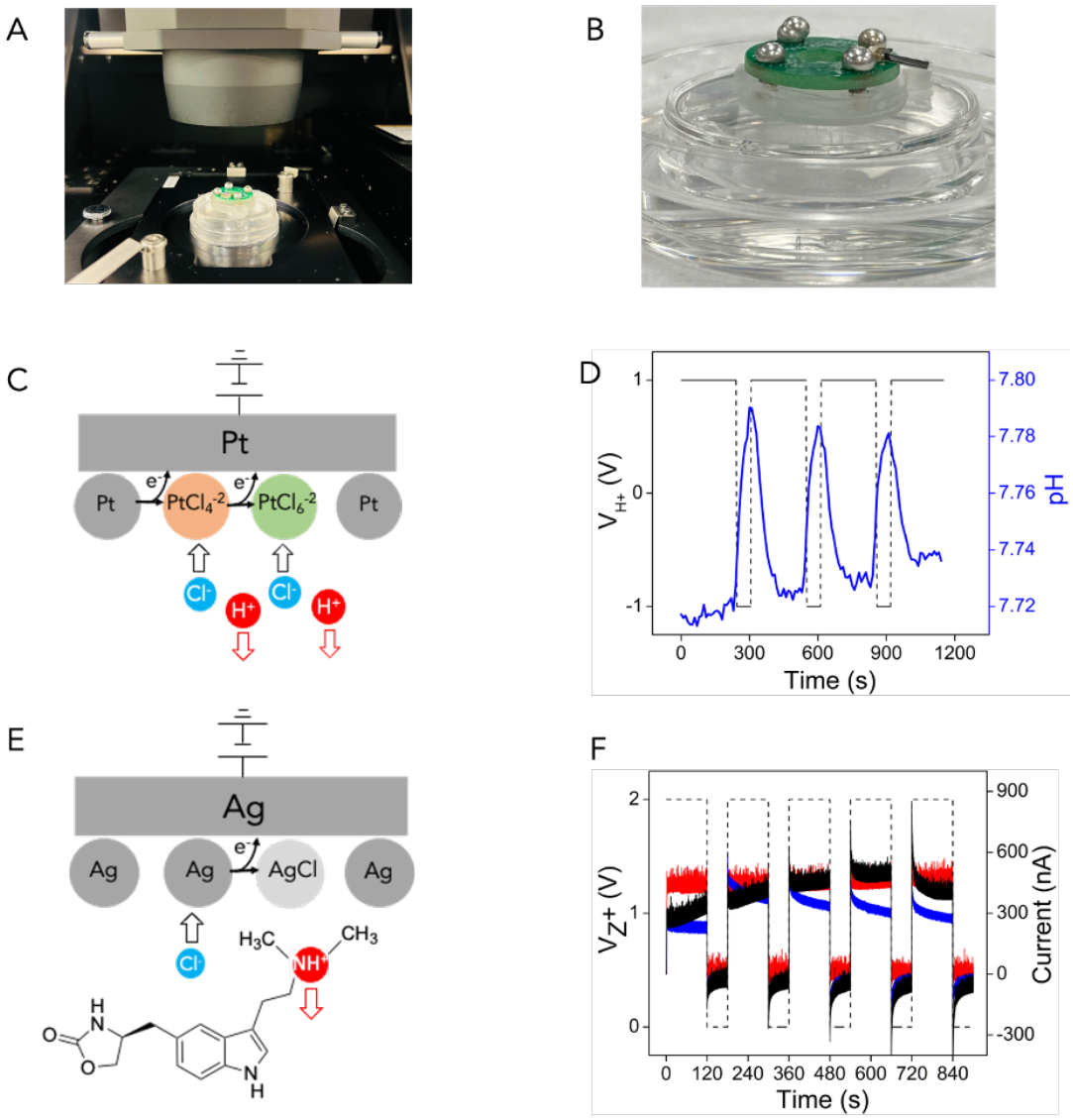


Figure 23: *(A) Microscopy set up for the calibration and proton delivery testing of the bioelecronic device. (B) Experimental set up for the calibration and zolmitriptan delivery testing of the bioelectronic device. (C) The oxidation reaction that occurs at the WE in HCl solution when Pt is the electrode material. (D) Fluorescence response*

of the device for H^+ delivery. (E) The oxidation reaction that occurs at the WE in Zolmitriptan-HCl solution when Ag is the electrode material. (F) Current response of the device to a series of V_{Z+} pulses.

For H^+ delivery, we used platinum (Pt) as the WE (Figure 23C). By using Pt as the WE, chloride ions present in the acidic solution undergo an initial reaction with Pt, resulting in the formation of $PtCl_4^{2-}$ [167,168]. This newly formed $PtCl_4^{2-}$ species can subsequently undergo further reactions with additional chloride ions in the solution, leading to the formation of $PtCl_6^{2-}$ [167,168]. Based on the standard redox potentials, the energy required for the formation of $PtCl_4^{2-}$ and $PtCl_6^{2-}$ is lower compared to the energy needed for the process of water splitting[169]. This indicates that the formation of $PtCl_4^{2-}$ and $PtCl_6^{2-}$ are favored and occur prior to any water splitting reactions taking place[168,169]. Furthermore, with the consumption of each chloride ion, one proton is pushed through the IEM[168]. For detecting $[H^+]$, the target solution comprised tris buffer and 5-(and-6)-Carboxy SNARF™ -1, a pH indicator dye with emissive wavelengths at 580 nm and 640 nm. Ratiometric calibration of the fluorescence response at both wavelengths, using solutions of known $[H^+]$, facilitated pH determination. Employing a device containing 0.5 M HCl in the reservoirs, we alternated V_{H+} pulses (+1 and -1 V), with positive pulses lasting 4 minutes and negative pulses lasting 1 minute. The positive V_{H+} pulses transferred H^+ from the device reservoir to the target solution, resulting in fluorescence intensity changes at both emissive wavelengths (Figure 24) and a corresponding pH change near the capillary at the WE (Figure 23D). With each positive V_{H+} pulse, the pH decreased by approximately 0.03 to 0.05 units. Considering the buffering capacity

of the target solution, we determined that the average per-pulse delivery efficiency[153] for three positive pulses was 41.2%.

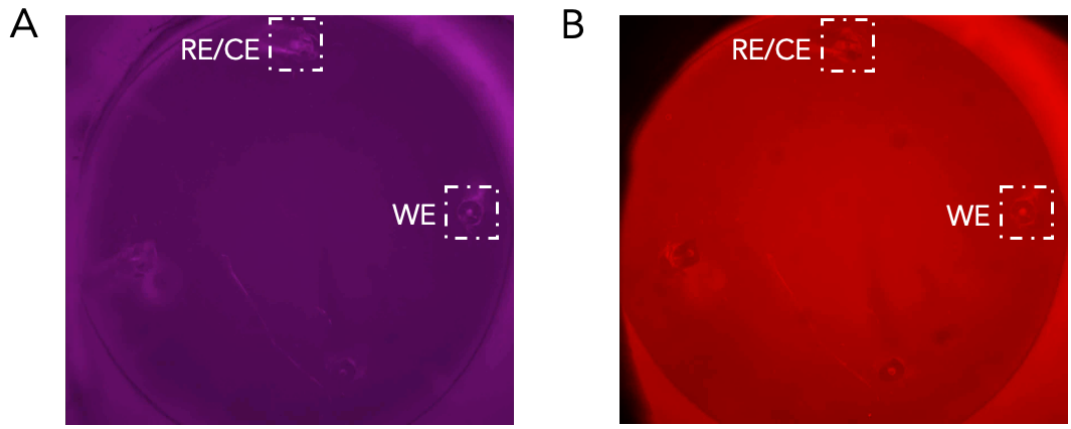


Figure 24: Fluorescence microscopy images of the outlets of a proton delivery device at the (A) 540 nm emission wavelength and (B) the 640 nm emission wavelength. The target contains tris buffer and SNARF dye. Fluorescence responses were recorded from the local area at the outlet near the WE.

To demonstrate the potential of the bioelectronic device for biomolecule delivery, we performed similar tests using the selective serotonin receptor agonist zolmitriptan. Zolmitriptan was dissolved in 100 mM HCl solutions at 1:1 molar ratio to form protonated zolmitriptan$^+$ (Z^+). For Zolmitriptan$^+$ delivery, we used Ag as the WE (Figure 23E). With a positive V_{Z+} pulse, Cl^- undergoes oxidation to become Cl, resulting in the formation of AgCl on the Ag surface. Simultaneously, Z^+ electrophoretically transfers through the IEM towards the target solution. With V_{Z+} pulses (+2 and 0 V),we recorded the current response of three devices (Figure 23F). To

determine the delivery efficiency, we conducted calibration using solutions with varying concentrations of Z^+ and analyzed the target solutions using High-Performance Liquid Chromatography (HPLC). The HPLC analysis revealed an average delivery efficiency of 55.2% for three delivery trials.

We assessed the bioelectronic device ability to deliver ions and biomolecules in a mouse model. For each in vivo study, we used three mice. Each mouse had two circular 6 mm splinted excisional wounds (Figure 25).



Figure 25: Example image of a mouse wound created for the in vivo experiments right after wound creation with splint ring.

Since wound contraction is a significant aspect of wound healing in mice but not in humans, we employed a silicone splint ring to minimize its impact during the study[170]. Then, we positioned the bioelectronic device onto the silicone splint ring (Figure 26A).

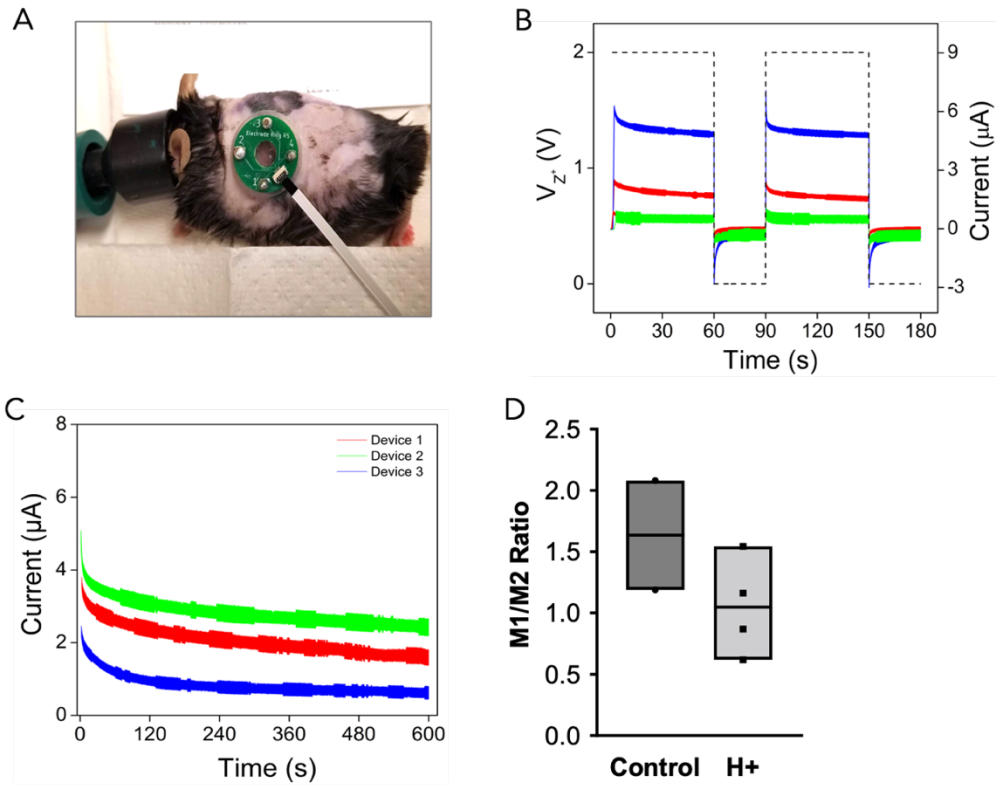


Figure 26: (A) Setup of the bioelectronic device on a mouse wound. The current profiles obtained from the actuation of the respective devices on anesthetized mouse wounds for (B) Zolmitriptan+, and (C) H+ delivery. (D) Quantification of M1/M2 macrophage ratios from H^+ delivery experiments (p=0.22). Dots in the floating bars indicate data from each mouse with lines showing the mean values.

The initial phase of our in vivo investigation focused on delivering Zolmitriptan. Zolmitriptan exhibits significant potential for wound healing by reducing both pain and inflammation[171]. In addition, its activation of the serotonin receptors can improve healing via serotonin-mediated pathways that impact on keratinocyte migration and wound inflammation[163]. Previous studies have demonstrated that directly administering

zolmitriptan to the human skin alleviates pain, reduces inflammation, and promotes the formation of new blood vessels[161]. To demonstrate the in vivo capability of our device to also deliver large biomolecules, we monitored the device's current response to a 2V peak-to-peak rectangular wave while on a mouse wound. The waveform consisted of 120 seconds at 2V and 60 seconds at 0V (Figure 26B). Based on the efficiency determined from our previous characterization, the estimated concentration of zolmitriptan delivered to the wound surface was 1.52 mM when considering a local wound fluid volume of 1 μL. These experimental findings validate the successful delivery of Z^+ to a mouse wound using our bioelectronic device.

H^+ ions hold potential implications for wound healing via modulation of both innervation and macrophage recruitment[172,173]. Using the established mouse model, we conducted a control experiment and an actuated device testing experiment. The control testing involved plain PDMS device bodies with capillaries (without PCBs) and unfilled reservoirs, while the actuated device testing involved devices with attached PCBs and reservoirs filled with 0.5 M HCl. We recorded the current profiles obtained from three different devices during a 10-minute actuation period (Figure 26C). The allowable anesthesia time for the mice imposed a limitation on the duration of actuation. Assuming a one-to-one mole ratio of protons delivered per mole of electrons, we estimated the delivery of 6.5 nanomoles of H^+ per device. This estimation provides valuable insights into the device's capability to deliver H^+ ions, facilitating further analysis and interpretation of its potential effects on wound healing[173] and related biological processes[174].

To investigate the biological effects of our bioelectronic system in vivo, we employed immunohistochemistry (IHC) staining to study the presence and distribution of macrophages in wounded skin samples with 3 days of H^+ treatment. Macrophages play crucial roles in various aspects of wound healing and are among the initial cell types to migrate to the wound site. It is worth noting that macrophages exhibit significant plasticity and can transition between different phenotypes. In vitro studies have demonstrated the transition from the classically activated M1 macrophage (pro-inflammatory phenotype) to the alternatively activated M2 macrophage (anti-inflammatory phenotype) known for promoting tissue repair[175,176]. M1 macrophages secrete cytokines such as IL-1, TNFa, IL-6, IL-12, and matrix metalloproteinases (MMPs), while M2 cells produce arginase, TGFb, CCL18, PGE2, IL-10, and upregulate scavenger receptors such as CD206 and CD163. However, in the *in vivo* environment, macrophage phenotype transition may exist as a continuum rather than a strict dichotomy, influenced by various signals within the microenvironment. Therefore, the function of macrophages undergoes precise regulation and dynamic changes in both temporal and spatial dimensions. In this study, our focus was to assess the relative distribution of the two predominant macrophage phenotypes, M1 and M2, at the wound site three days post-wounding. Data were collected from two control mice and four mice treated with H^+ (Figure 26D). To distinguish M1-like cells, we employed iNOS as a specific marker, while CD206 was used to identify M2-like cells. Additionally, a pan macrophage marker, F4/80, was co-stained to facilitate the overall macrophage visualization and analysis. Representative images illustrate that macrophages of both

phenotypes were observed in the wound bed of all samples (Figure 27). The wounds that received H^+ treatment exhibited a decrease in the quantity of F4/80+iNOS+ M1 macrophages, while the number of F4/80+CD206+ M2-like cells showed minimal change in comparison. Consequently, the ratio of M1 to M2 macrophages decreased noticeably after three days of treatment (Figure 26D). We can attribute the high *p* value of 0.22 to the low sample size in the control group. These results indicate that H^+ stimulation using our bioelectronic bandage can modulate the wound environment, thereby expediting the healing processes. Our findings offer valuable insights into the potential roles of macrophages in response to H^+ treatment and its therapeutic effects.

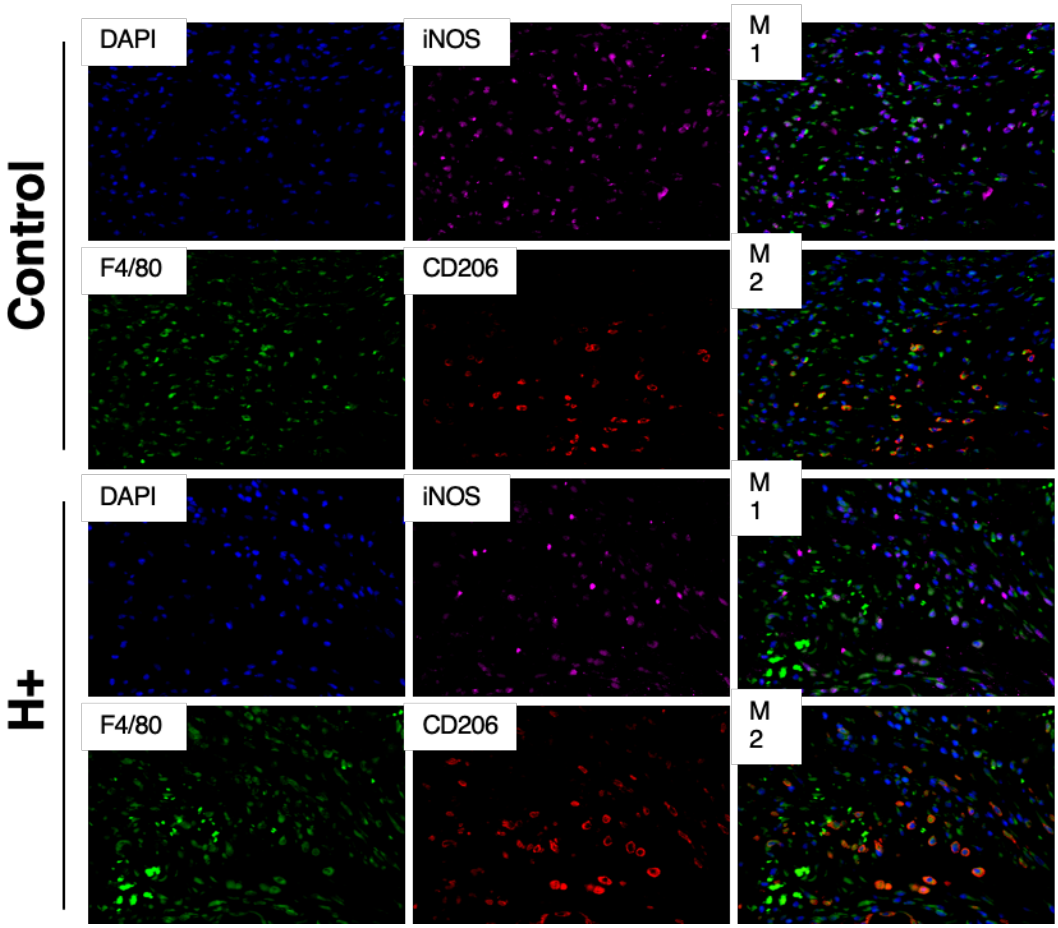


Figure 27: Representative immunofluorescence images of dorsal skin wound tissues from mice 3 days after wounding with/without H+ treatment. Seven μm thick tissue sections were co-stained with F4/80 (green) plus iNOS (purple), CD206 (red), and DAPI (blue) as indicated. n = 2 mice for the control, and n =4 for the H^+ treated group. 5 images were taken for each sample for quantification.

5.2.3 Conclusion

We developed a bioelectronic device for controlled delivery of therapeutic ions and biomolecules towards expediting wound healing. Our advanced, bioelectronic ion pump-based device enables targeted delivery of therapeutic agents to the wound site. The use of electrophoretic ion pumps and ion-selective hydrogels allows for the flow-free delivery of specific ions such as H^+ as well as biomolecules like zolmitriptan. The successful delivery of these substances was validated through in vitro characterization. Further, the in vivo studies conducted in a mouse model demonstrated the device's potential in wound healing, as shown through the decreased M1/M2 macrophage ratio observed with proton delivery.

This bioelectronic device holds promise for addressing the complex physiological changes that occur during wound healing. By delivering therapeutic treatment in a targeted manner, the device has the potential to decrease inflammation and stimulate tissue regeneration, thereby enhancing the healing process. Further optimization and development of this device, including exploring additional ions and biomolecules, could lead to innovative strategies for wound healing and contribute to improved

patient outcomes. The integration of bioelectronics with wound healing processes represents a promising avenue for future research and the development of advanced therapeutic approaches.

5.2.4 Methods

Hydrogel Capillary Fibers Fabrication

We have reported the fabrication process for hydrogel capillary fibers in previous work.[166] The hydrogel precursor solution comprises 2-acrylamido-2-methyl-1-propanesulfonic acid (AMPSA)(1g, 1M), polyethylene glycol diacrylate (PEGDA)(1071.41 μL, 0.4 M), and photoinitiator (I2959) (0.05 g, 0.05 M). We first treat a glass capillary fiber (ID 100 μm, OD 375 μm, 10 cm long) with NaOH etching and silane A174 to promote covalent bonding between the hydrogel and glass fiber interior. After injecting the hydrogel precursor solution into the fiber, UV crosslinking occurs for five minutes at 8 mW/cm^2. We then cut the capillary fibers into 5 mm pieces and store the fibers in solution for several hours before ionic conductivity measurement and device integration.

Ionic Conductivity Measurement

When measuring ionic conductivity of the hydrogel capillaries outside the device, we use PDMS wells to separate two electrolyte solutions, each interfacing with an electrode. One 5 mm hydrogel capillary connects across both solutions. We then use an Autolab potentiostat PGSTAT128N with analytic software Nova 2.0 to supply a

voltage across the electrodes and measure the resultant current. Measurement of device current entails a similar process using the electrodes inside the device.

Fluorescence Probes

For detection of H^+ concentration, we used real-time imaging on a fluorescence microscope (Keyence BZ-X710) with fluorescence probes. We achieved pH detection with the fluorescent probe 5-(and-6)-Carboxy SNARF™-1 (C1270, Invitrogen™), which exhibits a $\lambda_{excitation}$ between 488 and 530 nm and a dual $\lambda_{emission}$ at 580 nm and 640 nm. The ratio of the fluorescence intensities at both wavelength factors into pH determination. The concentration of SNARF in the target was 50 μM in 0.1 M tris buffer. All fluorescence images were analyzed using ImageJ.

M1/M2 Immunohistochemical (IHC) Staining

At the conclusion of each experiment, mice were euthanized, and their wounds were excised. Wound tissues were fixed in a 4% paraformaldehyde solution for 24 hours. Subsequently, the fixed tissues underwent processing in a Tissue-Tek VIP 6 processor (Sakura Finetek, Torrance, CA) and were embedded in paraffin wax blocks. To facilitate analysis, the tissues were then sectioned into 5-μm thick slices and mounted onto glass slides. For macrophage identification, wound tissue slices underwent antigen retrieval treatment and were subsequently blocked for 2 hours using 10% Donkey Serum (Thermo Fisher). Following that, the samples were incubated overnight with primary antibodies targeting specific markers: F4/80 (dilution 1:50; MCA497G, BIO-RAD, Hercules, CA), iNOS (dilution 1:200; PA3-030A, Thermo Fisher Scientific), and CD206 (dilution 1:200; PA5-46994, Thermo Fisher Scientific). Alexa Fluor-

conjugated secondary antibodies (Donkey Anti rat-AlexaFluor 488, Donkey Anti rabbit-AlexaFluor 647, Donkey Anti goat-AlexaFluor 568, dilution 1:200, Thermo Fisher Scientific) were used for subsequent staining, followed by counterstaining with DAPI. To preserve the samples, an anti-fade mountant (SlowFade Mountant; S36936, Thermo Fisher Scientific) was applied, and imaging was performed using a high-resolution microscope (BZ-X800, KEYENCE, Itasca, IL). For each sample, five randomly selected fields at the wound center were imaged, which was determined by the absence of epidermal structures, which were confirmed by parallel Hematoxylin and Eosin (H&E) staining of consecutive sections. The acquired images were subjected to processing using ImageJ and CellProfiler 4.2 software for semi-quantitative analysis. The numbers of macrophage subtypes were manually counted based on double-positive staining through blind counting for reducing statistical bias.

6. DNA nanopores as artificial membrane channels for bioprotonics

Biological membrane channels mediate information exchange between cells and facilitate molecular recognition. While tuning the shape and function of membrane channels for precision molecular sensing via de-novo routes is complex, an even more significant challenge is interfacing membrane channels with electronic devices for signal readout, which results in low efficiency of information transfer - one of the major

barriers to the continued development of high-performance bioelectronic devices. To this end, we integrate membrane spanning DNA nanopores with bioprotonic contacts to create programmable, modular, and efficient artificial ion-channel interfaces. Here we show that cholesterol modified DNA nanopores spontaneously and with remarkable affinity span the lipid bilayer formed over the planar bio-protonic electrode surface and mediate proton transport across the bilayer. Using the ability to easily modify DNA nanostructures, we illustrate that this bioprotonic device can be programmed for electronic recognition of biomolecular signals such as presence of Streptavidin and the cardiac biomarker B-type natriuretic peptide, without modifying the biomolecules. We anticipate this robust interface will allow facile electronic measurement and quantification of biomolecules in a multiplexed manner.

6.1 Introduction

In biological systems, communication between cells occurs via membrane proteins and ion channels that act as size-selective filters or stimulus-responsive molecular valves to either passively allow or actively control the flow of ions across the cell membrane[177]. Cellular communication often surpasses information processing in electronic devices in efficiency, regulation, and specificity[178,179]. Augmenting electronic devices with biological components can enable one to access, analyze, and respond to intercellular information via data transduction and signal transmission[177,180]. Examples include metal oxide semiconductors integrated with ATPase[181], carbon nanotubes[100,101] and silicon nanowires to sense pH[102], 2D transistors functionalized with gramicidin[78], organic electrochemical devices with membrane channels[182,183], and H^+ selective

bioprotonic devices integrated with gramicidin, alamethicin and light sensitive rhodopsins[107,184]. Synthetic membrane channels can further increase the functionality of these devices with well-defined geometries, durability, robustness, and ease of modification[92,185]. Self-assembled synthetic membrane channels are particularly attractive due to their ease of fabrication[92]. To this end, Watson-Crick pairing based hybridization of single-stranded DNA (ssDNA) can rationally and in a bottom-up manner design self-assembled DNA nano-structures[186] that mimic membrane proteins with sophisticated architectures[187-190] and varied functionalities[191-193]. Here, we merge synthetic self-assembled DNA nanopores based ion-channels with H^+ selective Pd-based electrodes to create a bioprotonic device that records and modulates H^+ currents traversing across the bilayer membrane (Figure 34). Unlike previous studies that used single channel ionic current measurements in membrane spanning nanopores[194,195], our device architecture enables biomolecular recognition as a function of ensemble measurement of the overall conductance change of the membrane that is an average over many ion-channels spread over several nanopore states. Utilizing programmable DNA nanopores, we showcase the versatility of the device in detecting specific biomolecules through distinct electronic signals, eliminating the need for additional pre-processing of the biomolecules.

6.2 Results

6.2.1 DNA Nanopore Bioprotonics

The DNA nanopore bioprotonic device comprises DNA nanopore ion channels spanning a supported lipid bilayer membrane (SLB) that is atop a Palladium (Pd) contact integrated with a microfluidic architecture (Figure 28a and 29).

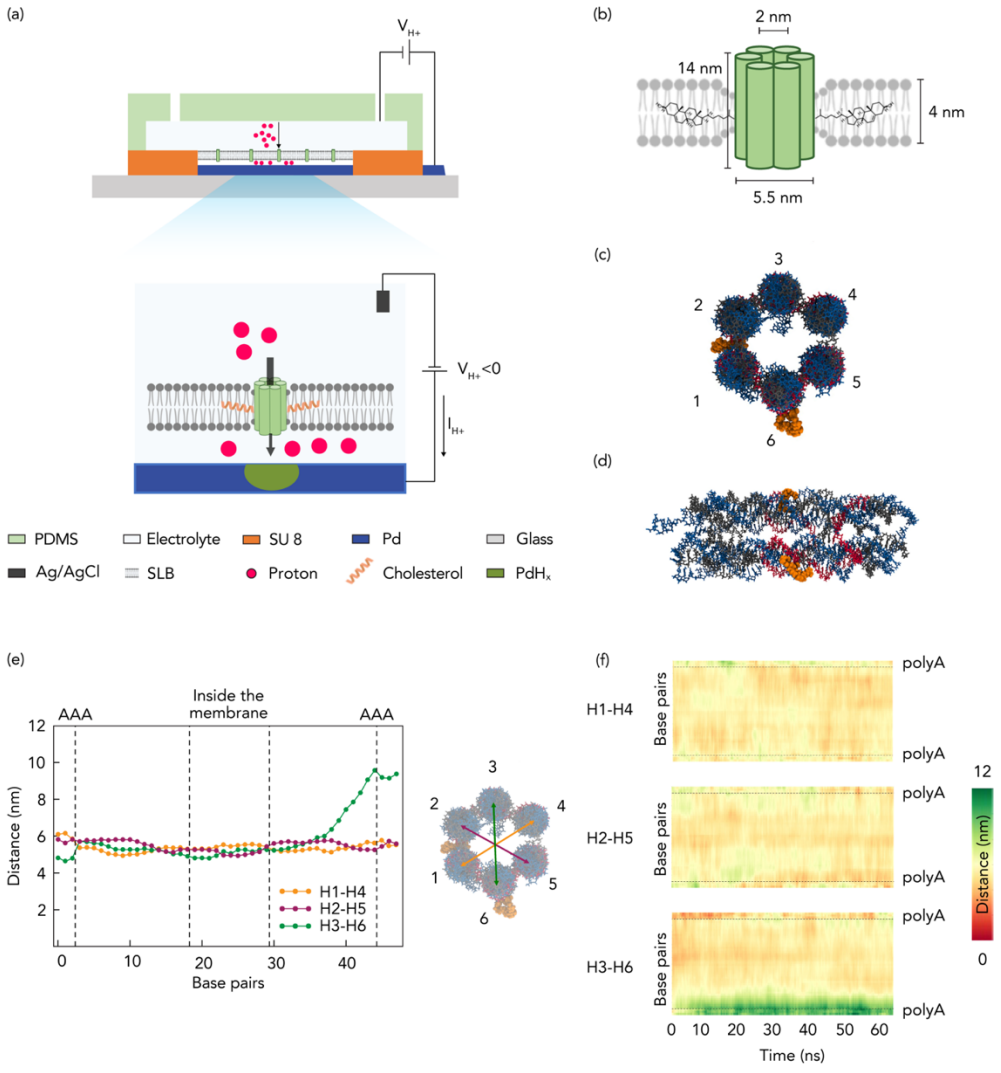


Figure 28: Schematics of bioprotonic devices. (a) Schematic depiction of the bioprotonic device. (b) Schematic representation of a DNA nanopore comprising six-helix bundles and 2-cholesterol anchors. (c) Top view of DNA nanopores with positioned cholesterol anchors. (d) Lateral view of DNA nanopores with positioned base pairs. (e) Simulation of the average distance between the diametrically opposite strands across the length of the nanopore. Yellow for distance between strands 1 and 4, green for distance between strands 2 and 5 and magenta for distance between strands 3 and 6. (f) Average distance heatmap for the pairs indicated in c and e.

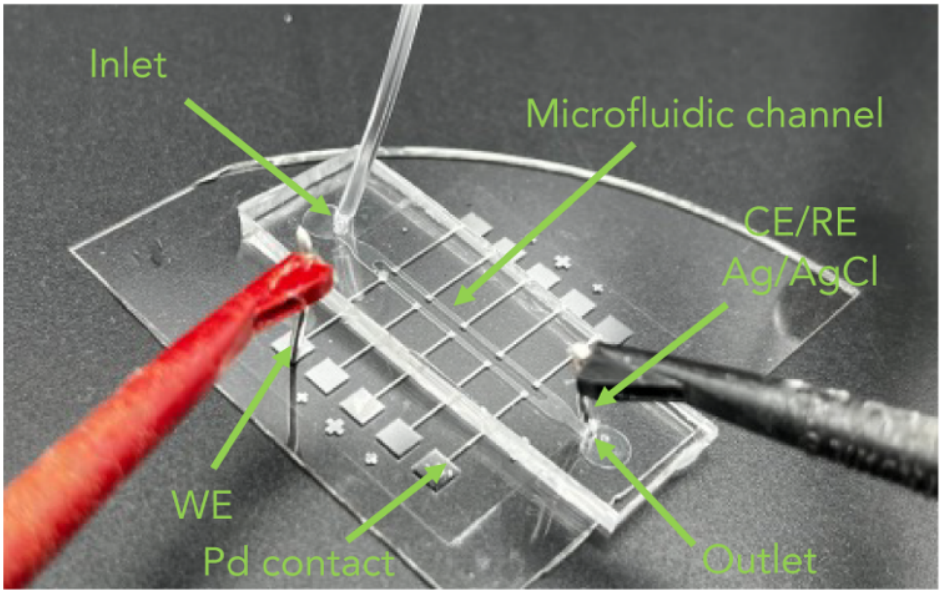


Figure 29: Optical image of the bioprotonic device.

A voltage (V_{H+}) between the Pd contact and the Ag/AgCl reference positioned in the solution causes a current of H^+ between the Pd contact and the solution depending on

polarity[196,197]. As previously reported, this flow of H^+ induces the electrochemical formation or dissolution of PdH_x that results in a measurable current (I_{H+}) in the electronic circuit[107,184,197]. Although this strategy does not afford enough temporal nor spatial resolution to investigate individual ion channel states, we used it to measure the average change in membrane conductance due to ion channel insertion and activity. To create biomimicking ion channels that enable H^+ transfer across the SLBs, we formed 14 nm long barrel shaped DNA nanopores via bottom-up rational design and directed self-assembly (Figure 28b). While simple ion-channels made out of DNA duplexes that lack a central hollow pore have been previously demonstrated as effective membrane spanning ion-conduction pathways[198], we chose a DNA nanostructure geometry consisting of a central physical pore to closely mimic the membrane[199-201] and enable a larger range of signal differentiation upon varied degrees of blockage of the pore. To design the nanostructure, we adapted the single stranded tile assembly method proposed by Seeman and colleagues[202] to self-assemble a nanobarrel-like structure with a hollow lumen from equimolar amounts of 13 short ssDNA strands. To design the strands, we first defined the desired geometry in a hexagonal lattice-based DNA design software caDNAno[203] and filled the shape from top to bottom with an even number of parallel double helices, held together by periodic crossovers of the strands. The sequences were randomly generated and then rationally down selected to maximize primary interactions as designed and minimize secondary and tertiary complex formations. The resulting 13 ssDNA strands (Table 5) were mixed in equimolar amounts to enable one-pot self-assembly into 6 inter-linked Helix Bundles (6HB) that

form the walls of the nanopore (Figure 28b, c, d). We functionalized the DNA nanopore with Tetri-ethylene Glycol–Cholesterol (TEG-Chol) to provide an anchor for insertion of the hydrophilic DNA nanopores into the hydrophobic environment of the SLB (Figure 28b, c, d and Figure 30 and 31). Next, we conducted transmission electron microscopy (Figure 31), dynamic light scattering (DLS) (Figure. 31c and d) analysis as well as molecular dynamics (MD) simulations to investigate the dimensions and the stability of the 6HB inside the SLB and its pore size under dynamic environments (Figure 28e and f). The average distance between the diametrically opposite DNA helices across the length of the nanopore is analyzed, as depicted in Figure 28e, providing insights into the pore size. Additionally, Figure 34f illustrates the dynamic behavior of these distances, as they change with time on a base pair level within the DNA nanopore. Our analysis revealed that inside the membrane, the center-to-center distances of the opposite helices ranged between 5 and 6 nm. Given that the radius of a DNA double helix is 1 nm, this indicated that the average pore size fluctuated between 3 and 4 nm. Outside the membrane, the DNA helices exhibited increased mobility, resulting in some helices moving apart from one another (Figure 28e green plot). However, as seen in the Figure 28f, this phenomenon did not impact the stability of the pore as the TEG-Chol anchors stabilized the DNA nanopore inside the SLB. Therefore, we infer that the length of the nanopore provides sufficient area for decoration with hydrophobic anchors to enable spontaneous insertion while projecting further beyond the SLB to enable desired interactions at the lip of the nanopore without disrupting its stability within the bilayer. The small inner lumen size facilitates proton transport

across the channel while obstructing proteins and other larger biomolecules to remain on the cis (negatively charged) side of the nanopore[199].

Table 5: Sequences of DNA nanopores

Source	Sequence Name	Oligo Sequence
6HB-2C nanopores		
IDT	S1-A	AAATCCACGTTCTTTAATAGTGGACTCTTGTTCCAAACTGGAACAAAA
IDT	S2-A	AAAGGCTATTCTTTTGATTTATAAGGGATTTTGCCGATTTCGGAAAAA
IDT	S3-A	AAAACAGGATTTTCGCCTGCTGGGGCAAACCAGCGTGGACCGCTTAAA
IDT	S4-A	AAACAACTCTCTCAGGGCCAGGCGGTGAAGGGCAATCAGCTGTTGAAA
IDT	S5-A	AAATCTCACTGGTGAAAAGAAAAACCACCCTGGCGCCCAATACGCAAA
IDT	S6-A	AAATCCCCGCGCGTTGGCCGATTCATTAATGCAGCTGGCACGACAAAA
IDT	S7	AGAGTTGGCGTATTGCGGGGA
IDT	S8	TGTCGTGACGTGGATTCCGAAATCGGCAGGCGAAATGATTGCCCTTCAC
IDT	S9	TCCACTATTAAAGACCAGCTGTTTCACCAGTGAGACAACAGCATCCTGT
IDT	S10	AAGCGGTAATAGCCTGTTCCA
IDT	S13	GAATCGGACAAGAGTTATAAATCAAAAGCCACGCTCCCTGAG
IDT	S11-TEGChol	CGCCTGGGGTTTGCCCCAGCAAAATCCC/3CholTEG/
IDT	S12-TEGChol	GTTTGGACCAACGCGGGCGCCAGGGTGGTTTTTCTCATTAAT/3CholTEG/

6HB nanopores		
IDT	S1-A	AAATCCACGTTCTTTAATAGTGGACTCTTGTTCCAAACTGGAACAAAA
IDT	S2-A	AAAGGCTATTCTTTTGATTTATAAGGGATTTTGCCGATTTCGGAAAAA
IDT	S3-A	AAAACAGGATTTTCGCCTGCTGGGGCAAACCAGCGTGGACCGCTTAAA
IDT	S4-A	AAACAACTCTCTCAGGGCCAGGCGGTGAAGGGCAATCAGCTGTTGAAA
IDT	S5-A	AAATCTCACTGGTGAAAAGAAAAACCACCCTGGCGCCCAATACGCAAA
IDT	S6-A	AAATCCCCGCGCGTTGGCCGATTCATTAATGCAGCTGGCACGACAAAA
IDT	S7	AGAGTTGGCGTATTGCGGGGA
IDT	S8	TGTCGTGACGTGGATTCCGAAATCGGCAGGCGAAATGATTGCCCTTCAC
IDT	S9	TCCACTATTAAAGACCAGCTGTTTCACCAGTGAGACAACAGCATCCTGT
IDT	S10	AAGCGGTAATAGCCTGTTCCA
IDT	S11	CGCCTGGGGTTTGCCCCAGCAAAATCCC
IDT	S12	GTTTGGACCAACGCGGGCGCCAGGGTGGTTTTTCTCATTAAT
IDT	S13	GAATCGGACAAGAGTTATAAATCAAAAGCCACGCTCCCTGAG

Fluorescent 6H-2C nanopores		
IDT	S1-A-5'-Atto488	/5ATTO488N/AAATCCACGTTCTTTAATAGTGGACTCTTGTTCCAAACTGGAACAAAA
IDT	S2-A-5'-Atto488	/5ATTO488N/AAAGGCTATTCTTTTGATTTATAAGGGATTTTGCCGATTTCGGAAAAA
IDT	S3-A-5'-Atto488	/5ATTO488N/AAAACAGGATTTTCGCCTGCTGGGGCAAACCAGCGTGGACCGCTTAAA
IDT	S4-A-5'-Atto488	/5ATTO488N/AAACAACTCTCTCAGGGCCAGGCGGTGAAGGGCAATCAGCTGTTGAAA
IDT	S5-A-5'-Atto488	/5ATTO488N/AAATCTCACTGGTGAAAAGAAAAACCACCCTGGCGCCCAATACGCAAA
IDT	S6-A-5'-Atto488	/5ATTO488N/AAATCCCCGCGCGTTGGCCGATTCATTAATGCAGCTGGCACGACAAAA
IDT	S7	AGAGTTGGCGTATTGCGGGGA
IDT	S8	TGTCGTGACGTGGATTCCGAAATCGGCAGGCGAAATGATTGCCCTTCAC
IDT	S9	TCCACTATTAAAGACCAGCTGTTTCACCAGTGAGACAACAGCATCCTGT
IDT	S10	AAGCGGTAATAGCCTGTTCCA
IDT	S13	GAATCGGACAAGAGTTATAAATCAAAAGCCACGCTCCCTGAG
IDT	S11-TEGChol	CGCCTGGGGTTTGCCCCAGCAAAATCCC/3CholTEG/
IDT	S12-TEGChol	GTTTGGACCAACGCGGGCGCCAGGGTGGTTTTTCTCATTAAT/3CholTEG/

6HB-2C-2B nanopores		
IDT	5'Bn-S1-A	/5Biosg/TCCACGTTCTTTAATAGTGGACTCTTGTTCCAAACTGGAACAAAA
IDT	S2-A	AAAGGCTATTCTTTTGATTTATAAGGGATTTTGCCGATTTCGGAAAAA
IDT	S3-A	AAAACAGGATTTTCGCCTGCTGGGGCAAACCAGCGTGGACCGCTTAAA
IDT	5'Bn-S4-A	/5Biosg/CAACTCTCTCAGGGCCAGGCGGTGAAGGGCAATCAGCTGTTGAAA
IDT	S5-A	AAATCTCACTGGTGAAAAGAAAAACCACCCTGGCGCCCAATACGCAAA
IDT	S6-A	AAATCCCCGCGCGTTGGCCGATTCATTAATGCAGCTGGCACGACAAAA
IDT	S7	AGAGTTGGCGTATTGCGGGGA
IDT	S8	TGTCGTGACGTGGATTCCGAAATCGGCAGGCGAAATGATTGCCCTTCAC
IDT	S9	TCCACTATTAAAGACCAGCTGTTTCACCAGTGAGACAACAGCATCCTGT
IDT	S10	AAGCGGTAATAGCCTGTTCCA
IDT	S13	GAATCGGACAAGAGTTATAAATCAAAAGCCACGCTCCCTGAG
IDT	S11-TEGChol	CGCCTGGGGTTTGCCCCAGCAAAATCCC/3CholTEG/
IDT	S12-TEGChol	GTTTGGACCAACGCGGGCGCCAGGGTGGTTTTTCTCATTAAT/3CholTEG/

Fluorescent 6HB-2C-2B nanopores		
IDT	5'Bn-S1-A-Atto488	/5ATTO488N/5Biosg/TCCACGTTCTTTAATAGTGGACTCTTGTTCCAAACTGGAACAAAA
IDT	S2-A-5'-Atto488	/5ATTO488N/AAAGGCTATTCTTTTGATTTATAAGGGATTTTGCCGATTTCGGAAAAA
IDT	S3-A-5'-Atto488	/5ATTO488N/AAAACAGGATTTTCGCCTGCTGGGGCAAACCAGCGTGGACCGCTTAAA
IDT	5'Bn-S4-A-Atto488	/5ATTO488N/5Biosg/CAACTCTCTCAGGGCCAGGCGGTGAAGGGCAATCAGCTGTTGAAA
IDT	S5-A-5'-Atto488	/5ATTO488N/AAATCTCACTGGTGAAAAGAAAAACCACCCTGGCGCCCAATACGCAAA

IDT	S6-A-5'-Atto488	/5ATTO488N/AAATCCCCGCGCGTTGGCCGATTCATTAATGCAGCTGGCACGACAAAA
IDT	S7	AGAGTTGGCGTATTGCGGGGA
IDT	S8	TGTCGTGACGTGGATTCCGAAATCGGCAGGCGAAATGATTGCCCTTCAC
IDT	S9	TCCACTATTAAAGACCAGCTGTTTCACCAGTGAGACAACAGCATCCTGT
IDT	S10	AAGCGGTAATAGCCTGTTCCA
IDT	S13	GAATCGGACAAGAGTTATAAATCAAAAGCCACGCTCCCTGAG
IDT	S11-TEGChol	CGCCTGGGGTTTGCCCCAGCAAAATCCC/3CholTEG/
IDT	S12-TEGChol	GTTTGGACCAACGCGGGCGCCAGGGTGGTTTTTCTCATTAAT/3CholTEG/

	6HB-2C-2AP nanopores	
IDT	5'AP-S1-A	GGCGATTCGTGATCTCTGCTCTCGGTTTCGCGTTCGTTCGTCCACGTTCTTTAATAGTGGACTCTTGTTCCAA ACTGGAACAAAA
IDT	S2-A	AAAGGCTATTCTTTTGATTTATAAGGGATTTTGCCGATTTCGGAAAAA
IDT	S3-A	AAAACAGGATTTTCGCCTGCTGGGGCAAACCAGCGTGGACCGCTTAAA
IDT	5'AP-S4-A	GGCGATTCGTGATCTCTGCTCTCGGTTTCGCGTTCGTTCGCAACTCTCTCAGGGCCAGGCGGTGAAGGGCAA TCAGCTGTTGAAA
IDT	S5-A	AAATCTCACTGGTGAAAAGAAAAACCACCCTGGCGCCCAATACGCAAA
IDT	S6-A	AAATCCCCGCGCGTTGGCCGATTCATTAATGCAGCTGGCACGACAAAA
IDT	S7	AGAGTTGGCGTATTGCGGGGA
IDT	S8	TGTCGTGACGTGGATTCCGAAATCGGCAGGCGAAATGATTGCCCTTCAC
IDT	S9	TCCACTATTAAAGACCAGCTGTTTCACCAGTGAGACAACAGCATCCTGT
IDT	S10	AAGCGGTAATAGCCTGTTCCA
IDT	S13	GAATCGGACAAGAGTTATAAATCAAAAGCCACGCTCCCTGAG
IDT	S11-TEGChol	CGCCTGGGGTTTGCCCCAGCAAAATCCC/3CholTEG/
IDT	S12-TEGChol	GTTTGGACCAACGCGGGCGCCAGGGTGGTTTTTCTCATTAAT/3CholTEG/

Fluorescent 6HB-2C-2AP nanopores		
IDT	5'-AP-S1-A-Atto488	/5ATTO488N/AAAGGCGATTCGTGATCTCTGCTCTCGGTTTCGCGTTCGTTCGTCCACGTTCTTTAATAGTGGA CTCTTGTTCCAAACTGGAACAAAA
IDT	S2-A-5'-Atto488	/5ATTO488N/AAAGGCTATTCTTTTGATTTATAAGGGATTTTGCCGATTTCGGAAAAA
IDT	S3-A-5'-Atto488	/5ATTO488N/AAAACAGGATTTTCGCCTGCTGGGGCAAACCAGCGTGGACCGCTTAAA
IDT	5'-AP-S4-A-Atto488	/5ATTO488N/AAAGGCGATTCGTGATCTCTGCTCTCGGTTTCGCGTTCGTTCGCAACTCTCTCAGGGCCAGGC GGTGAAGGGCAATCAGCTGTTGAAA
IDT	S5-A-5'-Atto488	/5ATTO488N/AAATCTCACTGGTGAAAAGAAAAACCACCCTGGCGCCCAATACGCAAA
IDT	S6-A-5'-Atto488	/5ATTO488N/AAATCCCCGCGCGTTGGCCGATTCATTAATGCAGCTGGCACGACAAAA
IDT	S7	AGAGTTGGCGTATTGCGGGGA
IDT	S8	TGTCGTGACGTGGATTCCGAAATCGGCAGGCGAAATGATTGCCCTTCAC

IDT	S9	TCCACTATTAAAGACCAGCTGTTTCACCAGTGAGACAACAGCATCCTGT
IDT	S10	AAGCGGTAATAGCCTGTTCCA
IDT	S13	GAATCGGACAAGAGTTATAAATCAAAAGCCACGCTCCCTGAG
IDT	S11-TEGChol	CGCCTGGGGTTTGCCCCAGCAAAATCCC/3CholTEG/
IDT	S12-TEGChol	GTTTGGACCAACGCGGGCGCCAGGGTGGTTTTTCTCATTAAT/3CholTEG/

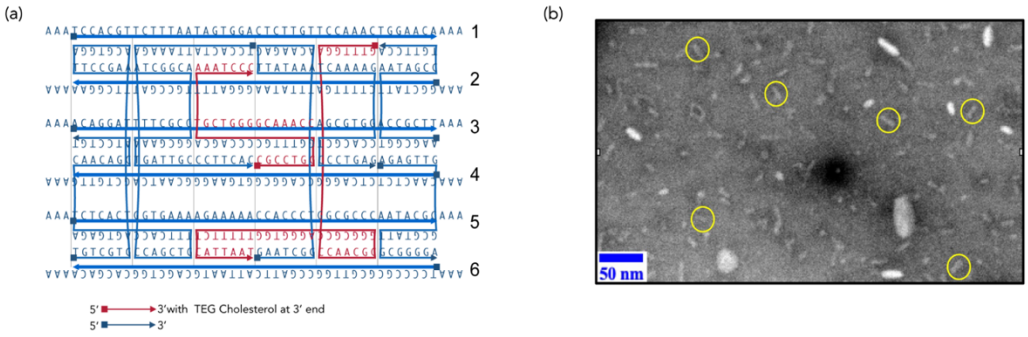


Figure 30: 6HB-2C nanopore design, conformation and simulations. (a) Sequence design and strand crossover details. Red strands indicate those oligos that have been modified at the 3' end with Tri-ethylene Glycol (TEG) cholesterol moieties. Blues strands indicate oligos without any modifications. Squares indicate the 5' end while triangles indicate the 3' end of DNA. (b) Negatively stained TEM micrograph of the 6HB nano-barrels. Yellow circles show the nanopores in a flat orientation.

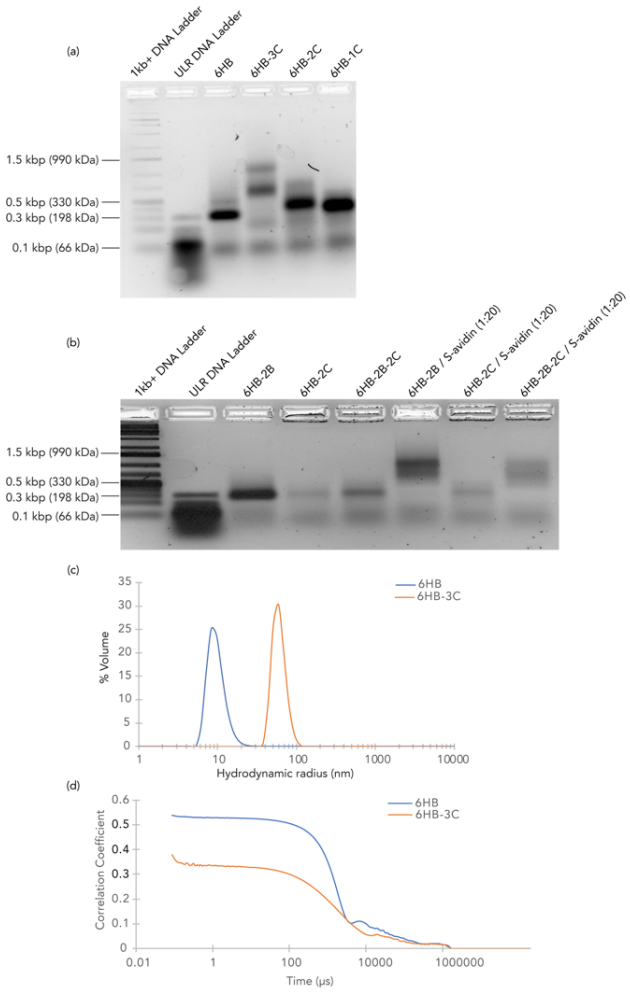


Figure 31: Design and verification of DNA nanopores with cholesterol handles. (a) Electrophoresis characterization (2% Agarose gel) of the nanopores with different number of cholesterol tags around the midsection of the nano-barrel. Lane 1 and 2, DNA ladders; lane 3, fluorescent 6HB nanopores without cholesterol tags; lane 4, 6HB-3C fluorescent nanopores with three cholesterol tags; lane 5, 6HB-2C fluorescent nanopores with two cholesterol tags; lane 6, 6HB-1C fluorescent nanopores with one cholesterol tag. The position of the Kilobase pair length of dsDNA markers is indicated

on the left of the gel. (b) Electrophoresis characterization (2% Agarose gel) of migration patterns of biotin modified nanopores in presence and absence of excess Streptavidin. Lanes 1 and 2, DNA ladders; lane 3, 6HB-2B nanopores without cholesterol modifications; lane 4, 6HB-2C nanopores without biotin modifications; lane 5, 6HB-2B-2C modifications; lane 6, 6HB-2B modifications with excess streptavidin (1x: 20x); lane 7, 6HB-2C modifications with excess streptavidin (1x: 20x); lane 8, 6HB-2C modifications with excess streptavidin (1×: 20×). The position of the base pair length of dsDNA markers are indicated in blue on the migration bands. (c) Dynamic light scattering trace of volume-based size distribution of 6HB nanopores (blue line) without any cholesterol tags and 6HB-3C nanopores (orange line) containing three cholesterol tags as measured on Malvern zetasizer instrument. This experiment was repeated 5 times for each sample and the results shown are the average values. (d) Size correlograms for 6HB and 6HB-3C nanopores showing the raw correlation function versus delay time data in the form of G2(τ) – 1. Both the samples show multiple scattering with intercepts less than 1 owing to that fact that the intensity-based size calculations include large scattering effects from multiple size populations and aggregates present even in extremely low fractions. This experiment was repeated 5 times for each sample and the results shown are the average values.

6.2.2 Control of H^+ flow with DNA Nanopore Bioprotonics

To validate the DNA nanopore ion-channel is indeed a H^+ conductor, we measured the dependence of I_{H+} to V_{H+} in the DNA bioelectronic device (Figure 32a). First, we

verified that the bare Pd contact transfers H^+ at the solution interface (Figure 32a-i). To do so, we recorded I_{H+} as a function of V_{H+} with the following sequence as previously reported[197]. In the first step, V_{H+}= - 400 mV for 600 seconds induces H^+ to flow from the solution into the Pd contact to form PdH_x (Figure 32a -i) as indicated by I_{H+}= -125 ± 11 nA (Figure 32b). In the second step, V_{H+} = 0 mV transferred H^+ from the PdH_x contact into the solution[197]. Here, I_{H+} indicates the prior formation of PdH_x that allows H^+ to transfer from the surface back into the solution even at V_{H+}= 0 mV because at a neutral pH, the protochemical potential of H^+ in the PdH_x contact is higher than the protochemical potential of H^+ in the solution[204]. We confirmed the characteristics of the Pd contact with Electrochemical Impedance Spectroscopy (EIS) (Figure 33 and Table 6).

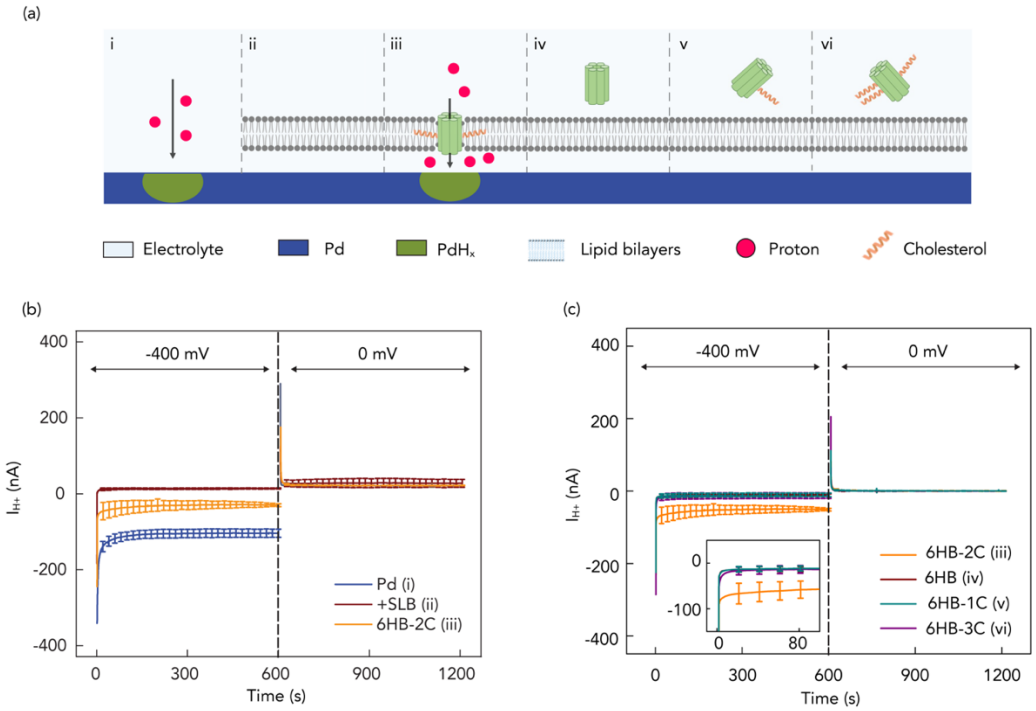


Figure 32: Schematics of control of H+ by membrane spanning DNA nanopores. (a) i) Pd contact with electrolyte solution; ii) Pd contact coated with SLBs; iii) DNA nanopores with 2-cholesterol anchors (6HB-2C); iv) DNA nanopores without cholesterol anchor (6HB); v) DNA nanopores with 1-cholesterol anchor (6HB-1C); vi) DNA nanopores with 3-cholesterol anchor (6HB-3C). (b) IH+ versus time plot for V = -400 mV and V = 0 mV. Blue trace Pd, red trace SLB, Orange trace 6HB-2C. At V = -400 mV, the I_{H+} = -125 ± 11 nA with bare Pd decreased to - 7 ± 1 nA with SLBs that indicates formed bilayers inhibit H+ transfer from the bulk solution to the Pd/solution interface. The I_{H+} = -52 ± 4 nA with 6HB-2C confirmed that the nanopore channels support the H+ transport. Error bars are 1 s.d. (n = 3). (c) I_{H+} versus time plot in different situations of Fig.2a under V = -400 mV and V = 0 mV. Orange trace 6HB-2C (2a-iii), red trace 6HB (2a-iv), cyan trace 6HB-1C (2a-v), and purple trace 6HB-3C (2a-vi). Under -400 mV, we also measured I_{H+} = -11 ± 5 nA, -13 ± 7 nA, and -12 ± 4 nA with 6HB, 6HB-1C and 6HB-3C, respectively. Error bars are 1 s.d. (n = 3). Only 6HB-2C provides created pathway to facilitate the flow of H+ to the Pd/solution interface. For all measurements, we switched the voltage to 0 mV, roughly after 600 s from the first instance of measurement, the H absorbed in Pd is oxidized to H+ and released back into the solution, allowing the current measured to return to 0 nA.

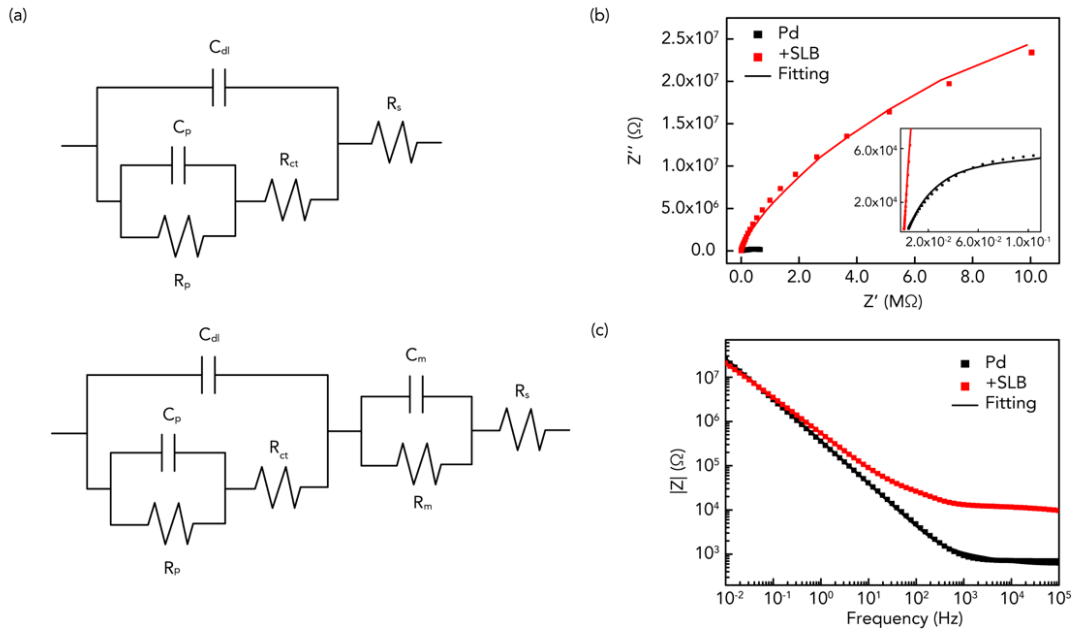


Figure 33: EIS measurement of bioprotonic device and lipid bilayer. (a) Equivalent circuit schematic utilized to fit experimental data. (Top) Bioprotonic device, (Bottom) Bioprotonic device with SLB. The electrolyte solution resistance, Rs, in series with membrane capacitance, Cm, membrane resistance, Rm, double layer capacitance, Cdl, charge transfer resistance, Rct, adsorption resistance Rp, and adsorption capacitance. The fitting to the experimental data was performed using the ZSimpWin software, and the results are provided in Table 6. (b) Nyquist plot illustrating the relationship between the real and imaginary part of the impedance for both bioprotonic devices and lipid bilayers. (c) Bode plot depicting the magnitude and phase of impedance as a function of frequency (Black: Pd and Red: SLB).

Table 6: Fitted parameter for equivalent circuit model of the bioprotonic device and lipid bilayer

	R_s (Ω)	C_m (F)	R_m (Ω)	CPE_{dl} (F)	R_{ct} (Ω)	CPE_p (F)	R_p (Ω)
Bare Pd	753.9	-	-	8.082e-8	2.09e5	1.328e-7	4.551e7
Pd/SLB	753.4	6.959e-6	3.953e-6	1.15e-7	4.784e4	8.919e-7	1.097e6

The overall impedance of lipid bilayer with bioprotonic device was found to be higher than that of the bare device, as evidenced by the larger semicircle in the Nyquist plot. However, in the table, the charge transfer resistance (R_{ct}) values were similar between the two systems. This discrepancy can be attributed to the presence of a gap between the lipid bilayer and the device surface. It may result in an additional resistance component, the membrane resistance (R_m), which contributes to the overall impedance of the lipid bilayer with bioprotonic devices. In addition, the Rm value obtained in this study is similar to the reported in the reference paper, suggesting that the lipid bilayer does not significantly impede the charge transfer process of the device surface but introduces an additional resistive element.

Second, we confirmed that the SLBs create barriers and block H^+ transport from the solution into the Pd surface to make sure that when we insert the DNA nanopore we measured H^+ transport across the nanopore (Figure 32a-ii), as indicated by I_{H+}= -7 ± 1 nA (Figure 32b). To verify the formation of SLBs, we repeated the current measurements and reported the current which are shown as the I_{H+} of 0 nM DNA in (see below) and obtained fluorescence imaging of fluorescence recovery after photobleaching measurements (FRAP) (Figure 34). The measured current, referred to

as the leakage current, indicates that few H^+ diffuse and leak across the bilayer membrane, possibly through the surface defects and are reduced at the Pd surface. After addition of 15 nM DNA nanopores modified with 2 cholesterol handles (6HB-2C) to the solution, we expected that the DNA nanopores spontaneously insert into the lipid bilayer (Figure 32a-iii) to form membrane spanning ion channels. This insertion resulted in I_{H+}= -52 ± 4 nA for V_{H+} = -400 mV (Figure 32b), which is much larger than I_{H+} for the SLBs coated Pd indicating that the DNA nanopores provide a pathway for H^+ to move across the SLBs. For all measurements, to avoid the accumulation of protons on Pd contact, in the second sequence, we set the V_{H+} to 0 mV. The higher photochemical potential than the electrolyte leads to the release of protons into the electrolyte and with positive I_{H+}. As predicted, DNA nanopores without any cholesterol handles (Figure 32a-iv) did not insert into the SLBs as corroborated by the same observed I_{H+} as recorded for the naked SLBs (Figure 32c). Nanopores with one or three cholesterol handles (6HB-1C, 6HB-3C) (Figure 32a-v, vi) also did not insert into the SLBs (Figure 32c). It is likely that 6HB-1C did not insert into the SLBs because one cholesterol handle is not enough to drive the hydrophilic DNA nanopore into the hydrophobic SLBs in a membrane-spanning configuration[205]. However, with the same reasoning one would we expected to see even better insertion for 6HB-3C compared to 6HB-2C. It is likely that the increased hydrophobicity of 6HB-3C drove its aggregation in solution to minimize its interaction with water and made the hydrophobic handles unavailable for insertion into the SLB. This aggregation is confirmed by multiple bands

observed for 6HB-3C in gel electrophoresis (Figure 31a) and a hydrodynamic radius eight times larger for 6HB-3C compared to 6HB as measured by DLS (Figure 31c).

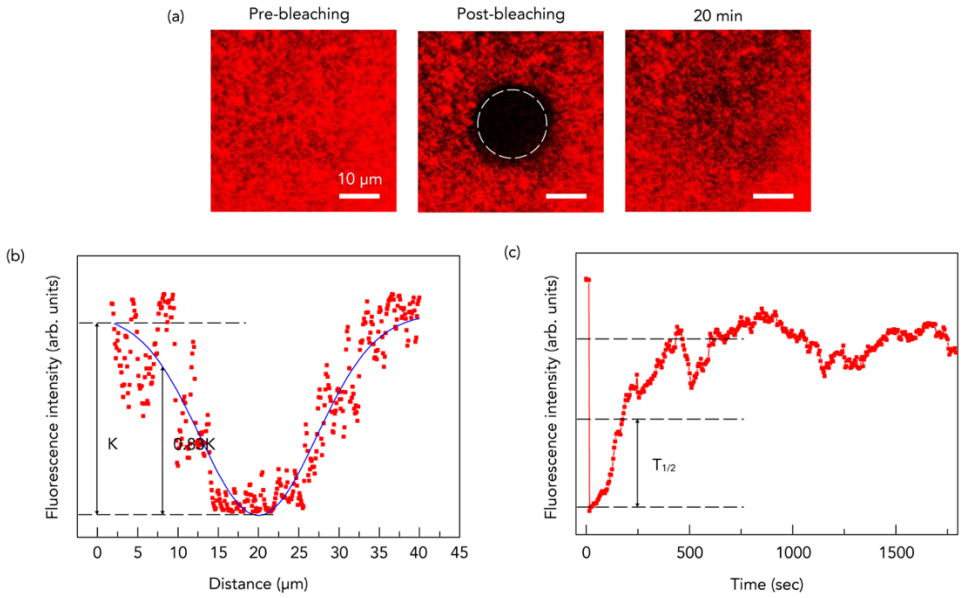


Figure 34: Characterization of lipid bilayer formation on Pd by FRAP. (a) Fluorescence intensity recovery after photobleaching is shown at t = pre, 0, and 20 min (from left to right) (b) Determination of effective bleaching spot. The Gaussian amplitude function was used to extract the effective bleaching spot radius. (c) The normalized fluorescence intensity of FRAP recovery curve. This experiment was independently repeated three times, and the results shown here are representative.

6.2.3 Programming the DNA nanopores for biomolecular sensing

DNA self-assembly allows for programming a desired functionality in the DNA nanopores by designing ad-hoc DNA sequences. As proof-of-concept biomolecular sensing, we programmed DNA nanopores for the detection of two proteins Streptavidin

(S-avidin) and a cardiac biomarker B-type natriuretic peptide (BNP) by including a biotin handle[206] or a DNA aptamer (AP) that has been down selected using the in-vitro SELEX technology respectively on the nanopores. We did so by functionalizing 6HB-2C nanopores using two ssDNAs modified with either a Biotin handle or the AP handle at their 5' ends followed by DNA hybridization to obtain the formation of 6HB-2C-2B (Figure 35a) and 6HB-2C-2AP (see below) nanopores respectively containing the specific tags at either end of the nano barrel. To get a clear current comparison before and after the addition of S-avidin or BNP, we increased the concentration of 6HB-2C-2B and 6HB-2C-2AP to 30 nM for the current measurements. As expected, 6HB-2C-2B nanopores inserted themselves into the SLB and resulted in a large ensemble current I_{H+}= -96 ± 21 nA at V_{H+}= -400 mV, indicating that the nanobarrel inside the DNA nanopore aids H^+ transport across the SLB (Figure 35a-i and b). However, when S-avidin was introduced into the environment in 5 times excess concentration with respect to the nanopore concentration, the binding event of the 5 nm sized S-avidin with the biotin handle[207] on the DNA nanopore effectively occluded the nanobarrel impeding H^+ transport across the SLB as indicated by a reduction of I_{H+} = -12 ± 6 nA (Figure 35a-ii and b) to the level of SLB leakage I_{H+}. This is an interesting result because prior research has shown that DNA structures without interior pores create H^+ conduction pathways across the SLB[198]. To confirm that S-avidin is indeed blocking the pore rather than plugging conduction pathways around the DNA structure, we exposed non-biotinylated 6HB-2C to the same S-avidin concentration (6HB-2C/S-avidin) in solution and did not observe appreciable change in I_{H+} = -92 ± 9 nA (Figure

35a-iii and b) because the S-avidin has no binding site available on the DNA nanopore that would result in the occlusion of the nanobarrel. Our observation and the results from ref. 37 are not necessarily contradictory because the two DNA structures are different from each other, ours contain cholesterol handles, and may interact in a different manner with the SLB. To further confirm that the current drop was indeed caused by the binding between S-avidin and biotin handle of the nanopore leading to the pathway occlusion, we also performed fluorescence imaging experiments prior to and after the addition of the proteins. To fabricate fluorescent nanopores, we modified some of the ssDNA strands with Atto 488 tags on their 5' ends (Table 5) prior to the single pot hybridization of the nanostructures. The fluorescent images of DNA nanopores before and after the addition of S-avidin (Figure 36) show the same number of DNA nanopores spanning the SLBs, exhibiting that binding between S-avidin and biotin indeed blocked the channels and resulted in the decreased ensemble current rather than other possible phenomenon such as nanopore aggregation or bulk dissociation of DNA nanopores from the SLB membrane. Additionally, we measured the dependence of the I_{H+} on the relative concentration of S-avidin with respect to the concentration of the biotin tagged nanopores. With the increase of S-avidin's concentration, more nanopores interacted with S-avidin leading to more blocked channels and thus a higher current decrease (Figure 37).

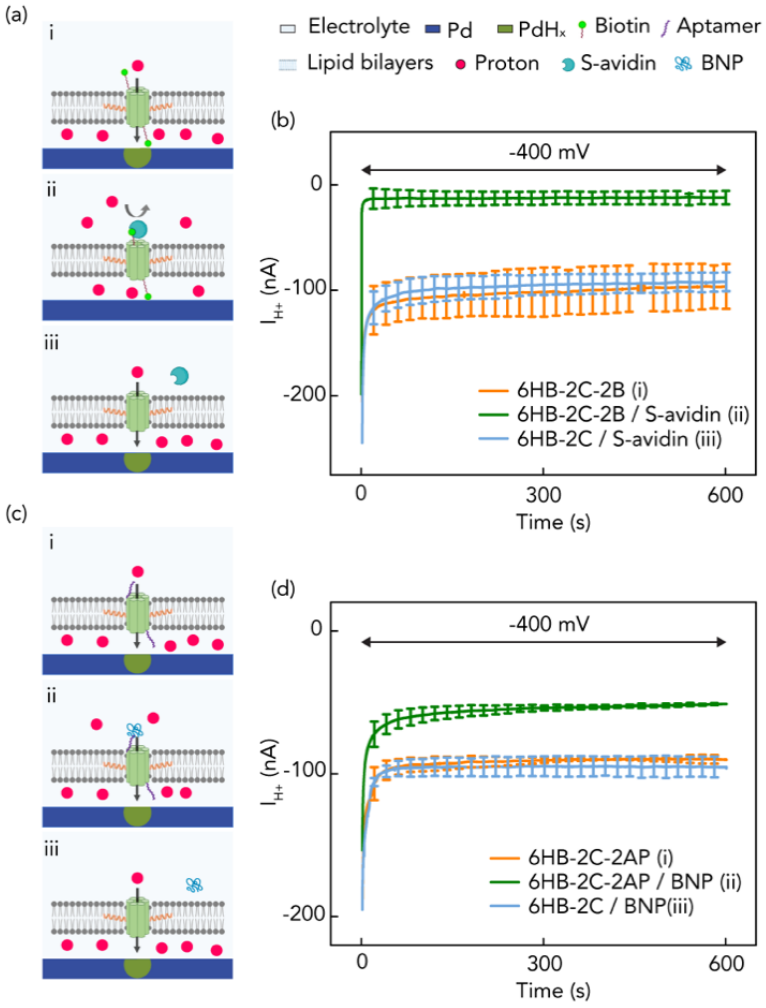


Figure 35: Schematics of bioprotonic devices with biotin-Streptavidin and aptamer-peptide. (a) i) 2-cholesterol handled DNA nanopores with biotin in the absence of streptavidin (6HB-2C-2B). Created pathway facilitates H^+ transfer without inhibition of binding due to absence of streptavidin; ii) 2-cholesterol-handled DNA nanopores with binding of biotin-streptavidin (6HB-2C-2B/S-avidin). H^+ transfer is inhibited by blocked pore channels; iii) 2-cholesterol-handled DNA nanopores without biotin in the presence of streptavidin (6HB-2C/S-avidin). The pores are not blocked by binding due to lacking biotin. (b) I_{H+} versus time plot for V = -400 mV. Orange trace 6HB-2C-2B

(3a-i), green trace 6HB-2C-2B/S-avidin (3a-ii) and blue trace 6HB-2C/S-avidin (3a-iii). We measured I_{H+} = -96 ± 21 nA, -12 ± 6 nA and -92 ± 9 nA with 6HB-2C-2B, 6HB-2C-2B/S-avidin and 6HB-2C/S-avidin, respectively. Error bars are 1 s.d. (n = 3). (c) i) 2-cholesterol handled DNA nanopores with SELEX based DNA aptamer in the absence of B-type natriuretic peptide (6HB-2C-2AP). Created pathway facilitates H+ transfer without inhibition of binding due to absence of peptide; ii) 2-cholesterol-handled DNA nanopores with binding of aptamer-peptide (6HB-2C-2AP/BNP). H^+ transfer is slightly inhibited by blocked pore channels; iii) 2-cholesterol-handled DNA nanopores without aptamer in the presence of peptide (6HB-2C/BNP). (d) IH+ versus time plot for V = -400 mV. Orange trace 6HB-2C-2AP (3c-i), green trace 6HB-2C-2AP/BNP (3c-ii) and blue trace 6HB-2C/BNP (3c-iii). We measured I_{H+} = -90 ± 3 nA, -51 ± 1 nA and -96 ± 9 nA with 6HB-2C-2AP, 6HB-2C-2AP/BNP and 6HB-2C/BNP, respectively. Error bars are 1 s.d. (n = 3).

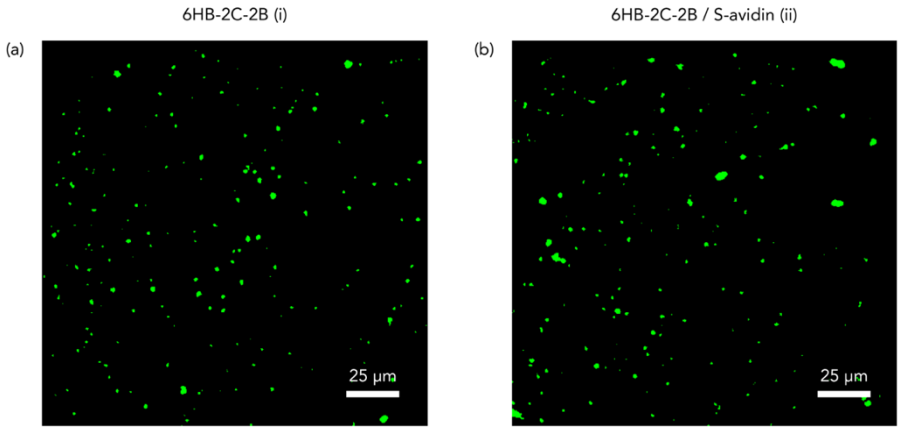


Figure 36: Fluorescence images of 2-cholesterol handled DNA nanopores before and after S-avidin binding. (a) Fluorescence image of DNA nanopores with 2-cholesterol

and biotin in the absence of streptavidin (6HB-2C-2B), showing ~205 nanopores. (b) Fluorescence image of the same nanopores after binding with S-avidin (6HB-2C-2B/S-avidin), showing ~200 nanopores. This experiment was independently repeated five times, and the results shown here are representative.

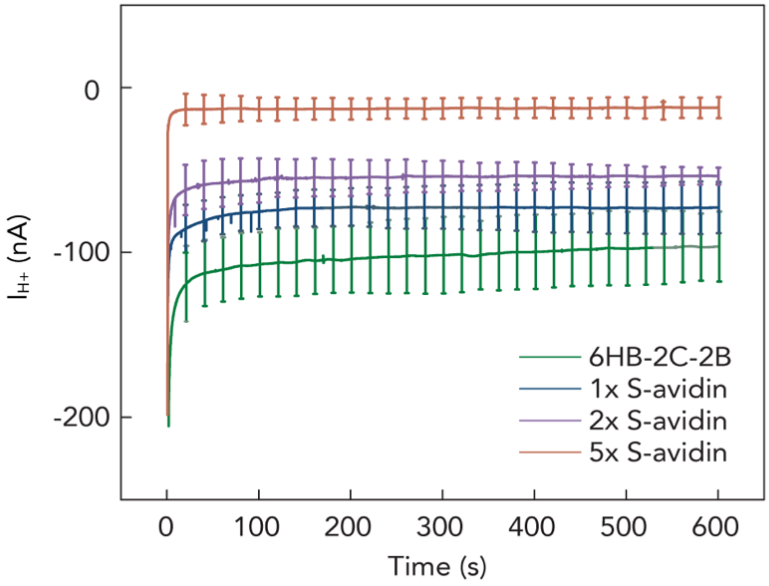


Figure 37: I_{H+} versus time plot for V = -400 mV under different concentrations of S-avidin. Green trace 6HB-2C-2B, blue trace 6HB-2C-2B/1X S-avidin (30 nM), purple trace 6HB-2C-2B/2X S-avidin (60 nM) and red trace 6HB-2C-2B/5X S-avidin (150 nM) which is also the same with the 6HB-2C-2B/S-avidin in Fig. 3b. We measured I_{H+} = -96 ± 21 nA, -73 ± 16 nA, -54 ± 5 nA and -12 ± 6 nA with DNA_Biotin (6HB-2C-2B), 6HB-2C-2B/1X S-avidin, 6HB-2C-2B/2X S-avidin, and 6HB-2C-2B/5X S-avidin respectively. Error bars are 1 s.d. (n = 3). Obviously, the increase of S-avidin's concentration leads to the decrease of I_{H+}.

Similar experiments and controls were conducted with 6HB-2C-2AP nanopores. For the same concentration of 6HB-2C-2AP (Figure 35c) nanopores as that of 6HB-2C-2B nanopores, the I_{H+} observed at V_{H+}= -400 mV was -90 ± 3 nA (Figure. 35c-i and d). Alike the biotin tagged nanopores, the DNA aptamer tagged nanopores inserted themselves into the SLB to form membrane-spanning ion channels and resulted in H^+ transport across the SLB. When BNP protein was introduced into the environment in 5 times excess concentration with respect to the nanopore concentration, a reduced I_{H+} of -51 ± 1 nA was observed (Figure 35c-ii and d) at V_{H+}= -400 mV. This showed that the affinity interactions between AP-BNP at the lip of the ion-channels blocked the transport of H^+. The smaller reduction in current in the case of AP-BNP compared to the dramatic reduction observed in Biotin-S-avidin is attributed to the weaker interaction affinity (k_D of 12 ± 1.5 nM)[208] compared against strong affinity of biotin-Streptavidin (k_D of 10^{-5} nM)[209]. Similarly, as control, exposing non-aptamer modified 6HB-2C nanopores to the same BNP concentration in solution (6HB-2C/BNP) did not cause any appreciable change in I_{H+} of -96 ± 9 nA (Figure 35c-iii and d) because the BNP has no binding site available on the DNA nanopore that would have resulted in the occlusion of the nanobarrel. By leveraging the programmability offered by the DNA nanostructures, we engineered the nanopores to demonstrate an electronic sensing response to a specific analyte in in-vitro environments without the need for modifying the analyte.

6.2.4 A model for the rate constant of association and dissociation of DNA nanopores self-insertion

To better understand the dynamics of DNA nanopore insertion with the SLB, we created a model based on Langmuir's equation and absorption/desorption kinetics[210,211] to analyze the insertion process of the DNA nanopore in the lipid bilayer. In this model, we describe DNA nanopores in solution (*n*) and lipid bilayer sites where the nanopores can be absorbed (*l*) as being initially separate (Eq. 14 left side). Upon insertion of the DNA nanopore into the lipid bilayer, the DNA nanopore and the lipid bilayer sites are conjoined together and we describe this entity as *nl* (Eq. 14 right side).

$$n + l \overset{k_a, k_d}{\longleftrightarrow} nl \tag{14}$$

The rate constant k_a ($M^{-1}s^{-1}$) describes the absorption reaction of the DNA nanopore into the lipid bilayer and the rate constant k_d (s^{-1}) describes the desorption reaction. From this model, we expect that more DNA nanopores in solution (*n*) correspond to a higher number of DNA nanopores inserted into the lipid bilayer (*nl*) resulting in I_{H+} to increase as a function of DNA nanopore concentration (C_n) (Figure 38a). Given the large number of DNA nanopores compared to the absorption area of the lipid bilayer, we assume C_n to be constant throughout the absorption process. To fully understand the absorption and desorption kinetics, we need to now derive k_a and k_d. To do so, we introduce the differential form of the Langmuir equation:

$$\frac{dC_{nl}}{dt} = k_a C_n C_u - k_d C_{nl} \tag{15}$$

where C_n and C_{nl} are the DNA nanopore concentrations in solution and lipid bilayers, respectively, and C_u represents the unoccupied site concentration in the SLBs. Since C_u is an unknown that we are not able to derive experimentally, we write (15) as:

$$\frac{dC_{nl}}{dt} = k_a C_n (C_{max} - C_{nl}) - k_d C_{nl} \quad (16)$$

Where $C_{max} = C_u + C_{nl}$ and C_{max} is the maximum value of C_{nl}. We derive C_{nl} by counting the number of inserted DNA nanopores ($N = C_{nl} V_l A$, V_l = *the volume of lipids*, A = *Avogadro's number*) as a function of C_n at equilibrium using fluorescent microscopy on fluorescently tagged nanopores (Figure 38b and 39). Unfortunately, we are not able to measure C_{max} using fluorescent microscopy for $C_n > 30$ nM because the inserted DNA nanopores are too close to each other and difficult to count. In Figure 44a, we have shown that I_{H+} increases with increasing C_n for $C_n < 45$ nM and then I_{H+} plateaus even if we increase C_n up to100 nM. We assume that for $C_n > 45$ nM, $C_{nl} = C_{max}$. To calculate C_{max} from I_{H+}, we then model the DNA nanopores as resistors in parallel:

$$\frac{R_m}{N} = \frac{V_{H+}}{I_{H+}} \quad (17)$$

and from equation 17 and the slope of Figure 38c, we calculate $R_m = 1 \times 10^{10}\ \Omega$ and $G_m = 1/R_m = 100$ pS, the resistance and conductivity of each individual nanopore. These values are consistent with the conductivity of artificial and natural membrane channels[212,213]. Using the calculated value of R_m, $N_{max} = 2350$ nanopores per device and $C_{max} = 2$ nM. To conclude the derivation of k_a, we then observe experimentally C_{nl}/dt by recording I_{H+} as a function of time introducing the DNA nanopores in the solution for t=0 (Figure 38d). We can thus assume $C_{nl} = 0$ and Eq 16 simplifies to:

$$k_a = \frac{dC_{nl}}{dt} / (C_n C_{max}) \quad (18)$$

Using $N = C_{nl} V_l A$ and equation 18 we can express dC_{nl}/dt as:

$$\frac{dC_{nl}}{dt} = \left| \frac{dI_{H^+}}{dt} \right| \cdot \frac{R_m}{V_{H^+}} \frac{1}{V_l \times A} \quad (19)$$

Combing equation 18 and 19 we can express k_a as:

$$k_a = \left| \frac{dI_{H^+}}{dt} \right| \cdot \frac{R_m}{V_{H^+}} \frac{1}{C_n N_{max}} \quad (20)$$

From the slope of Figure 38d at $t = 0$, we calculate $k_a = 8.5 \times 10^3\ M^{-1}s^{-1}$.

We then look at time t when the system reaches dynamic equilibrium and $dC_{nl}/dt = 0$ and write:

$$k_a C_n (C_{max} - C_{nl,e}) = k_d C_{nl,e} \quad (21)$$

where $C_{nl,e}$ is the adsorbate concentration in bilayers at equilibrium. We derive $C_{nl,e}$ from I_{H+} and calculate $k_d = 1.9 \times 10^{-4}\ s^{-1}$. We then calculate the apparent dissociation constant to be $k_D = k_d/k_a = 22$ nM. The apparent dissociation constant indicates a high affinity of the 6HB-2C to the SLBs and is higher than the affinity of most protein-ligand interactions (100 μM — 100 nM)[212,214,215].

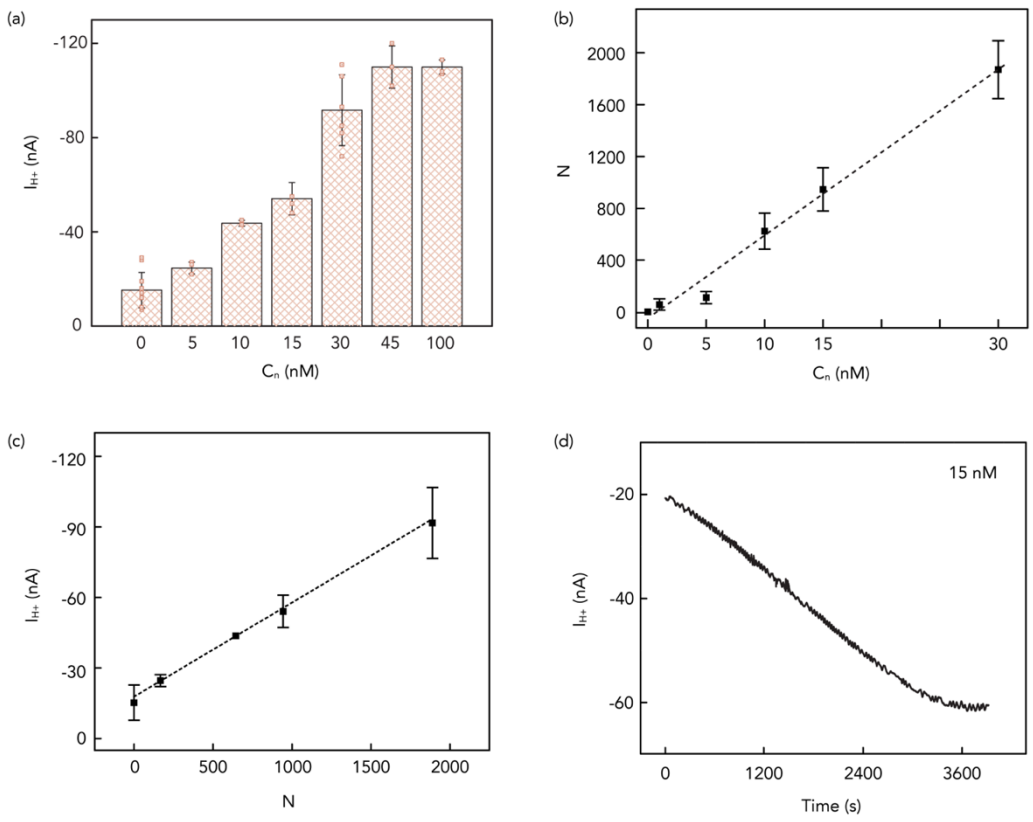


Figure 38: Illustration of DNA nanopores characteristics. (a) I_{H+} versus the introduced 6HB-2C concentration (C_n) plot (V_{H+} = -400 mV) for 6HB-2C nanopores. Inset: Zoom-in view of the data distribution of I_{H+} with different 6HB-2C concentration. We measured I_{H+} = -15 ± 8 nA, -25 ± 3 nA, -44 ± 1 nA, -52 ± 4 nA, -92 ± 15 nA, -111 ± 9 nA and-110 ± 3 nA with 0 nM, 5 nM, 10 nM, 15 nM, 30 nM, 45 nM and 100 nM of 6HB-2C, respectively. Error bars are 1 s.d. (n = 10, 3, 3, 3, 6, 3 and 3 for 0 nM, 5 nM, 10 nM, 15 nM, 30 nM, 45 nM and 100 nM respectively). (b) The number of inserted 6HB-2C nanopores (N) versus the introduced 6HB-2C concentration (C_n) plot. The value of the slope in the plot is 64. Error bars are 1 s.d. (n = 3). (c) I_{H+} versus Number of inserted 6HB-2C nanopores (N) under -400 mV. The value of the slope in the plot is

4×10^{-11}. Error bars are 1 s.d. (n = 3). (d) I_{H+} versus time plot during 15 nM 6HB-2C insertion process under -400 mV.

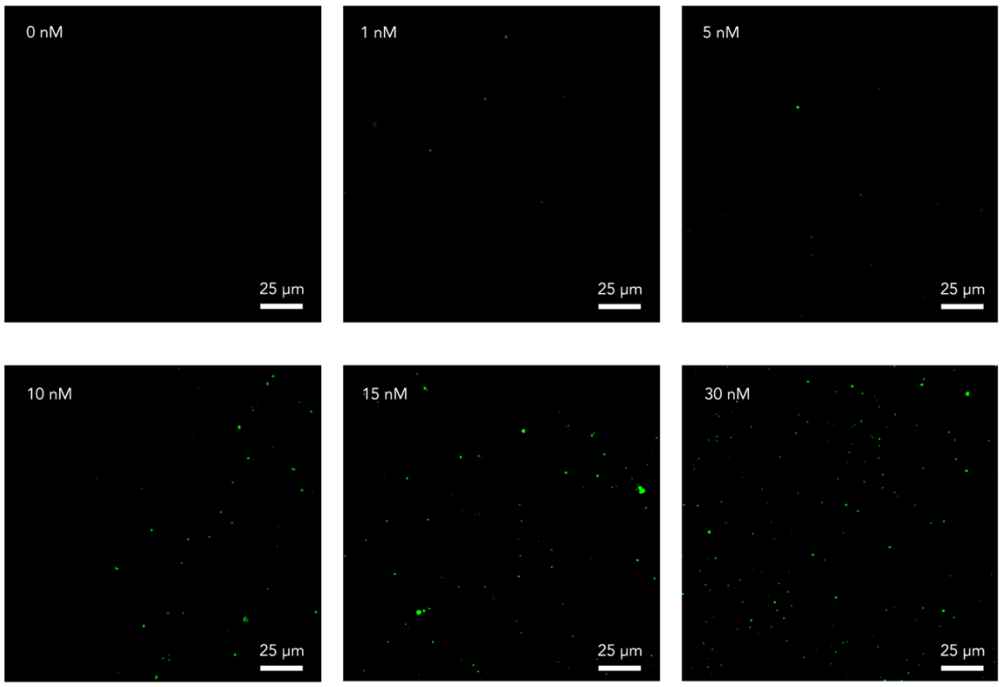


Figure 39: Fluorescence images of DNA nanopores at different concentrations. This experiment was independently repeated five times, and the results shown here are representative.

6.3 Discussion

We have successfully demonstrated a programmable bio-protonic device with membrane-spanning DNA nanopore ion channels as molecularly precise interconnects, which measure and control the H^+ transfer across the lipid bilayer interface. Leveraging

the programmability of DNA constructs to custom design the nanopores and modify their surfaces, we introduced a novel class of self-assembling membrane-spanning molecular signal transducers. These are able to interface with bio-protonic contacts to electronically sense specific biomolecules in-vitro, bypassing the need for additional preprocessing of the biomolecules. With our device architecture, we demonstrated that the ensemble electronic current signals instead of single channel recordings can be effectively used for the electronic recognition of specific biomolecules. This approach enables the simultaneous collection of responses from multiple channels, which could potentially yield more reliable and accurate information about the target. Our ensemble method compensates for any variability or outliers in individual channel recordings, resulting in data that is more consistent and reliable, thereby enhancing the robustness and reliability in sensing the targets. In addition, this strategy greatly simplifies the device fabrication process and the recording of signals by eliminating the necessity for high precision equipment and individual tailoring associated with single-molecule devices. Furthermore, we provided valuable insights into the kinetics of DNA nanopores by conducting ensemble experiments and developing a dynamic model. These findings lay the foundations to explore potential future applications of this DNA nanopore architecture in the field of biosensing.

6.4 Methods

6.4.1 Materials

1,2-dioleoyl-sn-glycerol-3-phosphocholine (DOPC, Avanti Polar Lipids), 1,2-dipalmitoyl-sn-glycerol-3-phosphoethanolamine-N-(lissamine rhodamine B sulfonyl) (Fluorescent liposomes, Avanti Polar Lipids) were used as received for formation of supported lipid bilayers. Unmodified ssDNA oligos in 25 nmole scale with standard purification, 3' TEG-Chol modified ssDNA oligos in 100 nmole scale with HPLC purification, 5'Bn modified ssDNA oligos in 25nmole scale with standard purification, AP-modified ssDNA oligos in 100 nmole scale with PAGE purification and 5'Atto modified ssDNA oligos in 100 nmole scale with HPLC purification were obtained from Integrated DNA Technologies. For sequences, refer to Table 5. The recombinant human BNP protein (ab87200) was purchased from Abcam and Streptavidin was purchased from Thermo Fisher Scientific. TE buffer 10x (pH = 8.0), $MgCl_2 \cdot 6H_2O$, 3-aminopropyl-triethoxy-silane (APTEs) and PBS (pH = 7.5) were purchased from Sigma-Aldrich. The Ag/AgCl reference electrode (RE) and counter electrode (CE) were from Warner Instruments. Glass wafers, 4-in diameter, were obtained from University Wafer Inc.

6.4.2 Device architecture, fabrication and characterization:

Bioprotonic devices were fabricated with conventional soft- and photo-lithography on a 500 μm thick layer of glass. The SU-8 insulating channel is 10 μm thick and the PDMS microfluidic channel is 100 μm on each chip. The Pd contacts, which served as

electrodes for our tests, have a contact area of 0.25 mm^2 (500 x 500 μm) with a thickness of 100 nm for significant interfacing with lipid solution. Pd was deposited on top of 5 nm Cr adhesion layer via electron beam evaporation (EBE). The microfluidic channel confines the flow of liquid to the top of the Pd contact and provides space to insert RE and CE (Table 6).

6.4.3 Electrical measurements:

We used a potential cut-off of – 400 mV for proton current measurement via Autolab. In the first step, we applied - 400 mV for 600 seconds to induce H^+ to flow from the solution into the Pd contact to form PdH_x and measured the proton current I_{H+}. In the second step, $V_{H+} = 0$ mV transferred H^+ from the PdH_x contact into the solution to show that at a neutral pH, the protochemical potential of H^+ in the PdH_x contact is higher than the protochemical potential of H^+ in the solution.

EIS measurements were performed with Autolab, recording impedance spectra in the frequency range between 0.1 Hz–100 kHz. An AC voltage of 0.01 V and a DC voltage of 0 V versus OCP (open circuit potential) were applied (Figure 33 and Table 7).

6.4.4 SLB formation:

DOPC liposomes were extracted and dried from a vial containing DOPC and chloroform via using nitrogen to blow it. And thus, the vial was put into a vacuum chamber for at least 6 hours to dry DOPC extremely. Followingly, PBS buffer solution (pH = 7.5) was added into the vial for rehydration with the exact density (1 mg ml^{-1}).

Sonication and vortex promote dissolution of DOPC in buffer solution and then 220 nm sterilizing filters purchased from Millex confine the size of vesicles. Before the deposition of SLBs on Pd contacts, the surface was hydrophilized by oxygen plasma[216]. The vesicle solution was introduced and dispensed in the microfluidic channel and the device was gently agitated for at least 8 h in high relative humidity (~ 95 % RH) to ensure vesicle fusion[217,218] and the SLB formation, followed by rinsing with buffer solution to wash away vesicle residue that was unfused. Essentially, the SLBs mimic cell membranes, electrically insulate the Pd contact and divide the solution into two volumes: cis and trans. SLBs are not in direct contact with the surface of the solid substrate because of a very thin hydration layer of 1—2 nm thickness between Pd contact and SLBs on this cis-side[219]. The separation offered by this thin layer facilitates the insertion of ion channels, such as the DNA nanopores by supplying lubrication and mobility to the SLBs[220].

6.4.5 Fluorescence imaging and fluorescence recovery after photobleaching measurements (FRAP)

The formation and quality of SLBs are validated by Fluorescence Recovery After Photobleaching (FRAP) (Figure 34), where fluorescent liposomes were combined with the DOPC lipids to form the bilayer. The samples were flushed with PBS buffer several times to remove excess fluorophores. Fluorescence imaging and FRAP experiments were performed on confocal microscopy (Leica, SP5 Confocal Microscope) with a 63× water immersion objective. DNA nanopores tagged with 488 Atto fluorophores on

either end of the nano barrel were used for the fluorescence imaging experiments. 488 nm Ar laser was used for fluorescence imaging, and 543 nm and 594 nm HeNe laser was used for photobleaching. A 20 μm diameter spot in the supported lipid bilayer was photobleached, and its fluorescence intensity recovery was monitored for 30 minutes. The fluorescence intensity of diameter and changes over time were analyzed with Image J and fitted using a Gaussian function[221]. The diffusion coefficient was calculated with the below equation:

$$D = \frac{R_n^2 + R_e^2}{T_{1/2}} \tag{22}$$

where R_n is the nominal radius from the user defined spot, R_e is the effective radius from the bleached radius right after the bleaching process, $T_{1/2}$ is half time to recovery and the diffusion coefficient was 8.52 μm^2/sec.

6.4.6 DNA nanopores folding and characterization:

The 6HB-2C DNA nanopore was assembled by heating and cooling an equimolar mixture of 11 unmodified and 2 TEG-Chol modified DNA strands (for sequences, see Table 5). 10 μL of each of 1 μM ssDNA were mixed along with 6 μL of 200 mM $MgCl_2$, 10 μL of 10x TE (pH = 8.0) and MQ water to prepare a 100 μL folding mixture. The mixture was divided into 50 μL aliquots so that the solution maintains an even contact with the heating elements of the thermocycler. They were first heated to a temperature of 95°C and then sequentially cooled to 16 °C by reducing the temperature at a rate of 0.13 °C per minute. For 6HB control nanopores without cholesterol anchors (6HB) and

other variations such as 6HB-1C, and 6HB-3C, 6HB-2B, 6HB-2C, 6HB-2C-2B, 6HB-2C-2AP and fluorescent tagged nanopores, the sequences were appropriately modified (for sequences, see Table 5).

The self-assembled structures were then characterized to confirm the correct and successful formation of the DNA nanopore. Since the structures were formed from equimolar ratios of ssDNA strands, purification was not necessary. The concentration of the resulting double stranded DNA nanostructures was analyzed with a spectrophotometer using UV absorbance spectra. Native gel electrophoresis was performed to verify the completeness of the folded structure and to verify the migration of the control nanopores without any cholesterol vs. migration of 6HB-1C, 6HB-2C, and 6HB-3C nanopores (Figure 31a). The 6HB-2C nanopores yielded a band, which migrated to the similar height as a control nanopore without any cholesterol anchors (Figure 31a, lanes 3 and 5 respectively, main band migrating at 300 bp marker). Furthermore, DLS established the monomeric nature of the nanobarrels, as only a single peak (volume-based size distribution) with an average hydrodynamic radius of 9.73 nm was observed (blue curve in Figure 31c). Intensity based size-correlograms (Figure 31d) and the polydispersity index (PI) values (Table 7) for the 6HB and 6HB-3C nanopores show presence of multiple-size distributions containing possible higher-order aggregates since unpurified samples were used directly for the experiments. For biotin modified nanopores, 6HB-2B and 6HB-2B-2C, the gel electrophoresis showed the accessibility of the biotin tags as slower migration patterns and dimer/quadrate aggregation patterns were observed in presence of excess Streptavidin protein (1x:20x

concentration ratios) (Figure. 31b lanes 6 and 8). No such migration pattern changes were observed in non-biotinylated nanopores, showing they were appropriate as controls (Figure 31b lanes 7).

Table 7: Polydispersity Index values for dynamic light scattering data

Name	6HB	6HB-3C
Z-Average (nm)	138.8	1097
Polydispersity Index (PI)	0.8249	0.7364
Peak One Width by Number (nm)	2.636	12.25
Peak One Mean by Number (nm)	9.755	60.48
Peak Two Width by Number (nm)	-	165.3
Peak Two Mean by Number (nm)	-	683.2
Intercept	0.7152	0.5497
In Range (%)	90.4	81.02
Fit Error	0.03045	0.00771

Intensity based Polydispersity index (PI) and hydrodynamic Z-average size (cumulants mean) values for 6HB and 6HB-3C nanopores averaged over 5 scans as observed on Malvern zetasizer instrument. Since a small percentage of aggregates are expected and can heavily skew the calculations owing to large scattering effects, number based mean values are used and contrasted against the intensity based-calculations to provide a more relevant estimate of the nanopore population distribution.

6.4.7 Simulation:

We perform molecular dynamics (MD) simulations with NAMD software53,54 using periodic boundary conditions. 6HB DNA nanopore design is generated with caDNAno and converted into all atom structures using automated conversation program which is available at the nanoHub web site. We covalently bound cholesterol-TEG (chol-TEG) extensions to 3'ends of designed staple strands by using the 'patches' provided in the NAMD tutorial55. We, then, inserted the chol-TEG conjugated 6HB DNA nanopore into the pre-equilibrated DOPC lipid bilayer membrane using the CHARMM-GUI website56. CHARMM 3657 and CGenFF58 force fields were used to define chol-TEG conjugated DNA nanostructure. We placed the whole system inside 0.15 mM KCl electrolyte after removing overlapping lipid and water molecules. For water molecules and ions TIP3P59 force field was used. After generating the initial system, we minimized the energy of lipid molecules for 50000 steps by keeping chol-TEG conjugated DNA nanostructure fixed. Next, we minimized the energy of the whole system while keeping the chol-TEG conjugated DNA nanopore harmonically restrained using the exponent of 2 for the harmonic constraint energy function for another 50000 steps. We released all the harmonic constraints and equilibrated the whole system for 3 ns prior MD production runs. Finally, the whole system was simulated for 64 ns at 295 K with a 2 fs timestep by saving the coordinates at every 4 fs. During the simulations, the VDW cutoff value is taken to be 12 Å. Electrostatic interactions are computed using the PME method60, and the SHAKE algorithm is applied to keep H bonds rigid.

7. Outlook

Bioelectronics provides a variety of novel methods to ion out the major open challenges from traditional electronics and thus confer various applications of ion conducting materials in iontronic devices and soft robotics and ion channels based platforms. In particular, utilizing their unique stretchability, transparency, and ionic conductivity in these fields has led to the development of several novel hydrogel interfaces. However, widespread implementation of hydrogels in such interfaces is limited by the difficulties associated with fabricating them. Hydrogel degradation and dehydration is another cause of concern and limits the ability to integrate them into microfabricated devices. Hydrogels are also difficult to rapidly prototype thereby restricting large scale production of hydrogel-integrated devices. Most research so far has been focused on material development but there is still need for either materials that are robust to device integration or integration strategies that maintain the properties of the hydrogel. There is a need for extensive research both in fabrication processes as well as hydrogel properties. The scope for further innovative research in improving fabrication strategies, material properties, and integration mechanisms opens doors for several exciting opportunities to build better interfaces between biology and electronics.

Besides, the integration of SLBs with bioelectronics offers a versatile and powerful platform for fundamental studies of transmembrane channel conductivity and potential applications in sensing. SLBs serve a dual role in this context, acting as passivating layers to isolate the devices from the external environment and as hosts for specific

transmembrane channels. The diverse range of bioelectronic platforms describe in this review demonstrates the potential of SLB integration with different materials, including 1D and 2D materials, organic bioelectronics, and bioprotonic devices. However, there is room for improvement in many areas, such as the stability of the lipid bilayer, miniaturization, and optimization of the signal-to-noise ratio for more accurate measurements of individual ion channels. With the continued improvements of SLB-intergraded bioelectronics, it may be possible to move beyond current applications towards multi-electrode multiplexed patch clamping, where individual transmembrane channels can be exposed to different conditions in parallel. This would provide an unprecedented level of detail in the study of transmembrane channel function, enabling the investigation of afflictions that affect transmembrane channels or fast and efficient drug screening.

8. Reference

1 Berggren, M. & Richter-Dahlfors, A. Organic Bioelectronics. *Advanced Materials* **19**, 3201-3213 (2007). https://doi.org:https://doi.org/10.1002/adma.200700419

2 Rivnay, J., Owens, R. M. & Malliaras, G. G. The Rise of Organic Bioelectronics. *Chemistry of Materials* **26**, 679-685 (2014). https://doi.org:10.1021/cm4022003

3 Zhang, A. & Lieber, C. M. Nano-Bioelectronics. *Chemical Reviews* **116**, 215-257 (2016). https://doi.org:10.1021/acs.chemrev.5b00608

4 Piccolino, M. Animal electricity and the birth of electrophysiology: the legacy of Luigi Galvani. *Brain Res Bull* **46**, 381-407 (1998). https://doi.org:10.1016/s0361-9230(98)00026-4

5 Young, J. Z. The Functioning of the Giant Nerve Fibres of the Squid. *The Journal of Experimental Biology* **15**, 170-185 (1938).

6 Hodgkin, A. L., Huxley, A. F. & Katz, B. Measurement of current-voltage relations in the membrane of the giant axon of Loligo. *J Physiol* **116**, 424-448 (1952). https://doi.org:10.1113/jphysiol.1952.sp004716

7 Cingolani, E., Goldhaber, J. I. & Marbán, E. Next-generation pacemakers: from small devices to biological pacemakers. *Nature Reviews Cardiology* **15**, 139-150 (2018). https://doi.org:10.1038/nrcardio.2017.165

8 Miocinovic, S., Somayajula, S., Chitnis, S. & Vitek, J. L. History, applications, and mechanisms of deep brain stimulation. *JAMA Neurol* **70**, 163-171 (2013). https://doi.org:10.1001/2013.jamaneurol.45

9 Deisseroth, K. *et al*. Next-Generation Optical Technologies for Illuminating Genetically Targeted Brain Circuits. *The Journal of Neuroscience* **26**, 10380 (2006). https://doi.org:10.1523/JNEUROSCI.3863-06.2006

10 Kringelbach, M. L., Jenkinson, N., Owen, S. L. F. & Aziz, T. Z. Translational principles of deep brain stimulation. *Nature Reviews Neuroscience* **8**, 623-635 (2007). https://doi.org:10.1038/nrn2196

11 Someya, T., Bao, Z. & Malliaras, G. G. The rise of plastic bioelectronics. *Nature* **540**, 379-385 (2016). https://doi.org:10.1038/nature21004

12 Lacour, S. P., Courtine, G. & Guck, J. Materials and technologies for soft implantable neuroprostheses. *Nature Reviews Materials* **1**, 16063 (2016). https://doi.org:10.1038/natrevmats.2016.63

13 Head, S. J. *et al*. The impact of prosthesis-patient mismatch on long-term survival after aortic valve replacement: a systematic review and meta-analysis of 34 observational studies comprising 27 186 patients with 133 141 patient-years. *Eur Heart J* **33**, 1518-1529 (2012). https://doi.org:10.1093/eurheartj/ehs003

14 Jia, M. & Rolandi, M. Soft and Ion-Conducting Materials in Bioelectronics: From Conducting Polymers to Hydrogels. *Advanced Healthcare Materials* **9**, 1901372 (2020). https://doi.org:https://doi.org/10.1002/adhm.201901372

15 Chun, H. & Chung, T. D. Iontronics. *Annual Review of Analytical Chemistry* **8**, 441-462 (2015). https://doi.org:10.1146/annurev-anchem-071114-040202

16 Horowitz, G. Organic Field-Effect Transistors. *Advanced Materials* **10**, 365-377 (1998). https://doi.org:https://doi.org/10.1002/(SICI)1521-4095(199803)10:5<365::AID-ADMA365>3.0.CO;2-U

17 Rivnay, J. *et al*. Organic electrochemical transistors. *Nature Reviews Materials* **3**, 17086 (2018). https://doi.org:10.1038/natrevmats.2017.86

18 Audi, M. & de Simon, M. Ion pumps. *Vacuum* **37**, 629-636 (1987). https://doi.org:https://doi.org/10.1016/0042-207X(87)90048-0

19 Gadsby, D. C. Ion channels versus ion pumps: the principal difference, in principle. *Nature Reviews Molecular Cell Biology* **10**, 344-352 (2009). https://doi.org:10.1038/nrm2668

20 Liao, C. *et al*. Flexible Organic Electronics in Biology: Materials and Devices. *Advanced Materials* **27**, 7493-7527 (2015). https://doi.org:https://doi.org/10.1002/adma.201402625

21 Meka, V. S. *et al*. A comprehensive review on polyelectrolyte complexes. *Drug Discovery Today* **22**, 1697-1706 (2017). https://doi.org:https://doi.org/10.1016/j.drudis.2017.06.008

22 Arbring Sjöström, T. *et al*. A Decade of Iontronic Delivery Devices. *Advanced Materials Technologies* **3**, 1700360 (2018). https://doi.org:https://doi.org/10.1002/admt.201700360

23 Rivnay, J. *et al*. Structural control of mixed ionic and electronic transport in conducting polymers. *Nature Communications* **7**, 11287 (2016). https://doi.org:10.1038/ncomms11287

24 Kayser, L. V. & Lipomi, D. J. Stretchable Conductive Polymers and Composites Based on PEDOT and PEDOT:PSS. *Advanced Materials* **31**, 1806133 (2019). https://doi.org:https://doi.org/10.1002/adma.201806133

25 Kiessling, V., Domanska, M. K., Murray, D., Wan, C. & Tamm, L. K. in *Wiley Encyclopedia of Chemical Biology* 1-12.

26 Tero, R. Substrate Effects on the Formation Process, Structure and Physicochemical Properties of Supported Lipid Bilayers. *Materials* **5**, 2658-2680 (2012).

27 Castellana, E. T. & Cremer, P. S. Solid supported lipid bilayers: From biophysical studies to sensor design. *Surface Science Reports* **61**, 429-444 (2006). https://doi.org:https://doi.org/10.1016/j.surfrep.2006.06.001

28 Bruce, P. G. *Solid state electrochemistry*. Vol. 5 (Cambridge university press, 1997).

29 Owens, B. B. & Argue, G. R. High-conductivity solid electrolytes: MAg4I5. *Science* **157**, 308-310 (1967).

30 Yao, Y.-F. Y. & Kummer, J. Ion exchange properties of and rates of ionic diffusion in beta-alumina. *Journal of Inorganic and Nuclear Chemistry* **29**, 2453-2475 (1967).

31 Mauritz, K. A. & Moore, R. B. State of understanding of Nafion. *Chemical reviews* **104**, 4535-4586 (2004).

32 Paulsen, B. D., Tybrandt, K., Stavrinidou, E. & Rivnay, J. Organic mixed ionic–electronic conductors. *Nature materials* **19**, 13-26 (2020).

33 Barrande, M., Bouchet, R. & Denoyel, R. Tortuosity of porous particles. *Analytical chemistry* **79**, 9115-9121 (2007).

34 Barros Jr, W. Solvent self-diffusion dependence on the swelling degree of a hydrogel. *Physical Review E* **99**, 052501 (2019).

35 Cao, J.-H., Zhu, B.-K. & Xu, Y.-Y. Structure and ionic conductivity of porous polymer electrolytes based on PVDF-HFP copolymer membranes. *Journal of membrane science* **281**, 446-453 (2006).

36 Goodenough, J. B. Proton conductors: Solids, membranes, and gels–materials and devices. Edited by Phillippe Colomban, Cambridge University Press, Cambridge, UK 1992, £ 75, xxxii, 581 pp., hardcover, ISBN 0-521-38317-X. *Advanced Materials* **5**, 683-685 (1993). https://doi.org:https://doi.org/10.1002/adma.19930050923

37 Zuo, Z., Fu, Y. & Manthiram, A. Novel Blend Membranes Based on Acid-Base Interactions for Fuel Cells. *Polymers* **4**, 1627-1644 (2012).

38 Miyake, T. & Rolandi, M. Grotthuss mechanisms: from proton transport in proton wires to bioprotonic devices. *Journal of Physics: Condensed Matter* **28**, 023001 (2016). https://doi.org:10.1088/0953-8984/28/2/023001

39 Jia, M., Kim, J., Nguyen, T., Duong, T. & Rolandi, M. Natural biopolymers as proton conductors in bioelectronics. *Biopolymers* **112**, e23433 (2021). https://doi.org:https://doi.org/10.1002/bip.23433

40 Ma, J. & Sahai, Y. Chitosan biopolymer for fuel cell applications. *Carbohydrate Polymers* **92**, 955-975 (2013). https://doi.org:https://doi.org/10.1016/j.carbpol.2012.10.015

41 Wu, G., Zhang, J., Wan, X., Yang, Y. & Jiang, S. Chitosan-based biopolysaccharide proton conductors for synaptic transistors on paper

substrates. *Journal of Materials Chemistry C* **2**, 6249-6255 (2014). https://doi.org:10.1039/C4TC00652F

42 Amit, M. *et al*. Measuring Proton Currents of Bioinspired Materials with Metallic Contacts. *ACS Applied Materials & Interfaces* **10**, 1933-1938 (2018). https://doi.org:10.1021/acsami.7b16640

43 Jia, M., Ray, S., Breault, R. & Rolandi, M. Control of pH in bioelectronics and applications. *APL Materials* **8** (2020). https://doi.org:10.1063/5.0027464

44 Park, C. S., Lee, C. & Kwon, O. S. Conducting Polymer Based Nanobiosensors. *Polymers* **8**, 249 (2016).

45 Gangopadhyay, R. & De, A. Conducting Polymer Nanocomposites: A Brief Overview. *Chemistry of Materials* **12**, 608-622 (2000). https://doi.org:10.1021/cm990537f

46 Twenty-five years of conducting polymers. *Chemical Communications*, 1-4 (2003). https://doi.org:10.1039/B210718J

47 Kumar, D. & Sharma, R. C. Advances in conductive polymers. *European Polymer Journal* **34**, 1053-1060 (1998). https://doi.org:https://doi.org/10.1016/S0014-3057(97)00204-8

48 Ravichandran, R., Sundarrajan, S., Venugopal, J. R., Mukherjee, S. & Ramakrishna, S. Applications of conducting polymers and their issues in biomedical engineering. *J R Soc Interface* **7 Suppl 5**, S559-579 (2010). https://doi.org:10.1098/rsif.2010.0120.focus

49 Ahmed, E. M. Hydrogel: Preparation, characterization, and applications: A review. *Journal of advanced research* **6**, 105-121 (2015).

50 Wichterle, O. & Lim, D. Hydrophilic gels for biological use. *Nature* **185**, 117-118 (1960).

51 Cascone, S. & Lamberti, G. Hydrogel-based commercial products for biomedical applications: A review. *International Journal of Pharmaceutics* **573**, 118803 (2020).

52 Li, J. & Mooney, D. J. Designing hydrogels for controlled drug delivery. *Nature Reviews Materials* **1**, 1-17 (2016).

53 Gupta, A. *et al*. The production and application of hydrogels for wound management: A review. *European Polymer Journal* **111**, 134-151 (2019).

54 Distler, T. & Boccaccini, A. R. 3D printing of electrically conductive hydrogels for tissue engineering and biosensors–A review. *Acta Biomaterialia* **101**, 1-13 (2020).

55 Eslahi, N., Abdorahim, M. & Simchi, A. Smart polymeric hydrogels for cartilage tissue engineering: a review on the chemistry and biological functions. *Biomacromolecules* **17**, 3441-3463 (2016).

56 Yuk, H., Lu, B. & Zhao, X. Hydrogel bioelectronics. *Chemical Society Reviews* **48**, 1642-1667 (2019). https://doi.org:10.1039/c8cs00595h

57 Seliktar, D. Designing Cell-Compatible Hydrogels for Biomedical Applications. *Science* **336**, 1124-1128 (2012). https://doi.org:10.1126/science.1214804

58 Lee, K. Y. & Mooney, D. J. Hydrogels for Tissue Engineering. *Chemical Reviews* **101**, 1869-1880 (2001). https://doi.org:10.1021/cr000108x

59 Yang, C. & Suo, Z. Hydrogel ionotronics. *Nature Reviews Materials* **3**, 125 (2018).

60 Tuszynski, J. A. in *Brain and Human Body Modeling: Computational Human Modeling at EMBC 2018* (eds Sergey Makarov, Marc Horner, & Gregory Noetscher) 195-208 (Springer International Publishing, 2019).

61 Rong, Q., Lei, W. & Liu, M. Conductive Hydrogels as Smart Materials for Flexible Electronic Devices. *Chemistry – A European Journal* **24**, 16930-16943 (2018). https://doi.org:https://doi.org/10.1002/chem.201801302

62 Xu, J., Tsai, Y.-L. & Hsu, S.-h. Design Strategies of Conductive Hydrogel for Biomedical Applications. *Molecules* **25**, 5296 (2020).

63 B. Rufato, K. *et al*. in *Hydrogels - Smart Materials for Biomedical Applications* (2019).

64 Hu, W., Wang, Z., Xiao, Y., Zhang, S. & Wang, J. Advances in crosslinking strategies of biomedical hydrogels. *Biomaterials Science* **7**, 843-855 (2019). https://doi.org:10.1039/C8BM01246F

65 Lee, C.-J. *et al*. Ionic Conductivity of Polyelectrolyte Hydrogels. *ACS Applied Materials & Interfaces* **10**, 5845-5852 (2018). https://doi.org:10.1021/acsami.7b15934

66 Zygadło-Monikowska, E., Florjańczyk, Z., Wielgus-Barry, E. & Hildebrand, E. Proton conducting gel polyelectrolytes based on 2-acrylamido-2-methyl-1-

propanesulfonic acid (AMPSA) copolymers: Part II. Hydrogels. *Journal of Power Sources* **159**, 392-398 (2006). https://doi.org:https://doi.org/10.1016/j.jpowsour.2006.02.038

67 Lee, K.-T. & Wu, N.-L. Manganese oxide electrochemical capacitor with potassium poly(acrylate) hydrogel electrolyte. *Journal of Power Sources* **179**, 430-434 (2008). https://doi.org:https://doi.org/10.1016/j.jpowsour.2007.12.057

68 Tang, Q., Chen, M., Wang, G., Bao, H. & Saha, P. A facile prestrain-stick-release assembly of stretchable supercapacitors based on highly stretchable and sticky hydrogel electrolyte. *Journal of Power Sources* **284**, 400-408 (2015). https://doi.org:https://doi.org/10.1016/j.jpowsour.2015.03.059

69 Katzenberg, A., Muñoz Davila, C., Chen, B., Siboonruang, T. & Modestino, M. A. Acid-Doped Hydrogel Electrolytes for Electrocatalyst Interfaces. *ACS Applied Polymer Materials* **2**, 2046-2054 (2020). https://doi.org:10.1021/acsapm.0c00214

70 Shi, Z. *et al*. Electroconductive natural polymer-based hydrogels. *Biomaterials* **111**, 40-54 (2016). https://doi.org:https://doi.org/10.1016/j.biomaterials.2016.09.020

71 Tan, H. & Marra, K. G. Injectable, Biodegradable Hydrogels for Tissue Engineering Applications. *Materials* **3**, 1746-1767 (2010).

72 Drury, J. L. & Mooney, D. J. Hydrogels for tissue engineering: scaffold design variables and applications. *Biomaterials* **24**, 4337-4351 (2003). https://doi.org:https://doi.org/10.1016/S0142-9612(03)00340-5

73 Jacobson, K., Liu, P. & Lagerholm, B. C. The lateral organization and mobility of plasma membrane components. *Cell* **177**, 806-819 (2019).

74 Hardy, G. J., Nayak, R. & Zauscher, S. Model cell membranes: Techniques to form complex biomimetic supported lipid bilayers via vesicle fusion. *Current Opinion in Colloid & Interface Science* **18**, 448-458 (2013). https://doi.org:10.1016/j.cocis.2013.06.004

75 Di Iorio, D., Verheijden, M. L., Van Der Vries, E., Jonkheijm, P. & Huskens, J. Weak Multivalent Binding of Influenza Hemagglutinin Nanoparticles at a Sialoglycan-Functionalized Supported Lipid Bilayer. *ACS Nano* **13**, 3413-3423 (2019). https://doi.org:10.1021/acsnano.8b09410

76 Lu, S.-H. *et al*. Identifying cancer origin using circulating tumor cells. *Cancer Biology & Therapy* **17**, 430-438 (2016). https://doi.org:10.1080/15384047.2016.1141839

77 Yorulmaz Avsar, S. *et al*. Immobilization Strategies for Functional Complement Convertase Assembly at Lipid Membrane Interfaces. *Langmuir* **33**, 7332-7342 (2017). https://doi.org:10.1021/acs.langmuir.7b01465

78 Park, Y. *et al*. Bionanoelectronic platform with a lipid bilayer/CVD-grown MoS2 hybrid. *Biosensors and Bioelectronics* **142**, 111512 (2019).

79 Hodnik, V. & Anderluh, G. in *Lipid-Protein Interactions* 23-36 (Springer, 2013).

80 Cho, N.-J., Frank, C. W., Kasemo, B. & Höök, F. Quartz crystal microbalance with dissipation monitoring of supported lipid bilayers on various substrates. *Nature protocols* **5**, 1096-1106 (2010).

81 Okahata, Y. & Ebato, H. Application of a quartz-crystal microbalance for detection of phase transitions in liquid crystals and lipid multibilayers. *Analytical Chemistry* **61**, 2185-2188 (1989).

82 Reviakine, I. & Brisson, A. Formation of Supported Phospholipid Bilayers from Unilamellar Vesicles Investigated by Atomic Force Microscopy. *Langmuir* **16**, 1806-1815 (2000). https://doi.org:10.1021/la9903043

83 Vallejo, A. & Gervasi, C. EIS studies of valinomycin-mediated K+ transport through supported lipid bilayers. *Journal of Electroanalytical Chemistry* **603**, 51-58 (2007).

84 Wang, V. Q. & Liu, S. A General Model of Ion Passive Transmembrane Transport Based on Ionic Concentration. *Frontiers in Computational Neuroscience* **12** (2019). https://doi.org:10.3389/fncom.2018.00110

85 Wallace, B. A. Gramicidin Channels and Pores. *Annual Review of Biophysics and Biophysical Chemistry* **19**, 127-157 (1990). https://doi.org:10.1146/annurev.bb.19.060190.001015

86 Nagaraj, R. & Balaram, P. Alamethicin, a transmembrane channel. *Accounts of Chemical Research* **14**, 356-362 (1981).

87 Zhang, S. J. & Jackson, M. B. GABA-activated chloride channels in secretory nerve endings. *Science* **259**, 531-534 (1993).

88 Xie, G. *et al*. Bacteriorhodopsin-inspired light-driven artificial molecule motors for transmembrane mass transportation. *Angewandte Chemie International Edition* **57**, 16708-16712 (2018).

89 Deisseroth, K. & Hegemann, P. The form and function of channelrhodopsin. *Science* **357**, eaan5544 (2017). https://doi.org:doi:10.1126/science.aan5544

90 Geng, J. *et al*. Stochastic transport through carbon nanotubes in lipid bilayers and live cell membranes. *Nature* **514**, 612-615 (2014). https://doi.org:10.1038/nature13817

91 Thomsen, R. P. *et al*. A large size-selective DNA nanopore with sensing applications. *Nature Communications* **10** (2019). https://doi.org:10.1038/s41467-019-13284-1

92 Jiang, T. *et al*. Single-chain heteropolymers transport protons selectively and rapidly. *Nature* **577**, 216-220 (2020). https://doi.org:10.1038/s41586-019-1881-0

93 Miyake, T., Josberger, E. E., Keene, S., Deng, Y. & Rolandi, M. An enzyme logic bioprotonic transducer. *APL Materials* **3**, 014906 (2014). https://doi.org:10.1063/1.4900886

94 Chang, B.-Y. & Park, S.-M. Electrochemical Impedance Spectroscopy. *Annual Review of Analytical Chemistry* **3**, 207-229 (2010). https://doi.org:10.1146/annurev.anchem.012809.102211

95 Nagle, J. F. & Morowitz, H. J. Molecular mechanisms for proton transport in membranes. *Proceedings of the National Academy of Sciences* **75**, 298-302 (1978). https://doi.org:doi:10.1073/pnas.75.1.298

96 Nagle, J. F., Mille, M. & Morowitz, H. J. Theory of hydrogen bonded chains in bioenergetics. *The Journal of Chemical Physics* **72**, 3959-3971 (1980). https://doi.org:10.1063/1.439674

97 Walz, D. & Caplan, S. R. Bacterial flagellar motor and H(+)/ATP synthase: two proton-driven rotary molecular devices with different functions. *Bioelectrochemistry* **55**, 89-92 (2002). https://doi.org:10.1016/s1567-5394(01)00162-1

98 Cukierman, S. Et tu, Grotthuss! and other unfinished stories. *Biochimica et Biophysica Acta (BBA) - Bioenergetics* **1757**, 876-885 (2006). https://doi.org:https://doi.org/10.1016/j.bbabio.2005.12.001

99 Jia, M., Ray, S., Breault, R. & Rolandi, M. Control of pH in bioelectronics and applications. *APL Materials* **8**, 120704 (2020). https://doi.org:10.1063/5.0027464

100 Chopra, N., Gavalas, V. G., Bachas, L. G., Hinds, B. J. & Bachas, L. G. Functional One-Dimensional Nanomaterials: Applications in Nanoscale Biosensors. *Analytical Letters* **40**, 2067-2096 (2007). https://doi.org:10.1080/00032710701567170

101 Feigel, I. M., Vedala, H. & Star, A. Biosensors based on one-dimensional nanostructures. *Journal of Materials Chemistry* **21**, 8940-8954 (2011).

102 Misra, N. *et al*. Bioelectronic silicon nanowire devices using functional membrane proteins. *Proceedings of the National Academy of Sciences* **106**, 13780-13784 (2009). https://doi.org:doi:10.1073/pnas.0904850106

103 Sarkar, D. *et al*. MoS2 field-effect transistor for next-generation label-free biosensors. *ACS nano* **8**, 3992-4003 (2014).

104 Jin, K., Xie, L., Tian, Y. & Liu, D. Au-modified monolayer MoS2 sensor for DNA detection. *The Journal of Physical Chemistry C* **120**, 11204-11209 (2016).

105 Park, H. *et al*. Label-free and recalibrated multilayer MoS2 biosensor for point-of-care diagnostics. *ACS applied materials & interfaces* **9**, 43490-43497 (2017).

106 Hemmatian, Z. *et al*. Electronic control of H+ current in a bioprotonic device with Gramicidin A and Alamethicin. *Nature Communications* **7**, 12981 (2016). https://doi.org:10.1038/ncomms12981

107 Soto-Rodríguez, J., Hemmatian, Z., Josberger, E. E., Rolandi, M. & Baneyx, F. A Palladium-Binding Deltarhodopsin for Light-Activated Conversion of Protonic to Electronic Currents. *Advanced Materials* **28**, 6581-6585 (2016). https://doi.org:https://doi.org/10.1002/adma.201600222

108 Spencer, K. C. *et al*. Characterization of mechanically matched hydrogel coatings to improve the biocompatibility of neural implants. *Scientific reports* **7**, 1-16 (2017).

109 Cho, Y., Park, S., Lee, J. & Yu, K. J. Emerging Materials and Technologies with Applications in Flexible Neural Implants: A Comprehensive Review of Current Issues with Neural Devices. *Advanced Materials*, 2005786 (2021).

110 Goding, J., Gilmour, A., Martens, P., Poole-Warren, L. & Green, R. Interpenetrating conducting hydrogel materials for neural interfacing electrodes. *Advanced healthcare materials* **6**, 1601177 (2017).

111 Vedadghavami, A. *et al*. Manufacturing of hydrogel biomaterials with controlled mechanical properties for tissue engineering applications. *Acta biomaterialia* **62**, 42-63 (2017).

112 Jia, M., Kim, J., Nguyen, T., Duong, T. & Rolandi, M. Natural biopolymers as proton conductors in bioelectronics. *Biopolymers*, e23433 (2021).

113 Simon, D. T., Gabrielsson, E. O., Tybrandt, K. & Berggren, M. Organic bioelectronics: bridging the signaling gap between biology and technology. *Chemical Reviews* **116**, 13009-13041 (2016).

114 Nyamayaro, K. *et al*. Toward Biodegradable Electronics: Ionic Diodes Based on a Cellulose Nanocrystal–Agarose Hydrogel. *ACS Applied Materials & Interfaces* **12**, 52182-52191 (2020).

115 Yin, M.-J., Yin, Z., Zhang, Y., Zheng, Q. & Zhang, A. P. Micropatterned elastic ionic polyacrylamide hydrogel for low-voltage capacitive and organic thin-film transistor pressure sensors. *Nano Energy* **58**, 96-104 (2019).

116 Gao, D. & Lee, P. S. Rectifying ionic current with ionoelastomers. *Science* **367**, 735-736 (2020).

117 Jia, M. *et al*. Bioelectronic control of chloride ions and concentration with Ag/AgCl contacts. *APL Materials* **8**, 091106 (2020). https://doi.org:10.1063/5.0013867

118 Selberg, J. *et al*. Machine Learning-Driven Bioelectronics for Closed-Loop Control of Cells. *Advanced Intelligent Systems* **2**, 2000140 (2020).

119 Poxson, D. J. *et al*. Capillary-Fiber Based Electrophoretic Delivery Device. *ACS Applied Materials & Interfaces* **11**, 14200-14207 (2019). https://doi.org:10.1021/acsami.8b22680

120 Meka, V. S. *et al*. A comprehensive review on polyelectrolyte complexes. *Drug discovery today* **22**, 1697-1706 (2017).

121 Caccavo, D. An overview on the mathematical modeling of hydrogels' behavior for drug delivery systems. *International journal of pharmaceutics* **560**, 175-190 (2019).

122 Guo, Y. *et al*. Synergistic energy nanoconfinement and water activation in hydrogels for efficient solar water desalination. *ACS nano* **13**, 7913-7919 (2019).

123 Zhou, Y. *et al*. Highly stretchable, elastic, and ionic conductive hydrogel for artificial soft electronics. *Advanced Functional Materials* **29**, 1806220 (2019).

124 Goding, J., Vallejo-Giraldo, C., Syed, O. & Green, R. Considerations for hydrogel applications to neural bioelectronics. *Journal of Materials Chemistry B* **7**, 1625-1636 (2019).

125 Kwon, H. J., Osada, Y. & Gong, J. P. Polyelectrolyte gels-fundamentals and applications. *Polymer journal* **38**, 1211-1219 (2006).

126 Durmaz, S. & Okay, O. Acrylamide/2-acrylamido-2-methylpropane sulfonic acid sodium salt-based hydrogels: synthesis and characterization. *Polymer* **41**, 3693-3704 (2000).

127 McAvoy, K., Jones, D. & Thakur, R. R. S. Synthesis and characterisation of photocrosslinked poly (ethylene glycol) diacrylate implants for sustained ocular drug delivery. *Pharmaceutical research* **35**, 1-17 (2018).

128 Yan, N., Paul, D. R. & Freeman, B. D. Water and ion sorption in a series of cross-linked AMPS/PEGDA hydrogel membranes. *Polymer* **146**, 196-208 (2018).

129 Seitanidou, M., Tybrandt, K., Berggren, M. & Simon, D. T. Overcoming transport limitations in miniaturized electrophoretic delivery devices. *Lab on a Chip* **19**, 1427-1435 (2019).

130 Nalampang, K., Panjakha, R., Molloy, R. & Tighe, B. J. Structural effects in photopolymerized sodium AMPS hydrogels crosslinked with poly (ethylene glycol) diacrylate for use as burn dressings. *Journal of Biomaterials Science, Polymer Edition* **24**, 1291-1304 (2013).

131 Guo, Q.-H. *et al*. Single-Crystal Polycationic Polymers Obtained by Single-Crystal-to-Single-Crystal Photopolymerization. *Journal of the American Chemical Society* **142**, 6180-6187 (2020).

132 Strauss, M. J. *et al*. Diverse Proton-Conducting Nanotubes via a Tandem Macrocyclization and Assembly Strategy. *Journal of the American Chemical Society* (2021).

133 Selberg, J., Jia, M. & Rolandi, M. Proton conductivity of glycosaminoglycans. *PLoS One* **14**, e0202713 (2019).

134 Karadağ, E., Nalbantoğlu, A., Kundakcı, S. & Üzüm, Ö. B. Highly swollen polymer/clay composite sorbent-based AAm/AMPS hydrogels and semi-IPNs composed of carboxymethyl cellulose and montmorillonite and cross-linked by PEGDA. *Polymer-Plastics Technology and Engineering* **53**, 54-64 (2014).

135 Bhattacharyya, A. *et al*. Hydrogel compression and polymer osmotic pressure. *Biotribology* **22**, 100125 (2020).

136 Flory, P. J. *Principles of polymer chemistry*. (Cornell University Press, 1953).

137 Chavda, H. & Patel, C. Effect of crosslinker concentration on characteristics of superporous hydrogel. *International journal of pharmaceutical investigation* **1**, 17 (2011).

138 Omidian, H., Rocca, J. G. & Park, K. Advances in superporous hydrogels. *Journal of controlled release* **102**, 3-12 (2005).

139 Garrouch, A. A., Ali, L. & Qasem, F. Using diffusion and electrical measurements to assess tortuosity of porous media. *Industrial & engineering chemistry research* **40**, 4363-4369 (2001).

140 Hormann, K., Baranau, V., Hlushkou, D., Höltzel, A. & Tallarek, U. Topological analysis of non-granular, disordered porous media: determination of pore connectivity, pore coordination, and geometric tortuosity in physically reconstructed silica monoliths. *New Journal of Chemistry* **40**, 4187-4199 (2016).

141 Hua, M. *et al*. Tough-Hydrogel Reinforced Low-Tortuosity Conductive Networks for Stretchable and High-Performance Supercapacitors. *Advanced Materials*, 2100983 (2021).

142 O'Connell, B. M., McGloughlin, T. M. & Walsh, M. T. Factors that affect mass transport from drug eluting stents into the artery wall. *Biomedical engineering online* **9**, 1-16 (2010).

143 Guy, Y., Faraji, A. H., Gavigan, C. A., Strein, T. G. & Weber, S. G. Iontophoresis From a Micropipet into a Porous Medium Depends on the ζ-Potential of the Medium. *Analytical chemistry* **84**, 2179-2187 (2012).

144 Demidova-Rice, T. N., Hamblin, M. R. & Herman, I. M. Acute and impaired wound healing: pathophysiology and current methods for drug delivery, part 1: normal and chronic wounds: biology, causes, and approaches to care. *Adv Skin Wound Care* **25**, 304-314 (2012). https://doi.org:10.1097/01.ASW.0000416006.55218.d0

145 Wang, C. *et al*. Flexible patch with printable and antibacterial conductive hydrogel electrodes for accelerated wound healing. *Biomaterials* **285**, 121479 (2022). https://doi.org:https://doi.org/10.1016/j.biomaterials.2022.121479

146 Selberg, J., Gomez, M. & Rolandi, M. The Potential for Convergence between Synthetic Biology and Bioelectronics. *Cell Systems* **7**, 231-244 (2018). https://doi.org:https://doi.org/10.1016/j.cels.2018.08.007

147 Shaner, S. *et al*. Bioelectronic microfluidic wound healing: a platform for investigating direct current stimulation of injured cell collectives. *Lab on a Chip* **23**, 1531-1546 (2023). https://doi.org:10.1039/D2LC01045C

148 Yu, R., Zhang, H. & Guo, B. Conductive Biomaterials as Bioactive Wound Dressing for Wound Healing and Skin Tissue Engineering. *Nano-Micro Letters* **14**, 1 (2021). https://doi.org:10.1007/s40820-021-00751-y

149 Mahanta, A. K. *et al*. Nanoparticle-Induced Controlled Drug Delivery Using Chitosan-Based Hydrogel and Scaffold: Application to Bone Regeneration. *Molecular Pharmaceutics* **16**, 327-338 (2019). https://doi.org:10.1021/acs.molpharmaceut.8b00995

150 Obara, K. *et al*. Photocrosslinkable chitosan hydrogel containing fibroblast growth factor-2 stimulates wound healing in healing-impaired db/db mice. *Biomaterials* **24**, 3437-3444 (2003). https://doi.org:https://doi.org/10.1016/S0142-9612(03)00220-5

151 Panwar, V. *et al*. Tunable, conductive, self-healing, adhesive and injectable hydrogels for bioelectronics and tissue regeneration applications. *Journal of Materials Chemistry B* **9**, 6260-6270 (2021). https://doi.org:10.1039/D1TB01075A

152 Dargaville, T. R. *et al*. Sensors and imaging for wound healing: A review. *Biosensors and Bioelectronics* **41**, 30-42 (2013). https://doi.org:https://doi.org/10.1016/j.bios.2012.09.029

153 Dechiraju, H. *et al*. On-chip on-demand delivery of K+ for in vitro bioelectronics. *AIP Advances* **12** (2022). https://doi.org:10.1063/5.0129134

154 Isaksson, J. *et al*. Electronic control of Ca2+ signalling in neuronal cells using an organic electronic ion pump. *Nat Mater* **6**, 673-679 (2007). https://doi.org:10.1038/nmat1963

155 CHESLER, M. Regulation and Modulation of pH in the Brain. *Physiological Reviews* **83**, 1183-1221 (2003). https://doi.org:10.1152/physrev.00010.2003

156 Tybrandt, K. *et al*. Translating Electronic Currents to Precise Acetylcholine–Induced Neuronal Signaling Using an Organic Electrophoretic Delivery Device. *Advanced Materials* **21**, 4442-4446 (2009). https://doi.org:https://doi.org/10.1002/adma.200900187

157 Williamson, A. *et al*. Controlling Epileptiform Activity with Organic Electronic Ion Pumps. *Advanced Materials* **27**, 3138-3144 (2015). https://doi.org:https://doi.org/10.1002/adma.201500482

158 Simon, D. T. *et al*. Organic electronics for precise delivery of neurotransmitters to modulate mammalian sensory function. *Nature Materials* **8**, 742-746 (2009). https://doi.org:10.1038/nmat2494

159 Jia, M. *et al*. A multi-ion electrophoretic pump for simultaneous on-chip delivery of H+, Na+, and Cl–. *APL Materials* **10** (2022). https://doi.org:10.1063/5.0084570

160 Hoffmann, O. *et al*. Triptans Reduce the Inflammatory Response in Bacterial Meningitis. *Journal of Cerebral Blood Flow & Metabolism* **22**, 988-996 (2002). https://doi.org:10.1097/00004647-200208000-00010

161 Döring, K., Best, C., Birklein, F. & Krämer, H. H. Zolmitriptan inhibits neurogenic inflammation and pain during electrical stimulation in human skin. *European Journal of Pain* **19**, 966-972 (2015). https://doi.org:https://doi.org/10.1002/ejp.622

162 Sadiq, A. *et al*. The Role of Serotonin during Skin Healing in Post-Thermal Injury. *International Journal of Molecular Sciences* **19**, 1034 (2018).

163 Fregoso, D. R. *et al*. Skin-brain axis signaling mediates behavioral changes after skin wounding. *Brain, Behavior, & Immunity - Health* **15**, 100279 (2021). https://doi.org:https://doi.org/10.1016/j.bbih.2021.100279

164 Guo, R. & Liu, J. Implantable liquid metal-based flexible neural microelectrode array and its application in recovering animal locomotion functions. *Journal of Micromechanics and Microengineering* **27**, 104002 (2017). https://doi.org:10.1088/1361-6439/aa891c

165 Miranda, I. *et al*. Properties and Applications of PDMS for Biomedical Engineering: A Review. *J Funct Biomater* **13** (2021). https://doi.org:10.3390/jfb13010002

166 Jia, M., Luo, L. & Rolandi, M. Correlating Ionic Conductivity and Microstructure in Polyelectrolyte Hydrogels for Bioelectronic Devices.

Macromolecular Rapid Communications **43**, 2100687 (2022). https://doi.org:https://doi.org/10.1002/marc.202100687

167 Vasile, E. *et al*. Making precious metals cheap: A sonoelectrochemical - Hydrodynamic cavitation method to recycle platinum group metals from spent automotive catalysts. *Ultrason Sonochem* **72**, 105404 (2021). https://doi.org:10.1016/j.ultsonch.2020.105404

168 Nguyen, T., Asefifeyzabadi, N., Li, H., Luo, L. & Rolandi, M. The Importance of Electrode Material in Bioelectronic Electrophoretic Ion Pumps. *Advanced Materials Technologies* **n/a**, 2201996 https://doi.org:https://doi.org/10.1002/admt.202201996

169 Allen J. Bard, R. P., Joseph Jordan. Standard Potentials in Aqueous Solution. (1985). https://doi.org:https://doi.org/10.1201/9780203738764

170 Yoon, D. J. *et al*. Topical Fluoxetine as a Potential Nonantibiotic Adjunctive Therapy for Infected Wounds. *Journal of Investigative Dermatology* **141**, 1608-1612.e1603 (2021). https://doi.org:https://doi.org/10.1016/j.jid.2020.11.016

171 Schoenen, J. & Sawyer, J. Zolmitriptan (Zomig™, 311C90), a novel dual central and peripheral 5HT1B/1D agonist: An overview of efficacy. *Cephalalgia* **17**, 28-40 (1997). https://doi.org:10.1177/0333102497017s1805

172 Bennison, L. *et al*. The pH of wounds during healing and infection: A descriptive literature review. *Wound Practice & Research: Journal of the Australian Wound Management Association* **25**, 63 (2017).

173 Percival, S. L., McCarty, S., Hunt, J. A. & Woods, E. J. The effects of pH on wound healing, biofilms, and antimicrobial efficacy. *Wound Repair and Regeneration* **22**, 174-186 (2014). https://doi.org:https://doi.org/10.1111/wrr.12125

174 Liu, Y., Kalén, A., Risto, O. & Wahlström, O. Fibroblast proliferation due to exposure to a platelet concentrate in vitro is pH dependent. *Wound Repair Regen* **10**, 336-340 (2002). https://doi.org:10.1046/j.1524-475x.2002.10510.x

175 Lucas, T. *et al*. Differential roles of macrophages in diverse phases of skin repair. *J Immunol* **184**, 3964-3977 (2010). https://doi.org:10.4049/jimmunol.0903356

176 Zhao, M. *et al*. Electrical signals control wound healing through phosphatidylinositol-3-OH kinase-gamma and PTEN. *Nature* **442**, 457-460 (2006).

177 Alberts B, J. A., Lewis J, et al. *Principles of Membrane Transport*. (Garland Science, 2002).

178 Szaciłowski, K. Digital Information Processing in Molecular Systems. *Chemical Reviews* **108**, 3481-3548 (2008). https://doi.org:10.1021/cr068403q

179 Waser, R. *Nanoelectronics and information technology: advanced electronic materials and novel devices*. (John Wiley & Sons, 2012).

180 Noy, A. Bionanoelectronics. *Advanced Materials* **23**, 807-820 (2011). https://doi.org:https://doi.org/10.1002/adma.201003751

181 Roseman, J. M., Lin, J., Ramakrishnan, S., Rosenstein, J. K. & Shepard, K. L. Hybrid integrated biological–solid-state system powered with adenosine triphosphate. *Nature Communications* **6**, 10070 (2015). https://doi.org:10.1038/ncomms10070

182 Kawan, M. *et al*. Monitoring supported lipid bilayers with n-type organic electrochemical transistors. *Materials Horizons* **7**, 2348-2358 (2020). https://doi.org:10.1039/d0mh00548g

183 Lu, Z. *et al*. Understanding electrochemical properties of supported lipid bilayers interfaced with organic electronic devices. *Journal of Materials Chemistry C* **10**, 8050-8060 (2022). https://doi.org:10.1039/D2TC00826B

184 Soto-Rodríguez, J., Hemmatian, Z., Black, J., Rolandi, M. & Baneyx, F. Two-Channel Bioprotonic Photodetector. *ACS Applied Bio Materials* **2**, 930-935 (2019). https://doi.org:10.1021/acsabm.8b00789

185 Tunuguntla, R. H. *et al*. Enhanced water permeability and tunable ion selectivity in subnanometer carbon nanotube porins. *Science* **357**, 792-796 (2017). https://doi.org:doi:10.1126/science.aan2438

186 Rothemund, P. W. K. Folding DNA to create nanoscale shapes and patterns. *Nature* **440**, 297-302 (2006). https://doi.org:10.1038/nature04586

187 Fu, D. & Reif, J. 3D DNA Nanostructures: The Nanoscale Architect. *Applied Sciences* **11**, 2624 (2021).

188 Langecker, M., Arnaut, V., List, J. & Simmel, F. C. DNA Nanostructures Interacting with Lipid Bilayer Membranes. *Accounts of Chemical Research* **47**, 1807-1815 (2014). https://doi.org:10.1021/ar500051r

189 List, J., Weber, M. & Simmel, F. C. Hydrophobic Actuation of a DNA Origami Bilayer Structure. *Angewandte Chemie International Edition* **53**, 4236-4239 (2014). https://doi.org:https://doi.org/10.1002/anie.201310259

190 Shetty, R. M., Brady, S. R., Rothemund, P. W. K., Hariadi, R. F. & Gopinath, A. Bench-Top Fabrication of Single-Molecule Nanoarrays by DNA Origami Placement. *ACS Nano* **15**, 11441-11450 (2021). https://doi.org:10.1021/acsnano.1c01150

191 Frtús, A. *et al*. The interactions between DNA nanostructures and cells: A critical overview from a cell biology perspective. *Acta Biomaterialia* **146**, 10-22 (2022). https://doi.org:https://doi.org/10.1016/j.actbio.2022.04.046

192 Lacroix, A. & Sleiman, H. F. DNA Nanostructures: Current Challenges and Opportunities for Cellular Delivery. *ACS Nano* **15**, 3631-3645 (2021). https://doi.org:10.1021/acsnano.0c06136

193 Douglas, S. M. *et al*. Self-assembly of DNA into nanoscale three-dimensional shapes. *Nature* **459**, 414-418 (2009). https://doi.org:10.1038/nature08016

194 Göpfrich, K. *et al*. DNA-Tile Structures Induce Ionic Currents through Lipid Membranes. *Nano Letters* **15**, 3134-3138 (2015). https://doi.org:10.1021/acs.nanolett.5b00189

195 Diederichs, T. *et al*. Synthetic protein-conductive membrane nanopores built with DNA. *Nature Communications* **10**, 5018 (2019). https://doi.org:10.1038/s41467-019-12639-y

196 Hemmatian, Z. *et al*. Taking electrons out of bioelectronics: bioprotonic memories, transistors, and enzyme logic. *Journal of Materials Chemistry C* **3**, 6407-6412 (2015). https://doi.org:10.1039/c5tc00502g

197 Hemmatian, Z. *et al*. Electronic control of H(+) current in a bioprotonic device with Gramicidin A and Alamethicin. *Nat Commun* **7**, 12981 (2016). https://doi.org:10.1038/ncomms12981

198 Göpfrich, K. *et al*. Ion Channels Made from a Single Membrane-Spanning DNA Duplex. *Nano Letters* **16**, 4665-4669 (2016). https://doi.org:10.1021/acs.nanolett.6b02039

199 Jap, B. K. & Walian, P. J. Structure and functional mechanism of porins. *Physiological Reviews* **76**, 1073-1088 (1996). https://doi.org:10.1152/physrev.1996.76.4.1073

200 Bayley, H., Braha, O. & Gu, L.-Q. Stochastic Sensing with Protein Pores. *Advanced Materials* **12**, 139-142 (2000). https://doi.org:https://doi.org/10.1002/(SICI)1521-4095(200001)12:2<139::AID-ADMA139>3.0.CO;2-Q

201 Maingi, V. *et al*. Stability and dynamics of membrane-spanning DNA nanopores. *Nature Communications* **8**, 14784 (2017). https://doi.org:10.1038/ncomms14784

202 Seeman, N. C. & Sleiman, H. F. DNA nanotechnology. *Nature Reviews Materials* **3**, 17068 (2017). https://doi.org:10.1038/natrevmats.2017.68

203 Douglas, S. M. *et al*. Rapid prototyping of 3D DNA-origami shapes with caDNAno. *Nucleic Acids Research* **37**, 5001-5006 (2009). https://doi.org:10.1093/nar/gkp436

204 Deng, Y. *et al*. H+-type and OH- -type biological protonic semiconductors and complementary devices. *Sci Rep* **3**, 2481 (2013). https://doi.org:10.1038/srep02481

205 Ohmann, A. *et al*. Controlling aggregation of cholesterol-modified DNA nanostructures. *Nucleic Acids Research* **47**, 11441-11451 (2019). https://doi.org:10.1093/nar/gkz914

206 Dundas, C. M., Demonte, D. & Park, S. Streptavidin–biotin technology: improvements and innovations in chemical and biological applications. *Applied Microbiology and Biotechnology* **97**, 9343-9353 (2013). https://doi.org:10.1007/s00253-013-5232-z

207 Kuzuya, A., Numajiri, K., Kimura, M. & Komiyama, M. Single-Molecule Accommodation of Streptavidin in Nanometer-Scale Wells Formed in DNA Nanostructures. *Nucleic Acids Symposium Series* **52**, 681-682 (2008). https://doi.org:10.1093/nass/nrn344

208 Wang, Y. *et al*. Magnetic microparticle-based SELEX process for the identification of highly specific aptamers of heart marker--brain natriuretic

peptide. *Microchimica Acta* **182**, 331-339 (2015). https://doi.org:10.1007/s00604-014-1338-y

209 Holmberg, A. *et al*. The biotin-streptavidin interaction can be reversibly broken using water at elevated temperatures. *Electrophoresis* **26**, 501-510 (2005). https://doi.org:10.1002/elps.200410070

210 Jönsson, U. *et al*. Real-time biospecific interaction analysis using surface plasmon resonance and a sensor chip technology. *Biotechniques* **11**, 620-627 (1991).

211 Islam, M. A., Chowdhury, M. A., Mozumder, M. S. I. & Uddin, M. T. Langmuir Adsorption Kinetics in Liquid Media: Interface Reaction Model. *ACS Omega* **6**, 14481-14492 (2021). https://doi.org:10.1021/acsomega.1c01449

212 Khan, A. *et al*. Development and application of ligand-based NMR screening assays for γ-butyrobetaine hydroxylase. *MedChemComm* **7**, 873-880 (2016). https://doi.org:10.1039/C6MD00004E

213 Zhang, B. *et al*. Role of contacts in long-range protein conductance. *Proceedings of the National Academy of Sciences* **116**, 5886-5891 (2019). https://doi.org:doi:10.1073/pnas.1819674116

214 Braner, M., Kollmannsperger, A., Wieneke, R. & Tampé, R. 'Traceless' tracing of proteins – high-affinity trans-splicing directed by a minimal interaction pair. *Chemical Science* **7**, 2646-2652 (2016). https://doi.org:10.1039/C5SC02936H

215 Huang, R., Bonnichon, A., Claridge, T. D. W. & Leung, I. K. H. Protein-ligand binding affinity determination by the waterLOGSY method: An optimised

approach considering ligand rebinding. *Scientific Reports* **7**, 43727 (2017). https://doi.org:10.1038/srep43727

216 Weber, M. J. *et al*. Atomic Layer Deposition of High-Purity Palladium Films from Pd(hfac)2 and H2 and O2 Plasmas. *The Journal of Physical Chemistry C* **118**, 8702-8711 (2014). https://doi.org:10.1021/jp5009412

217 Shim, J. S., Geng, J., Ahn, C. H. & Guo, P. Formation of lipid bilayers inside microfluidic channel array for monitoring membrane-embedded nanopores of phi29 DNA packaging nanomotor. *Biomed Microdevices* **14**, 921-928 (2012). https://doi.org:10.1007/s10544-012-9671-6

218 Lind, T. K. & Cárdenas, M. Understanding the formation of supported lipid bilayers via vesicle fusion-A case that exemplifies the need for the complementary method approach (Review). *Biointerphases* **11**, 020801 (2016). https://doi.org:10.1116/1.4944830

219 Nickel, B. Nanostructure of supported lipid bilayers in water. *Biointerphases* **3**, Fc40-46 (2008). https://doi.org:10.1116/1.3007998

220 Richter, R. P. & Brisson, A. R. Following the formation of supported lipid bilayers on mica: a study combining AFM, QCM-D, and ellipsometry. *Biophys J* **88**, 3422-3433 (2005). https://doi.org:10.1529/biophysj.104.053728

221 Kang, M., Day, C. A., Kenworthy, A. K. & DiBenedetto, E. Simplified Equation to Extract Diffusion Coefficients from Confocal FRAP Data. *Traffic* **13**, 1589-1600 (2012). https://doi.org:10.1111/tra.12008